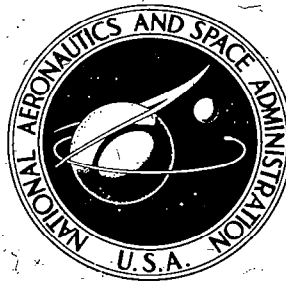


NASA TECHNICAL
REPORT



NASA TR R-330

NASA TR R-330

LOAN COPY: RETURN TO
AFWL (WL0L)
KIRTLAND AFB, N MEX

EXPERIMENTAL AND ANALYTICAL
INVESTIGATION OF THE FLUTTER
OF FLAT BUILT-UP PANELS
UNDER STREAMWISE INPLANE LOAD

by Robert W. Hess
Langley Research Center
Langley Station, Hampton, Va.



1. Report No. NASA TR R-330	2. Government Accession No.	3. Recipient's Catalog No.	
4. Title and Subtitle EXPERIMENTAL AND ANALYTICAL INVESTIGATION OF THE FLUTTER OF FLAT BUILT-UP PANELS UNDER STREAMWISE INPLANE LOAD		5. Report Date February 1970	
		6. Performing Organization Code	
7. Author(s) Robert W. Hess		8. Performing Organization Report No. L-6640	
		10. Work Unit No. 126-14-14-03-23	
9. Performing Organization Name and Address NASA Langley Research Center Hampton, Va. 23365		11. Contract or Grant No.	
		13. Type of Report and Period Covered Technical Report	
12. Sponsoring Agency Name and Address National Aeronautics and Space Administration Washington, D.C. 20546		14. Sponsoring Agency Code	
		15. Supplementary Notes	
16. Abstract The flutter of 13 panels subject to streamwise inplane load at Mach numbers of 1.57 and 1.96 has been investigated. Panel length-width ratios ranged from 1 to 4.2. The experimental flutter boundary was compared with an analytical flutter boundary for six of the panels. Damping, both aerodynamic and structural, was found to have a pronounced effect on the analytical flutter boundary. The agreement between analysis and experiment was dependent upon how structural damping was introduced in the formulation of the problem.			
17. Key Words Suggested by Author(s) Panel flutter Inplane load Damping		18. Distribution Statement Unclassified - Unlimited	
19. Security Classif. (of this report) Unclassified	20. Security Classif. (of this page) Unclassified	21. No. of Pages 87	22. Price* \$3.00

*For sale by the Clearinghouse for Federal Scientific and Technical Information
Springfield, Virginia 22151



CONTENTS

	Page
SUMMARY	1
INTRODUCTION	1
SYMBOLS	2
APPARATUS	5
Wind Tunnel	5
Vacuum Chamber	5
Splitter Plate and Loading Mechanism	6
INSTRUMENTATION	6
PANELS	7
Configuration	7
Buckling Stress	7
Frequencies	8
Damping	10
FLUTTER TESTS	11
Procedure	11
Experimental Results	12
ANALYSIS	13
Flutter Solution With Zero-Stress Modes	14
Flutter Solution With Stressed Modes	16
DISCUSSION OF ANALYTICAL FLUTTER RESULTS AND COMPARISON WITH EXPERIMENT	17
CONCLUSIONS	20
APPENDIX A – LOCAL FLOW CONDITIONS	22
APPENDIX B – MODE-SHAPE MEASURING APPARATUS AND PROCEDURES	23
Apparatus	23
Procedure	23
APPENDIX C – DETAILS OF FLUTTER SOLUTION	25
Zero-Stress-Mode Solution	25
Stressed-Mode Solution	32

	Page
REFERENCES	38
TABLES	40
FIGURES	45

**EXPERIMENTAL AND ANALYTICAL INVESTIGATION OF
THE FLUTTER OF FLAT BUILT-UP PANELS
UNDER STREAMWISE INPLANE LOAD**

By Robert W. Hess
Langley Research Center

SUMMARY

This paper presents both experimental and analytical flutter results of an investigation of the effects of streamwise inplane load on 13 panels at Mach numbers of 1.57 and 1.96. The panels were supported by longitudinal stiffeners and transverse frames, the spacing of these members allowing a variation in the length-width ratio from 1.0 to 4.2. The experimental results are compared with calculated results for six of the panels. Two sets of calculations were made by using linearized quasi-steady aerodynamic theory in conjunction with a Galerkin procedure. The calculations differed in the treatment of structural damping. One set of calculations employed calculated vibration mode shapes for an unstressed panel and the structural damping was applied to panel bending only. The second calculation employed calculated vibration mode shapes for the panel in a stressed condition, and structural damping was applied to both panel bending and compression.

INTRODUCTION

There are many variables that affect panel flutter and a major problem involved in the study of panel flutter is the isolation and determination of the significance of these variables. The flutter boundary for a particular panel is a complex function of such variables as panel configuration; midplane stress; edge restraint; flow angularity; dynamic pressure; Mach number; pressure differential and gradient; structural, aerodynamic, and acoustic damping; and boundary-layer thickness. The destabilizing effect of midplane stress has been the subject of many experimental and analytical investigations since the work of Sylvester and Baker (ref. 1). Reviews that contain some results of these efforts may be found in references 2 to 5. The agreement between experiment and theory has often been poor because of the inability to define or control adequately the variables affecting the onset of flutter. In addition, as pointed out in reference 6, the misapplication of damping in analytical solutions appears to have been the cause of much of the lack of agreement for stressed panels.

The purpose of the investigation reported in the present paper was to examine the flutter of flat isotropic panels subject to inplane compressive loads in the streamwise direction only and constructed to simulate practical edge conditions. A series of 13 multibay panels was constructed so that for each, the test panel was the center bay of a built-up structure. The center bay was supported by longitudinal stiffeners and transverse frames whose spacing defined test-panel length-width ratios ranging from 1.0 to 4.2. The dynamic pressure and frequencies at flutter were calculated by two methods for six of the panels, and these analytical values were compared with the experimental results. Linearized aerodynamic theory for two-dimensional flow in which the aerodynamic damping term was retained (also known as "modified piston theory") was used in both methods in conjunction with a Galerkin (modal) procedure. Mode shapes calculated with zero inplane stress were used in the first method in which the structural damping appeared only with the bending terms. Mode shapes calculated with inplane stress were used in the second method in which the structural damping was applied to both the bending and the inplane load terms.

Appendix A presents the measured flow conditions over the panel. Appendix B discusses the techniques and apparatus used in measuring panel mode shapes, frequencies, and damping. Appendix C gives the details of the two analyses used in the present paper.

SYMBOLS

This list contains only those symbols that are significant to the entire paper. Symbols are defined in appendix C that are restricted in meaning to that section of the paper.

A_m, A_n	complex modal amplitude coefficients
a_1	speed of sound over panel
\bar{B}	parameter defined by equation (C11)
C_0, C_1, C_2	modal integrals defined by equations (4)
$C_{mn}^{(3)}, C_{mn}^{(4)}, C_{mn}^{(5)}$	modal integrals defined by equations (8)
D	panel flexural rigidity, $\frac{Eh_p^3}{12(1 - \nu^2)}$

E	Young's modulus
f	panel frequency
g	structural damping coefficient
g _a	aerodynamic damping coefficient, equations (13)
h	thickness
$i = \sqrt{-1}$	
k	reduced frequency, $l\omega/V_1$
l	length of test panel
M ₁	local Mach number
M _{t,θ}	torsional stiffness of stiffeners
N _x	inplane loading in stream direction, positive in compression
$\bar{N}_x = \frac{N_x}{\gamma l^2}$	
N _y	inplane loading in cross-stream direction, positive in compression
$\bar{N}_y = \frac{N_y}{\gamma w^2} \frac{C_1}{C_0}$	
Δp	static pressure differential
q	dynamic pressure
R	radius
t	time
V ₁	velocity of airstream over panel

w	width of test panel
x,y,z	orthogonal coordinates (see fig. 11)
X _A	streamwise asymmetric deflection function
X _S	streamwise symmetric deflection function
Y ₁	spanwise deflection function
Z	panel deflection
$\alpha, \beta, \bar{\beta}$	eigenfunction in arguments X _A , X _S
$\beta_M = \sqrt{M_1^2 - 1}$	
γ	mass per unit area
η	nondimensional coordinate in y-direction, $\frac{y}{w}$
λ	dynamic-pressure parameter, $\frac{2ql^3}{\beta_M D}$
μ_1	density ratio, $\frac{\gamma}{\rho_1 l}$
ν	Poisson's ratio for isotropic plate
ξ	nondimensional coordinate in x-direction, $\frac{x}{l}$
ρ_1	air density over panel
σ	inplane stress in stream direction, positive for compression
σ_{cr}	static buckling stress with no airflow
Ω	flutter eigenvalue parameter, $(\omega_r/\omega)^2(1 + ig)$
ω	circular flutter frequency

ω_r circular reference frequency, $\sqrt{\frac{\pi^4 D}{l^4 \gamma}}$

ω_m circular natural frequency mode m

Subscripts:

m,n mode numbers

p panel

ad aerodynamic damping

r reference

s stiffener

APPARATUS

Wind Tunnel

The flutter tests were conducted in the Langley Unitary Plan wind tunnel at free-stream Mach numbers of 2 and 1.6. The dynamic pressure in that tunnel is continuously variable with maximum levels of 2550 psf (122 kN/m²) and 2400 psf (114.9 kN/m²) at free-stream Mach numbers of 2 and 1.6, respectively.

The splitter plate on which the panels were mounted (fig. 1) projected into the air-stream 15 inches (38 cm) from the tunnel sidewall so that the flutter tests could be conducted free of the tunnel boundary layer. To maintain the smallest possible pressure gradient on the surface of the panel, the splitter plate had a negative angle of attack of 1.05° with respect to the free stream. The resulting local Mach numbers over the panel were 1.96 and 1.57 for the respective free-stream Mach numbers of 2.0 and 1.6. The local static and dynamic flow conditions over the panel are given in appendix A.

Vacuum Chamber

The panel vibration characteristics were determined in the 55-foot-diameter (16.764 m) vacuum chamber of the Langley dynamics research laboratory. The vacuum system is capable of evacuating the chamber from atmospheric pressure to 0.2 mm mercury absolute.

Splitter Plate and Loading Mechanism

The splitter plate (fig. 2), which had a cavity 1.8 inches (4.572 cm) deep, 38.42 inches (97.587 cm) long, and 24.38 inches (61.925 cm) wide, contained the hydraulic mechanism for applying inplane loads to the panel. The leading edge of the panel was bolted to the splitter plate and the trailing edge was fastened to a movable mounting plate. A guide plate was supported from the back of the splitter plate cavity by three low-friction guides. The guide plate constrained the mounting plate to rectilinear movement only. Inplane compression loads (8000 lb (35 586 N) maximum) were applied at the trailing edge by means of hydraulic pressure acting on eight pistons which, in turn, loaded the movable mounting plate at the trailing edge. A single piston was used to return the system and to apply tension to the panel.

The streamwise edges of the built-up panel could be clamped to the splitter plate (fig. 1) by clamps which, upon being released, relieved accumulated shear stress due to inplane loading. Each clamp was pulled down by the vertical movement of five recessed bolts. The movement of these bolts (clamped or released) was actuated by remotely controlled pneumatic jacks. The leading edge of the clamp was bolted to the splitter plate and a flex hinge, which had been milled into the clamp ahead of the panel leading edge, allowed translation and rotation of the remaining portion of the clamp.

All openings to the splitter plate were sealed with appropriate O-rings, gaskets, or sheet rubber. Pressure in the cavity was controlled by bleeding in or evacuating air through a 1-inch (2.54-cm) tube.

INSTRUMENTATION

The basic instrumentation consisted of four four-arm strain-gage bridges mounted on the test panel. Three of these measured compression; one at the leading edge, one at the trailing edge, and one next to the middle of a longitudinal stiffener at one side of the test panel. The fourth strain-gage bridge measured bending at the trailing edge of the panel. Its dc output was monitored on a digital voltmeter, and its ac output was monitored on an oscilloscope. Two pressure cells (5 psi (34.475 kN/m²)), which measured the pressure differential between the cavity behind the panel and the surface of the panel, were used to establish a minimum pressure differential.

The output of the compression gages, panel pressure cells, and the pressure cells used for measuring the hydraulic pressure of the loading apparatus was monitored on self-balancing potentiometers. These outputs and that of the bending gage were also recorded by a recording oscillograph and a frequency-modulated tape recorder.

Thermocouples were mounted at the center of the panel and at the leading edge adjacent to the transverse frame. The temperatures at these two locations were read on recording potentiometers.

PANELS

Configuration

The panels were built-up structures, as shown in figures 3 and 4, in which only the center bay constituted the test panel. The method of construction was chosen to provide a realistic edge restraint for the panels. The length and width of the center bay (measured from rivet line to rivet line) was varied by using different spacing of the transverse frames and of the principal longitudinal stiffeners (those adjacent to the center bay). The principal longitudinal stiffeners were continuous and welded to the doublers at the leading and trailing edge of the structure whereas the auxiliary stiffeners were interrupted by the transverse frame. The auxiliary stiffeners were incorporated to raise the buckling loads and the flutter dynamic pressure of the adjacent panels to levels higher than that of the test panel. In addition, some bays adjacent to the test panel were stiffer since they were constructed with a thicker skin which overlapped the test panel at the stiffener. This construction was used only for high length-width ratio panels. A summary of the panel configurations is given in figure 5, and a table of the physical properties is given in table I. Two orifices were located in the skin of the built-up panel, one ahead of the forward transverse frame, the second just back of the aft transverse frame, to provide a means to measure the pressure differential between the cavity and the surface of the panel.

Buckling Stress

The ratio of inplane stress to static buckling stress σ/σ_{CR} is a primary variable in this investigation. The buckling stress was calculated and determined experimentally for each panel. The calculated values were determined from the equations of reference 7. The torsional stiffness $M_{t,\theta}$ of the edge supports was calculated by using shear flow analysis. (See ref. 8, for example.) In order to verify the accuracy of the calculated values of $M_{t,\theta}$, seven test specimens such as shown in figure 6 were constructed and tested, and the important dimensions are given in table II. Experimental values of $M_{t,\theta}$ were between 20 and 27.7 percent lower than the calculated values. On five of the specimens, the rivet spacing was reduced by a factor of two and, as a result, the difference between calculation and experiment was reduced to between 2.7 and 15 percent. The design rivet spacing was not changed on the test panels, but the calculated values for the torsional stiffness were consequently reduced by 24 percent as given in table I under "Adjusted torsional stiffness."

Experimental values of buckling stress are, in general, dependent on the means of loading (by displacement or by force), panel support, and initial deformation. The necessity of using pneumatic clamps to secure the side edges of the built-up panel to the splitter plate imposed an additional restraint and all buckling measurements were made with the clamps in the clamped condition. The load was applied in increments and the clamps were cycled (released and clamped) at each increment. In all cases the actuation of the clamps increased the inplane stress somewhat. This condition was undoubtedly due to the fact that the edges of the panel did not precisely conform to the splitter plate along the length of the panel edge and the final increment of stress was actually applied by the side clamps.

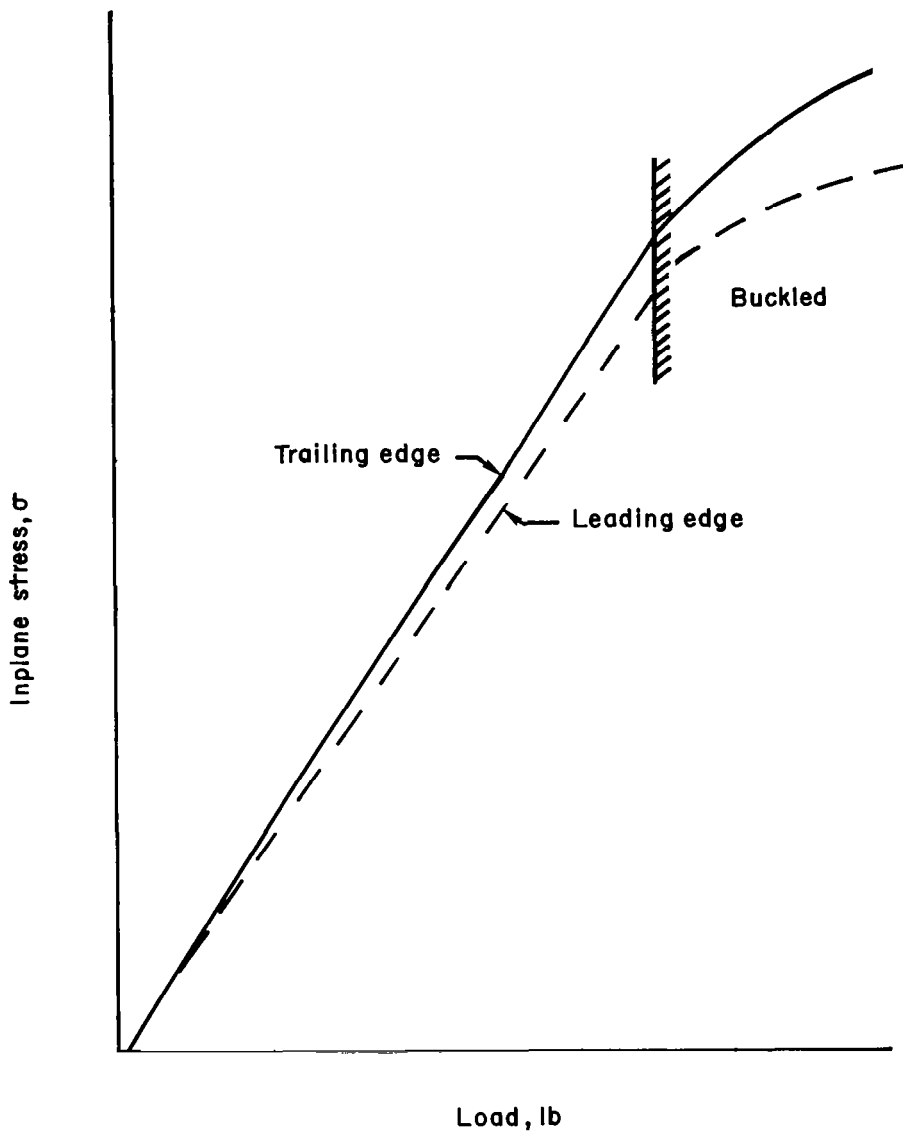
Zero stress was consistently obtained by initially putting the panel in tension, releasing the hydraulic pressure, and then repeatedly cycling the clamps until no change in strain was measured in the clamped condition. This procedure gave repeatable values of buckling stress and repeatable values of zero strain after compression loading. Table I lists two values of experimental buckling stress because in most cases, the measured stress at buckling differed between the leading-edge (L.E.) and the trailing-edge (T.E.) strain-gage locations. In most cases, the location with the highest stress level had a higher stress-loading slope from no load to buckling as is shown in sketch (a).

The thickness of critical members – skin, stiffener, and frames – differed on panels 7 to 13. The requirement that the stiffeners be stable beyond the critical buckling stress of the test panel resulted in large values of stiffness ratio $M_{t, \theta}/D$ and essentially clamped-edge conditions.

Frequencies

Panel frequencies were measured at atmospheric pressure before and after the flutter tests. The small cavity depth of 1.8 inches (4.57 cm) in the splitter plate precluded meaningful comparison with calculated frequencies because of the stiffening and damping effects of the air in a shallow cavity. These effects were explored experimentally and analytically in references 9 and 10, respectively. At the completion of the flutter tests, the splitter plate was installed in the vacuum chamber and the natural frequencies, mode shapes, and structural damping were measured for panels 1 to 5 at levels of inplane load and ambient pressure that corresponded to those of the experimental flutter boundary. The details of the apparatus and procedure are described in appendix B.

For comparison with experiment and for use in the flutter analysis, the natural frequencies and mode shapes were calculated for panels 1 to 6 by using the equations of reference 7. Figure 7 gives the calculated natural frequencies as a function of inplane stress. Figure 7 also contains the corresponding measured frequencies for panels 1 to 5. For comparison purposes, the experimental values at zero stress are given at the



Sketch (a).

lowest density for which they were obtained. A comparison of measured and calculated mode shapes is shown in figure 8 for the first and third modes of panel 3 at stress ratios σ/σ_{CR} of 0, 0.20, and 0.45. These mode shapes were measured after flutter testing and are considered to be typical. The greatest difference between calculated and measured mode shapes was in the lower modes, and this difference was amplified by increased inplane load. It should be noted that all symmetric modes were excited by a shaker at the center of the panel.

The solution of the equations of reference 7 for the panel frequencies and mode shapes as a function of inplane stress was programed by using Newton iteration procedures. Equations (16) to (19) of reference 7 are of two types depending on panel geometry and inplane load. For zero inplane stress, the eigenfunction is composed of trigonometric and hyperbolic functions. As the compression load is increased, the solution enters a region (shown as dashed lines in fig. 7) in which the lower eigenfunctions are composed only of trigonometric functions. As is found in reference 7, there are levels of stress in this region where with changing stress, panel modes evolve so that inflection points and internal node lines appear and disappear. During a preliminary test of the mode-shape surveying apparatus in the vacuum chamber, before the flutter tests, modes such as shown in figure 5 of reference 7 were encountered. However, because of the difficulty in mapping the mode shapes of a damped system at high stress levels, it was decided to restrict measurements to conditions of inplane loading below a stress-ratio σ/σ_{cr} of 0.55.

The frequencies measured at atmospheric pressure and with zero inplane load were lower after the flutter tests than they were before. With the exception of panel 3, the measured values of the panel frequency in a vacuum are significantly less (10 to 20 percent) than the calculated values. This result coupled with the fact that the measured buckling stress prior to flutter testing was close to the calculated value (except for panel 4) is a measure of the loss of stiffness caused by the flutter testing.

Damping

For no airflow, the damping of the panel vibration was affected by the interdependent variables of cavity size, ambient pressure, inplane stress, mode, frequency, amplitude, and energy dissipation at structural joints. The ambient pressure and stress ratio were varied during the damping measurements of the various modes. Because of the number of variables and their interdependence, a plot of damping as a function of frequency results in a wide scatter band and no general conclusions are justified. The test results are tabulated in table III and were obtained in the vacuum chamber for the lower modes of panels 1 to 5. The damping coefficient g was determined from measurements of the vibration decrement. Most of the data fall between values of g of 0.015 and 0.05 which is in the range cited in the published literature; that is, 0.01 for simple structures to 0.08 for complex, built-up structures. (See ref. 11.)

It was anticipated that panel 5 might have higher values of damping because of its construction; that is, the center bay had a lap joint with the thicker adjacent panels. As can be noted in table III, the level of damping does appear to be higher than that of panels 1 to 4. It was not anticipated that an application of an inplane load would result in a decrease in measured damping, but this decrease did occur for modes 3, 4, and 5

of panel 5. A close look at the damping of panels 1 to 4 indicates isolated examples of this behavior. A possible cause for this behavior, which was not explored, may be the coupling of modes between the test panel and the adjacent bays. As was discussed by Ungar and Scharton (ref. 12), indirect excitation of one panel or system by another causes an energy exchange and higher recorded values of damping. The degree of coupling between bays would be expected to vary with inplane stress since the rate of change of the natural frequencies with changing inplane load would not be the same for the center bay and the adjacent bays.

FLUTTER TESTS

Procedure

The general procedure was to set the tunnel flow to the desired dynamic pressure while maintaining the pressure in the cavity at a minimum difference from the pressure on the surface of the panel. The output of the two thermocouples was then monitored until both gave the same constant reading. The procedure for determining an effective zero-pressure differential was as follows: The inplane compressive load was incrementally increased until flutter was observed, at which time the differential pressure was slowly varied until maximum flutter amplitude was observed. The readings of differential pressure from the two transducers at maximum flutter amplitude were used as the new value of zero differential pressure.

After an effective zero differential pressure was established, the inplane load was released and the zero reference stress was recorded. Inplane load was then slowly increased incrementally. At each increment the clamps were cycled (released and clamped) to relieve any accumulated shear stress at the side edges. When the flutter boundary was approached in this manner, the first indication of flutter was the appearance of a small harmonic signal, superimposed on a response signal generated by aerodynamic noise, which usually increased slowly in amplitude with time. In some cases it was necessary to increase the inplane load beyond the initial point before the amplitude increased.

This procedure was not used for the case in which the minimum-dynamic-pressure flutter boundary was determined for a panel stiffened by the pressure differential. It was not prudent at the higher levels of dynamic pressure and differential pressure to release the clamps. To do so would result in the loss of stabilizing pressure differential and the possible loss of the strain gages or the panel because of violent flutter.

At low dynamic pressures, pressure differential and inplane load could be applied and the clamp cycled without risk to the panel. The dynamic pressure was then raised until flutter was observed. At this point both dynamic pressure and inplane load were

slowly varied until the minimum dynamic pressure at flutter was obtained. The dynamic pressure was then dropped and the procedure repeated at a higher pressure differential.

Experimental Results

The experimental results at Mach numbers of 1.96 and 1.57 are presented in figure 9 for flutter frequency and flutter dynamic pressure as a function of stress ratio. The stress ratio σ/σ_{cr} used in figure 9 is an average value. As was discussed in the section dealing with buckling stress, the buckling stress was not the same at each bridge location. At a given inplane load, the stress ratio was determined by using the buckling stress σ_{cr} for each panel compression bridge location and taking the average of the resulting ratios.

The data of figure 9 are characterized by a rapid decrease in the flutter dynamic pressure with increasing inplane stress. With the exception of two panels, the minimum dynamic pressure occurred at inplane stress ratios as low as 0.6. This result is in contrast to the flutter behavior of thermally stressed panels which have a nearly equal load in the streamwise and cross-stream direction. For this type of loading (ref. 6), the minimum flutter dynamic pressure is at the transition point (the intersection of the buckled and unbuckled panel boundary).

The flutter boundaries fell into two general categories at both Mach numbers: those which form a single smooth curve with increasing inplane stress, and those which exhibit abrupt changes. These changes are also accompanied by a jump in the panel flutter frequencies. An abrupt change in frequency can also be noted at or near zero stress for some panels whose boundaries fall in the first category. This flutter was at a frequency higher than that of most of the data, and the amplitude at a given stress ratio increased more slowly with time. Panel 12 (fig. 9(1)) is an example of the most extreme change in flutter boundary in that the high-frequency flutter was completely separate from the main body of the data and could be approached from a high and low level of stress ratio. The occurrence of high-frequency flutter in most cases prevented a good determination of the low-frequency flutter boundary near the zero stress level.

The $M_1 = 1.57$ data are at the same or higher dynamic pressure, at a given stress ratio, than the $M_1 = 1.96$ data. This result is contrary to the expected result that the flutter dynamic pressure decrease with decreasing Mach number. This result may be accounted for by considering the effects of local flow conditions at the two Mach numbers. The aerodynamic noise and the static-pressure variation along the center of the panel were both greater at $M_1 = 1.57$ than at $M_1 = 1.96$. The panel response to the aerodynamic noise had the effect that the onset of flutter was more difficult to detect at a Mach number of 1.57 and the greater static-pressure variation had a stiffening effect on the panel.

The stabilizing effects of maintaining a positive pressure differential (internal pressure greater than static external pressure) on an inplane-loaded panel were investigated with panel 11 at $M_1 = 1.96$. The results are given in figure 10 for flutter frequency and dynamic pressure as a function of static-pressure differential. Each point represents the minimum flutter dynamic pressure for the given differential pressure. Because of the stiffening effects of pressure differential, the inplane load at the minimum points increases with increasing Δp . The variation of the minimum dynamic pressure at flutter with pressure differential is relatively small near zero, but increased rapidly above a differential pressure of about 0.2 psi (1.379 kN/m²). At a Δp of 0.43 psi (2.96 kN/m²), the dynamic pressure at flutter is increased by a factor of eight; this increase is equivalent to a factor of two increase in panel thickness.

ANALYSIS

Based on the results of previous investigators, it is evident that structural and aerodynamic damping should be included in an analytical panel flutter model. Neglecting damping completely, as shown in reference 13, results in a flutter boundary (q as a function of σ/σ_{CR}) that goes to an unrealistic zero dynamic pressure at points of frequency coalescence for panels with length-width ratios greater than 1.0. The addition of aerodynamic damping improves the results somewhat; however, an exaggerated decrease in flutter dynamic pressure is still conspicuous at points of frequency coalescence.

Structural damping (that is, damping in harmonic motion which is proportional to amplitude and in phase with velocity in contrast to a viscous representation), in addition to aerodynamic damping, is used in two analytical models in the present paper. In the first model the structural damping coefficient modifies only the bending term. Calculated mode shapes and frequencies for an unstressed panel are used in the calculation which is hereafter called the zero-stress-mode solution. The advantages of this model are demonstrated in reference 6. In the second model, structural damping is assumed to be equally effective in both bending and compression as assumed in references 13, 14, and 15. Calculated mode shapes and frequencies for stressed panels are used in this calculation which is hereafter called the stressed-mode solution.

Flutter boundaries were calculated for panels 1 to 6 for a Mach number of 1.96. The panel properties are given in table I and the coordinate system is shown in figure 11. The aerodynamic loading was represented by linearized, two-dimensional aerodynamics, the aerodynamic damping term being retained (also known as "modified piston theory"). A brief outline of the two analyses, in which a Galerkin procedure is used, is presented. The integrals resulting from the derivation are given in appendix C.

Flutter Solution With Zero-Stress Modes

The differential equations of motion for small deflections of an isotropic panel subject to inplane loads with one side exposed to a supersonic airstream may be written as:

$$D \left(\frac{\partial^4 Z}{l^4 \partial \xi^4} + \frac{2}{l^2 w^2} \frac{\partial^4 Z}{\partial \xi^2 \partial \eta^2} + \frac{\partial^4 Z}{w^4 \partial \eta^4} \right) (1 + ig) + \frac{N_x}{l^2} \frac{\partial^2 Z}{\partial \xi^2} + \frac{N_y}{w^2} \frac{\partial^2 Z}{\partial \eta^2} + \gamma \frac{\partial^2 Z}{\partial t^2} = -\rho_1 \frac{V_1}{\beta_M} \left(\frac{\partial Z}{\partial t} + \frac{V_1}{l} \frac{\partial Z}{\partial \xi} \right) \quad (1)$$

where

$$\xi = \frac{x}{l}$$

$$\eta = \frac{y}{w}$$

g structural damping coefficient

N_x, N_y inplane loading in the x- and y-directions, positive in compression

$$\beta_M = \sqrt{M_1^2 - 1}$$

γ mass per unit area of panel

ρ_1 air density

V_1 velocity

The mode shapes that satisfy the boundary conditions for clamped edges with zero translation and with no airflow were calculated by using the equations of reference 7.

An approximate solution to equation (1) was obtained by a Galerkin procedure where the solution was taken to be of the form

$$Z(\xi, \eta, t) \approx \sum_{n=1}^N A_n X_n(\xi) Y_1(\eta) e^{i\omega t} \quad (2)$$

where X_n is the n th mode shape in the x -direction, Y_1 is the assumed mode shape (one half-wave) in the spanwise direction, and the coefficient A_n is, in general, complex. Substitution of equation (2) into equation (1), multiplication by Y_1 , and integration of the product with respect to η over the panel width results in the following ordinary differential equation:

$$\sum_{n=1}^N A_n w \left[D \left(\frac{1}{l^4} X_n^{IV} + \frac{2}{l^2 w^2} \frac{C_1}{C_0} X_n^{II} + \frac{1}{w^4} \frac{C_2}{C_0} X_n \right) (1 + ig) + \frac{N_x}{l^2} X_n^{II} + \frac{N_y}{w^2} \frac{C_1}{C_0} X_n - \omega^2 \gamma X_n + \rho_1 \frac{V_1}{\beta_M} \left(i\omega X_n + \frac{V_1}{l} X_n^I \right) \right] = 0 \quad (3)$$

where the Roman superscripts on X_n denote derivatives with respect to its argument ξ . By following the notation of reference 7,

$$\left. \begin{aligned} C_0 &= \int_{-1/2}^{1/2} [Y_1(\eta)]^2 d\eta \\ C_1 &= \int_{-1/2}^{1/2} Y_1^{II}(\eta) Y_1(\eta) d\eta \\ C_2 &= \int_{-1/2}^{1/2} Y_1^{IV}(\eta) Y_1(\eta) d\eta \end{aligned} \right\} \quad (4)$$

and the Roman superscripts on Y_1 indicate differentiation with respect to its argument η .

The differential equation for the free vibration of a panel with no inplane load consistent with the assumptions and notation used previously can be written as:

$$A_n D \left(\frac{1}{l^4} X_n^{IV} + \frac{2}{l^2 w^2} \frac{C_1}{C_0} X_n^{II} + \frac{1}{w^4} \frac{C_2}{C_0} X_n \right) = \gamma \omega_n^2 A_n X_n \quad (5)$$

which expresses the relationship between the elastic restoring forces and the normal-mode mass-inertia forces.

Substituting equation (5) into equation (3) is valid since the modes and frequencies of equation (5) are panel normal modes. The resulting equation is

$$\sum_{n=1}^N w \left\{ \left[\omega_n^2 (1 + ig) - \omega^2 \right] \gamma X_n + \frac{N_x}{l^2} X_n^{II} + \frac{N_y}{w^2} \frac{C_1}{C_0} X_n + \rho_1 \frac{V_1}{\beta_M} \left(i\omega X_n + \frac{V_1}{l} X_n^I \right) \right\} A_n = 0 \quad (6)$$

Continuation of the Galerkin procedure by multiplying equation (6) by $X_m(\xi)$ and integrating over the length results (when m is successively $1, 2, 3, \dots, N$) in a set of N simultaneous equations in matrix form:

$$\left[1 - \left(\frac{\omega_m}{\omega}\right)^2 (1 + ig) - \frac{C_1}{C_0} \frac{N_y}{\gamma w^2 \omega^2} - \frac{i}{\mu_1 k \beta_M} \right] \{A_m C_{mn}^{(3)}\} - \left[\frac{N_x C_{mn}^{(4)}}{\gamma l^2 \omega^2} + \frac{C_{mn}^{(5)}}{\mu_1 k^2 \beta_M} \right] \{A_n\} = 0$$

$$\left(\begin{array}{l} n = 1, 2, 3, 4, \dots, N; \\ m = 1, 2, 3, 4, \dots, N \end{array} \right) \quad (7)$$

where

$$k = \frac{l\omega}{V_1}$$

$$\mu_1 = \frac{\gamma}{\rho_1 l}$$

$$\beta_M = \sqrt{M_1^2 - 1}$$

$$\left. \begin{aligned} C_{mn}^{(3)} &= \int_{-1/2}^{1/2} X_m X_n d\xi & (=0 \text{ if } m \neq n) \\ C_{mn}^{(4)} &= \int_{-1/2}^{1/2} X_m X_n^{\Pi} d\xi \\ C_{mn}^{(5)} &= \int_{-1/2}^{1/2} X_m X_n^I d\xi \end{aligned} \right\} \quad (8)$$

For a nontrivial solution the determinant of the coefficients A_n must equal zero. As is discussed in appendix C, the determinant was first put into a lambda form since the frequency term $1/\omega^2$ appears in off-diagonal elements and then solved by means of a complex eigenvalue routine.

Flutter Solution With Stressed Modes

The differential equation for the stressed mode solution is:

$$\left[D \left(\frac{1}{l^4} \frac{\partial^4 Z}{\partial \xi^4} + \frac{2}{l^2 w^2} \frac{\partial^4 Z}{\partial \xi^2 \partial \eta^2} + \frac{\partial^4 Z}{w^4 \partial \eta^4} \right) + \frac{N_x}{l^2} \frac{\partial^2 Z}{\partial \xi^2} + \frac{N_y}{w^2} \frac{\partial^2 Z}{\partial \eta^2} \right] (1 + ig) + \gamma \frac{\partial^2 Z}{\partial t^2} = -\rho_1 \frac{V_1}{\beta_M} \left(\frac{\partial Z}{\partial t} + \frac{V_1}{l} \frac{\partial Z}{\partial \xi} \right) \quad (9)$$

Equation (9) is similar to equation (1) except that in equation (9) the structural damping for inplane compressive vibration is assumed to be equal to that for flexural vibration, both being multiplied by $1 + ig$.

Equation (9) was reduced to an ordinary differential equation as described in the previous section. The differential equation for the free vibration of a panel subject to inplane loads can be written as:

$$A_n D \left(\frac{1}{l^4} X_n^{(IV)} + \frac{2}{l^2 w^2} \frac{C_1}{C_0} X_n'' + \frac{1}{w^4} \frac{C_2}{C_0} X_n + \frac{N_x}{l^2} X_n'' + \frac{N_y}{w^2} \frac{C_1}{C_0} X_n \right) = \gamma \omega_n^2 A_n X_n \quad (10)$$

The ordinary differential equation becomes

$$\sum_{n=1}^N w \left\{ \left[\omega_n^2 (1 + ig) - \omega^2 \right] \gamma X_n + \rho_1 \frac{V_1}{\beta_M} i \omega X_n + \frac{V_1}{l} X_n' \right\} A_n = 0 \quad (11)$$

Multiplying by $X_m(\xi)$ and integrating along the length results in the following N simultaneous equations in matrix form that express the dynamic equilibrium of flutter:

$$\left[\left(\frac{\omega_r}{\omega_m} \right)^2 \left(1 - \frac{i}{\mu_1 k^2 \beta_M} \right) - \Omega \right] \{ C_{mn}^{(3)} A_m \} - \left[\left(\frac{\omega_r}{\omega_m} \right)^2 \frac{1}{\mu_1 k^2 \beta_M} C_{mn}^{(5)} \right] \{ A_n \} = 0$$

$$\left(\begin{array}{l} n = 1, 2, 3, \dots, N; \\ m = 1, 2, 3, \dots, N \end{array} \right) \quad (12)$$

and

$$\Omega = \left(\frac{\omega_r}{\omega} \right)^2 (1 + ig)$$

$$\omega_r = \sqrt{\frac{\pi^4 D}{l^4 \gamma}}$$

DISCUSSION OF ANALYTICAL FLUTTER RESULTS AND COMPARISON WITH EXPERIMENT

The flutter boundary calculations of this investigation were highly dependent on both structural and aerodynamic damping. Retention of the aerodynamic damping term had a stabilizing effect. The ratios of the flutter dynamic pressure calculated with aerodynamic damping to the calculated result without damping, and the corresponding frequency

ratios are given as functions of length-width ratio in figure 12. Structural damping and stress ratio were both zero for the calculations which were made by use of the zero-stress mode equations. Since aerodynamic damping is frequency dependent and since the natural frequencies of the panels increase with increasing length-width ratio (fig. 7), an increase in aerodynamic damping with length-width ratio is not surprising. Some insight into the large variation of the results in figure 12 may be obtained by considering the aerodynamic damping coefficient g_a utilized in reference 16 for a semi-infinite panel:

$$g_a = \frac{\rho_1 a_1}{\gamma \omega} \frac{\omega}{\omega_r} \quad (13a)$$

which can be written as

$$g_a = \frac{\rho_1 a_1 l^2}{\pi^2 \sqrt{D} \gamma} \quad (13b)$$

The ratio of g_a for the panels to that for panel 1 for a constant dynamic pressure is given in figure 13 for the panels in figure 12. Since the lengths of the panels are the same with the exception of panel 1, the variation of g_a among the other four panels in figure 13 is due to panel thickness in D and γ .

The calculated flutter dynamic pressure for zero aerodynamic and structural damping agreed with the values computed from reference 17. The convergence of the present solutions was tested by increasing the number of modes used in the solution until the calculations gave small differences in the dynamic pressure and flutter frequency with increased number of modes. Eight modes were used for panels 1, 2, and 3; 10 modes for panel 4; and 16 modes were used for panels 5 and 6. The results of reference 17 were determined from a closed-form solution to the panel flutter equations and are based on the assumption of a spanwise mode, no damping, and piston-theory aerodynamic loading.

Three flutter boundaries were calculated for panels 1 to 6 and are compared with the experimental data for $M_1 = 1.96$ in figure 14 in terms of flutter dynamic pressure as a function of stress ratio. The calculated and experimental flutter frequencies are also given as a function of stress ratio in figure 14. Two of the flutter boundaries were determined by using a structural damping coefficient g of 0.05 in the stress-mode and zero-stress-mode calculations. A structural damping coefficient of 0.05 was used since it was the upper limit for the bulk of the damping data. The third boundary was determined by using zero structural damping in a zero-stress-mode calculation. The aerodynamic damping term was retained in the calculations of all three boundaries.

The flutter boundary for the case of zero structural damping is shown as a dashed line in figures 14(a) to 14(f). For panels 2 to 6, the flutter boundary is similar to a

boundary in which aerodynamic damping is also neglected in that the boundary goes nearly to zero at points of frequency coalescence. This tendency is not noted in the experimental data.

The flutter boundaries for the two calculations in which structural damping was retained are the same at low values of stress ratio. For panels 2 to 6 structural damping is stabilizing. As the stress ratio is increased, the two boundaries separate. The boundary from the stressed-mode solution (long dash) becomes irregular for panels with length-width ratios greater than 1.0. The zero-stress-mode boundary (solid line) remains smooth for all values of stress ratio and except for panel 1, the dynamic pressure at flutter is greater beyond the point where the boundaries separated. At the higher values of stress ratio (approaching 1.0), structural damping becomes less effective in the stressed-mode solution and for panels 2 to 6 the results are essentially the same as those with a structural damping of zero. In contrast to the flutter dynamic pressure, the flutter frequencies from the two sets of calculations were in good agreement.

The calculated results for panel 1 ($l/w = 1$) are substantially different from the calculated results of the other five panels, in that the addition of structural damping was destabilizing for both types of calculations. This result is not uncommon in lifting-surface flutter (ref. 18) or in panel flutter (ref. 19). The effect of structural damping was more pronounced in the zero-stress-mode calculations. The experimental data of panel 1 fall uniformly below the calculated values of flutter dynamic pressure over the whole range of stress ratio σ/σ_{CR} in contrast to the results of the other five panels.

The experimental data of panels 2 to 6 have the same general trend in the variation of dynamic pressure with σ/σ_{CR} as the calculated data and the minimum experimental levels are in fair agreement with the zero-stress-mode calculations for $g = 0.05$. However, there are some large differences between the calculated and experimental results at low levels of σ/σ_{CR} where the experimental results are confused by the occurrence of high-frequency flutter.

With the exception of the high-frequency flutter, the bulk of the measured flutter frequencies were in fair agreement with the calculated values up to a stress ratio of about 0.70. Beyond this stress ratio the calculated flutter frequencies decreased more rapidly than the experimental data and go to zero above stress ratios of 1.0.

A comparison of experimental and calculated results (zero-stress-mode shape calculation with a structural damping coefficient of 0.05) for $M_1 = 1.96$ is given in figure 15. The results are given in terms of the parameter $\lambda^{1/3} \frac{w}{l}$ (where

$\lambda^{1/3} \frac{w}{l} = \left(\frac{2gw^3}{\beta M^2 D} \right)^{1/3}$) as a function of length-width ratio for two conditions. The

calculated boundary for the minimum dynamic pressure with inplane streamwise load is shown as a solid line. The calculated boundary for zero inplane load is shown as a dashed line. The experimental data symbols are coded by panel thickness.

As was discussed in the analysis section, a damping coefficient of 0.05 was chosen as an upper bound since the bulk of the measured damping coefficients fell below that value. The calculated results for the minimum flutter dynamic pressure reflect this choice in damping coefficient in that they are an upper bound to the experimental flutter data. A better fit of the calculated values to the experimental data would have been obtained if measured damping coefficients at all stress ratios had been used.

The high-frequency flutter confused the experimental results near a stress ratio of zero. The limited experimental data at $\sigma/\sigma_{CR} = 0$ shown in figure 15 that are compatible with the linear theory used in the present paper are the result of extrapolation. The region of the high-frequency flutter at $\sigma/\sigma_{CR} = 0$ is shown as a shaded area in figure 15.

CONCLUSIONS

An experimental and analytical study has been conducted of the flutter characteristics of flat panels that were constructed with practical edge conditions. Thirteen panels were subjected to streamwise inplane loads and the study covered Mach numbers of 1.96 and 1.57. The flutter boundaries for six of these panels were calculated by using two-dimensional quasi-steady aerodynamics. Aerodynamic and structural damping were included in the formulation of the problem which was solved by use of a Galerkin procedure. Structural damping was considered in two ways: effective in bending only, and effective in both bending and inplane compression. The investigation leads to the following conclusions:

1. The dynamic pressure at the onset of flutter decreased rapidly by 80 to 90 percent with increasing streamwise inplane compressive stress. For panels with length-width ratios greater than 1, the minimum flutter dynamic pressure occurred at compressive stresses that were somewhat less than the buckling stress, and the dynamic pressure subsequently increased when the panel was loaded beyond the buckling stress.

2. Damping, both aerodynamic and structural, was found to have a pronounced effect on the calculated flutter boundary.

3. The agreement between analysis and experiment depended on structural damping and the manner in which it was introduced into the formulation of the problem. Calculations in which structural damping was introduced only in the panel-bending terms resulted in good agreement with experimental trends.

4. Limited examination of the effects of static-pressure differential acting across the panel indicated that static-pressure difference increased the inplane load required to cause buckling and resulted in an increase of the minimum flutter dynamic pressure by up to a factor of eight for the particular panel tested.

5. Natural frequencies, mode shapes, and structural damping were measured for five of the panels at levels of inplane stress and ambient pressure that corresponded to the flutter condition. It was found to be impractical to map with sufficient accuracy and detail the number of mode shapes required for flutter calculations over the range of inplane stress of the flutter tests.

6. Measured structural damping varied over a range from about 0.012 to 0.05 for variations in panel geometry, mode, inplane stress, and ambient pressure.

Langley Research Center,
National Aeronautics and Space Administration,
Langley Station, Hampton, Va., October 20, 1969.

APPENDIX A

LOCAL FLOW CONDITIONS

Local flow conditions were measured with an 0.5-inch-thick (1.27 cm) calibration plate which was machined at the edges to fit the cavity so that its surface was flush with the splitter plate. Eighteen static-pressure orifices were located 2 inches (5.08 cm) apart and 3 inches (7.62 cm) below the stream-aligned center line of the plate. A 1-psi (6895-N/m²) pressure gage was used to measure fluctuating pressures and was located 6 inches (15.24 cm) aft of the vertical center line and 3 inches (7.62 cm) above the stream-aligned center line. Provision was made to mount a boundary-layer rake on the center line at the leading and trailing edge of the plate.

The pressure distributions for two levels of dynamic pressure at local Mach numbers M_1 of 1.96 and 1.57 are shown in figure 16. No values of Δp are given at the trailing edge of the plate because this area was in the wake of the boundary-layer rake. Pressure spectra, from 0 to 600 Hz, and overall levels expressed as ratios to dynamic pressure squared p_{rms} are shown in figure 17.

The pressure differential measurements in figure 16 show that at a local Mach number of 1.57, pressure differentials are two to three times greater than at a local Mach number of 1.96. The fluctuating pressure levels (fig. 17) were higher at a Mach number of 1.57 than at a Mach number of 1.96 in the frequency range of the flutter test results. The difference in overall levels is of the order that would be expected for this Mach number range in turbulent flow. (See ref. 20, for example.)

The minimum Reynolds number, based on the distance from the leading edge of the splitter plate to the leading edge of the panel and minimum stagnation pressure, was approximately 1.3×10^6 at a Mach number of 1.96. The boundary-layer thickness ranged from 0.8 inch (2.03 cm) to 1.75 inches (4.445 cm) for the two Mach numbers at stagnation pressures of 718 psf (34.378 kN/m²) and 2160 psf (103.42 kN/m²).

APPENDIX B

MODE-SHAPE MEASURING APPARATUS AND PROCEDURES

The vibration data measurements were made in the 55-foot (16.764-m) vacuum chamber of the Langley dynamics research laboratory. In order to measure panel mode shapes remotely, a system was designed that incorporated a means of systematically handling a large volume of data.

Apparatus

A photograph of the splitter plate and the mode-shape measuring apparatus is shown in figure 18. Three 2-pound (8.90 N) shakers were positioned so that the first six streamwise bending vibration modes, with one half-wave in the cross-stream direction, could be excited. A small length of compliant plastic tubing was attached to the shaker driving spindle. The shakers were mounted so that a 0.003-inch (0.00762 cm) gap existed between the plastic tubing and the panel. When the panel was vibrated in a given mode, the spindles of the coils of the two inactive shakers were drawn back from the panel by a dc bias voltage on the shaker coils. The carriage shown in figure 18 transported a displacement detector either continuously or incrementally by remote control by use of two independent coordinate drive systems. The variable reluctance detector was automatically maintained at 0.02 inch (0.0508 cm) from the panel surface. The ac analog signal from the detector was converted to a dc voltage for readout on a x-y plotter and a digital voltmeter. In order to minimize error caused by electronic noise, an error null circuit was used at the output of the ac-dc converter. This circuit provided a dc voltage equal in amplitude and opposite in polarity to the electronic noise signal.

A reference displacement detector provided a continuous record of surface displacement at a point for the period of time necessary to map the mode shape of the upper half of the panel and thus provided the reference needed to correct the measured data for any variation in response amplitude with time. A reference detector was also used to provide a response phase relationship over the vibrating surface.

Procedure

The vacuum chamber was evacuated to a density equal to the static air density of a point on the flutter boundary and the corresponding inplane load was applied. After a preliminary mode-shape search was made in the continuous mode of the carriage operation, data were taken in the incremental mode of operation in which the detector moved in pre-set increments over the panel. The amplitude, reference amplitude, phase, and surface

APPENDIX B

coordinates were automatically punched on cards at each point. The amplitude, phase, and one coordinate were also plotted simultaneously on the x-y plotter for visual reference.

A program using Fourier series analysis was used to fit a curve through the data. A typical example is shown in figure 19 where the large symbols are the measured data and the small dots were obtained from the curve-fitting program.

There were practical limitations to the mapping of the mode shapes of a panel under inplane load. The region of stress above the coalescence of the first two modes presents a problem because of the number of modes within a narrow range of frequencies of a damped system. Also, a very slight change in stress, due to small changes in temperature for instance, caused the panel response to shift mode at a given frequency. As may be observed by referring to figure 7, the problem becomes increasingly severe with increasing length-width ratio. A system limitation was the inability to excite the first two modes at a length-width ratio of 3.77 and modes above the third for a length-width ratio of 1.0. It might have been possible to excite these modes if the system had been designed for a multiple shaker input in which a system in which the force is proportional to the deflection allows the use of multiple shakers without mode-shape distortion.

As may be apparent from the foregoing discussion, the mapping of a sufficient number of panel modes over a wide range of stress conditions with sufficient accuracy for use in flutter calculations presents a formidable task even for one panel and was found to be impractical. The system was useful for comparison of experimental mode shapes and frequencies with computed values and the determination of panel damping for the conditions of the flutter experiments.

APPENDIX C

DETAILS OF FLUTTER SOLUTION

Zero-Stress-Mode Solution

Since the flutter frequency appears as $1/\omega^2$ in the off-diagonal as well as the diagonal elements in equation (7), the determinant of the coefficients was first put into a lambda form in which the eigenvalue, $\lambda = 1/\omega^2$, appears only in the diagonal elements.

The determinant of the coefficients of equation (7) is in the form

$$|A - C\lambda| = 0 \quad (C1)$$

where A and C are complex. The determinant is in the desired form when

$$|D - \lambda| = 0 \quad (C2)$$

where

$$[\bar{D}] = [\bar{C}]^{-1}[\bar{A}] \quad (C3)$$

To invert the matrix $[\bar{C}]$ by using real arithmetic procedures, the elements are separated into their real and imaginary parts. Rewriting equation (C3) in this form yields:

$$[\bar{c} + i\bar{\gamma}][\bar{d} + i\bar{\delta}] = [\bar{a} + i\bar{\alpha}] \quad (C4)$$

The bar denotes a submatrix and here the Greek letters are used to denote the imaginary part of the complex matrix. Multiplying the terms and the left-hand side of equation (C4), and then equating the real and imaginary parts results in a matrix equation that yields the real and imaginary parts of $[\bar{D}]$

$$\begin{Bmatrix} \bar{d} \\ \bar{\delta} \end{Bmatrix} = \begin{bmatrix} \bar{c} & -\bar{\gamma} \\ \bar{\gamma} & \bar{c} \end{bmatrix}^{-1} \begin{Bmatrix} \bar{a} \\ \bar{\alpha} \end{Bmatrix} \quad (C5)$$

The submatrices of equation (C5) expressed in the terms of equation (7) are:

APPENDIX C

$$\left. \begin{aligned}
 \bar{a} &= - \left[C_{mn}^{(3)} \right] + \left[\frac{C_{mn}^{(5)}}{\mu_1 \beta_M k^2} \right] \\
 \bar{\alpha} &= \left[\frac{C_{mn}^{(3)}}{\mu_1 \beta_M k} \right] \\
 \bar{c} &= \left[C_{mn}^{(3)} \left(-\omega_m^2 - \frac{N_y}{\gamma w^2} \frac{C_1}{C_0} \right) \right] - \left[\frac{N_x C_{mn}^{(4)}}{\gamma l^2} \right] \\
 \bar{\gamma} &= - \left[\omega_m^2 g C_{mn}^{(3)} \right]
 \end{aligned} \right\} \quad (C6)$$

In matrix form these equations become, for a four-mode solution:

$$\bar{a} = \begin{bmatrix} -D_{PS(1)} & \frac{C_{PSA(1,2)}}{\mu_1 \beta_M k^2} & 0 & \frac{C_{PSA(1,4)}}{\mu_1 \beta_M k^2} \\ \frac{C_{PAS(2,1)}}{\mu_1 \beta_M k^2} & -D_{PA(2)} & \frac{C_{PAS(2,3)}}{\mu_1 \beta_M k^2} & 0 \\ 0 & \frac{C_{PSA(3,2)}}{\mu_1 \beta_M k^2} & -D_{PS(3)} & \frac{C_{PSA(3,4)}}{\mu_1 \beta_M k^2} \\ \frac{C_{PAS(4,1)}}{\mu_1 \beta_M k^2} & 0 & \frac{C_{PAS(4,3)}}{\mu_1 \beta_M k^2} & -D_{PA(4)} \end{bmatrix} \quad (C7a)$$

$$\bar{\alpha} = \begin{bmatrix} \frac{\bar{D}_{PS(1)}}{\mu_1 \beta_M k} & 0 & 0 & 0 \\ 0 & \frac{D_{PA(2)}}{\mu_1 \beta_M k} & 0 & 0 \\ 0 & 0 & \frac{D_{PS(3)}}{\mu_1 \beta_M k} & 0 \\ 0 & 0 & 0 & \frac{D_{PA(4)}}{\mu_1 \beta_M k} \end{bmatrix} \quad (C7b)$$

APPENDIX C

where

$$D_{PS}^{(m)} = C_{mn}^{(3)} \quad (\text{Lengthwise symmetric modes; } m \text{ is odd})$$

$$D_{PA}^{(m)} = C_{mn}^{(3)} \quad (\text{Lengthwise asymmetric modes; } m \text{ is even})$$

$$C_{PSA}^{(m,n)} = C_{mn}^{(5)} \quad (m \text{ is odd; } n \text{ is even})$$

$$C_{PAS}^{(m,n)} = C_{mn}^{(5)} \quad (m \text{ is even; } n \text{ is odd})$$

$$\bar{c} = \begin{bmatrix} (-\omega_1^2 - \bar{N}_y) D_{PS}^{(1)} & 0 & -N_x C_{SS2}^{(1,3)} & 0 \\ -\bar{N}_x C_{SS}^{(1)} & & & \\ 0 & (-\omega_2^2 - \bar{N}_y) D_{PA}^{(2)} & 0 & -\bar{N}_x C_{AA2}^{(2,4)} \\ & -\bar{N}_x C_{AA}^{(2)} & & \\ -N_x C_{SS2}^{(3,1)} & 0 & (-\omega_3^2 - \bar{N}_y) D_{PS}^{(3)} & 0 \\ & & -N_x C_{SS}^{(3)} & \\ 0 & -\bar{N}_x C_{AA2}^{(4,2)} & 0 & (-\omega_4^2 - \bar{N}_y) D_{PA}^{(4)} \\ & & & -\bar{N}_x C_{AA}^{(4,4)} \end{bmatrix} \quad (C7c)$$

$$\bar{\gamma} = \begin{bmatrix} -\omega_1^2 g D_{PS}^{(1)} & 0 & 0 & 0 \\ 0 & -\omega_2^2 g D_{PA}^{(2)} & 0 & 0 \\ 0 & 0 & -\omega_3^2 g D_{PA}^{(3)} & 0 \\ 0 & 0 & & -\omega_4^2 g D_{PA}^{(4)} \end{bmatrix} \quad (C7d)$$

APPENDIX C

where

$$\bar{N}_x = \frac{N_x}{\gamma l^2}$$

$$\bar{N}_y = \frac{N_y}{\gamma w^2} \frac{C_1}{C_0}$$

$$C_{SS}(m) = C_{mn}^{(4)} \quad (m = n, \text{ odd})$$

$$C_{SS2}(m,n) = C_{mn}^{(4)} \quad (m \neq n, \text{ odd})$$

$$C_{AA}(m) = C_{mn}^{(4)} \quad (m = n, \text{ even})$$

$$C_{AA2}(m,n) = C_{mn}^{(4)} \quad (m \neq n, \text{ even})$$

The mode shapes used in the calculations from equation (18) of reference 7 are:

$$\left. \begin{aligned} X_S &= \cos 2\alpha\xi - \frac{\cos \alpha}{\cosh \beta} \cosh 2\beta\xi && \text{(Symmetric modes)} \\ X_A &= \sin 2\alpha\xi - \frac{\sin \alpha}{\sinh \beta} \sinh 2\beta\xi && \text{(Asymmetric modes)} \end{aligned} \right\} \quad (C8)$$

The integers in equations (C7) designate the mode number of the arguments α and β which are defined in reference 7. Coefficients resulting from the integration of the products of the mode shapes over the length of the panel are given below.

$$D_{PS}(m) = S_{R2}(\alpha_m) - \frac{2 B_B(\alpha_m, \beta_m) R_1(\alpha_m, \beta_m)}{C_C(\alpha_m, \beta_m)} + S_{R3}(\beta_m) B_B^2(\alpha_m, \beta_m) \quad (C9a)$$

$$D_{PA}(m) = S_{R1}(\alpha_m) - \frac{2 D(\alpha_m, \beta_m) R_2(\alpha_m, \beta_m)}{C_C(\alpha_m, \beta_m)} - S_{R4}(\beta_m) D^2(\alpha_m, \beta_m) \quad (C9b)$$

APPENDIX C

$$\begin{aligned}
 C_{PAS}(m,n) = & -A_{L1}(\alpha_m, \alpha_n) + \frac{2 D(\alpha_m, \beta_m) A_{LL1}(\alpha_n, \beta_m)}{A_{AA}(\alpha_n, \beta_m)} - \frac{2 A_A(\alpha_n, \beta_n) B_{AA1}(\alpha_m, \beta_n)}{B_{BB}(\alpha_m, \beta_n)} \\
 & + A_A(\alpha_n, \beta_n) D(\alpha_m, \beta_m) B_{BB1}(\beta_m, \beta_n)
 \end{aligned} \tag{C9c}$$

$$\begin{aligned}
 C_{PSA}(m,n) = & A_{L2}(\alpha_m, \alpha_n) - \frac{2 B_B(\alpha_m, \beta_m) A_{LL2}(\alpha_n, \beta_m)}{A_{AA}(\alpha_n, \beta_m)} - \frac{2 C(\alpha_n, \beta_n) B_{AA2}(\alpha_m, \beta_n)}{B_{BB}(\alpha_m, \beta_n)} \\
 & + B_B(\alpha_m, \beta_m) C(\alpha_n, \beta_n) B_{BB2}(\beta_m, \beta_n)
 \end{aligned} \tag{C9d}$$

$$\begin{aligned}
 C_{SS}(m) = & -4 S_{R2}(\alpha_m) \alpha_m^2 + 4 S_{R3}(\beta_m) B_B^2(\alpha_m, \beta_m) \beta_m^2 \\
 & + \frac{4 B_B(\alpha_m, \beta_m) E_E(\alpha_m, \beta_m) R_1(\alpha_m, \beta_m)}{C_C(\alpha_m, \beta_m)}
 \end{aligned} \tag{C9e}$$

$$\begin{aligned}
 C_{AA}(m) = & -4 S_{R1}(\alpha_m) \alpha_m^2 - 4 S_{R4}(\beta_m) D^2(\alpha_m, \beta_m) \beta_m^2 \\
 & + \frac{4 D(\alpha_m, \beta_m) E_E(\alpha_m, \beta_m) R_2(\alpha_m, \beta_m)}{C_C(\alpha_m, \beta_m)}
 \end{aligned} \tag{C9f}$$

$$\begin{aligned}
 C_{SS2}(m,n) = & - \frac{2 \alpha_n A_{L2}(\alpha_m, \alpha_n) - 4 A_A(\alpha_n, \beta_n) \beta_n B_{AA2}(\alpha_m, \beta_n)}{B_{BB}(\alpha_m, \beta_n)} \\
 & + \frac{4 \alpha_n B_B(\alpha_m, \beta_m) A_{LL2}(\alpha_n, \beta_m)}{A_{AA}(\alpha_n, \beta_m)} + 2 \beta_n A_A(\alpha_n, \beta_n) B_B(\alpha_m, \beta_m) B_{BB2}(\beta_m, \beta_n)
 \end{aligned} \tag{C9g}$$

APPENDIX C

$$C_{AA2}(m,n) = - \frac{2 \alpha_n A_{L1}(\alpha_m, \alpha_n) - 4 C(\alpha_n, \beta_n) \beta_n B_{AA1}(\alpha_m, \beta_n)}{B_{BB}(\alpha_m, \beta_n)} + \frac{4 \alpha_n D(\alpha_m, \beta_m) A_{LL1}(\alpha_n, \beta_m)}{A_{AA}(\alpha_n, \beta_m)} + 2 \beta_n C(\alpha_n, \beta_n) D(\alpha_m, \beta_m) B_{BB1}(\beta_m, \beta_n) \quad (C9h)$$

where

$$S_{R1}(\alpha_m) = \frac{0.5 - \sin 2\alpha_m}{4\alpha_m} \quad (C10a)$$

$$S_{R2}(\alpha_m) = \frac{0.5 + \sin 2\alpha_m}{4\alpha_m} \quad (C10b)$$

$$S_{R3}(\beta_m) = \frac{0.5 + \sinh 2\beta_m}{4\beta_m} \quad (C10c)$$

$$S_{R4}(\beta_m) = \frac{0.5 - \sinh 2\beta_m}{4\beta_m} \quad (C10d)$$

$$S_{R5}(\beta_m) = \frac{0.5 + \sin 2\beta_m}{4\beta_m} \quad (C10e)$$

$$S_{R6}(\beta_m) = \frac{0.5 - \sin 2\beta_m}{4\beta_m} \quad (C10f)$$

$$R_1(\alpha_m, \beta_m) = \alpha_m \sin \alpha_m \cosh \beta_m + \beta_m \cos \alpha_m \sinh \beta_m \quad (C10g)$$

$$R_2(\alpha_m, \beta_m) = \beta_m \sin \alpha_m \cosh \beta_m - \alpha_m \cos \alpha_m \sinh \beta_m \quad (C10h)$$

$$A_{L1}(\alpha_m, \alpha_n) = \alpha_n \left(\frac{\sin \alpha_n - \alpha_m}{\alpha_n - \alpha_m} - \frac{\sin \alpha_n + \alpha_m}{\alpha_n + \alpha_m} \right) \quad (C10i)$$

$$A_{L2}(\alpha_m, \alpha_n) = \alpha_n \left(\frac{\sin \alpha_n + \alpha_m}{\alpha_n + \alpha_m} + \frac{\sin \alpha_n - \alpha_m}{\alpha_n - \alpha_m} \right) \quad (C10j)$$

APPENDIX C

$$A_{LL1}(\alpha_n, \beta_m) = \alpha_n (\beta_m \sin \alpha_n \cosh \beta_m - \alpha_n \cos \alpha_n \sinh \beta_m) \quad (C10k)$$

$$A_{LL2}(\alpha_n, \beta_m) = \alpha_n (\beta_m \cos \alpha_n \sinh \beta_m + \alpha_n \sin \alpha_n \cosh \beta_m) \quad (C10l)$$

$$B_{AA1}(\alpha_m, \beta_n) = \beta_n (\beta_n \sin \alpha_m \cosh \beta_n - \alpha_m \cos \alpha_m \sinh \beta_n) \quad (C10m)$$

$$B_{AA2}(\alpha_m, \beta_n) = \beta_n (\beta_n \cos \alpha_m \sinh \beta_n + \alpha_m \sin \alpha_m \cosh \beta_n) \quad (C10n)$$

$$B_{BB1}(\beta_m, \beta_n) = \beta_n \left[\frac{\sinh(\beta_n + \beta_m)}{\beta_n + \beta_m} - \frac{\sinh(\beta_n - \beta_m)}{\beta_n - \beta_m} \right] \quad (C10o)$$

$$B_{BB2}(\beta_m, \beta_n) = \beta_n \left[\frac{\sinh(\beta_n + \beta_m)}{\beta_n + \beta_m} + \frac{\sinh(\beta_n - \beta_m)}{\beta_n - \beta_m} \right] \quad (C10p)$$

$$A_A(\alpha_n, \beta_n) = \frac{\cos \alpha_n}{\cosh \beta_n} \quad (C10q)$$

$$B_B(\alpha_m, \beta_m) = \frac{\cos \alpha_m}{\cosh \beta_m} \quad (C10r)$$

$$C(\alpha_n, \beta_n) = \frac{\sin \alpha_n}{\sinh \beta_n} \quad (C10s)$$

$$D(\alpha_m, \beta_m) = \frac{\sin \alpha_m}{\sinh \beta_m} \quad (C10t)$$

$$A_{AA}(\alpha_n, \beta_m) = \alpha_n^2 + \beta_m^2 \quad (C10u)$$

$$B_{BB}(\alpha_m, \beta_n) = \alpha_m^2 + \beta_n^2 \quad (C10v)$$

$$C_C(\alpha_m, \beta_m) = \alpha_m^2 + \beta_m^2 \quad (C10w)$$

$$E_E(\alpha_m, \beta_m) = \alpha_m^2 - \beta_m^2 \quad (C10x)$$

The lambda determinant (eq. (C2)) was solved by means of a QR algorithm. The solution for a given panel, stress ratio, and air density was the value of $k \left(\frac{L\omega}{V_1} \right)$ that

APPENDIX C

caused the imaginary frequency to be zero. The value of air density used in the calculations corresponded to the experimental density.

At low stress levels where there was no low-frequency flutter data, the initial value of dynamic pressure, and hence air density, was determined from an extrapolation of the experimental low-frequency flutter boundary. At these stress levels, the calculated flutter dynamic pressure was often higher than the dynamic pressure of the extrapolation. It was found that increasing the density in the calculations resulted in decreasing difference between the input and calculated density. Since the experimental data were obtained under variable density and constant velocity conditions, the appropriate flutter boundary was considered to be that which resulted in a constant flutter velocity.

Stressed-Mode Solution

The stressed-mode shapes and frequencies used in equation (12) were calculated by using the equations of reference 7. As was briefly discussed in the section dealing with panel frequencies, the equations fall into two regions, depending on panel geometry and inplane load. The parameter that governs which mode shape equations are used for a given mode of an isotropic panel is

$$\bar{B} = \left(\frac{\omega_m}{\omega_r}\right)^2 - \left(\frac{l}{w}\right)^2 \left(\frac{1}{\pi^4} \frac{C_2}{C_0} + \frac{N_x w^2}{\pi^2 D} \frac{C_1}{C_0}\right) \quad (C11)$$

where

$$\omega_r = \sqrt{\frac{\pi^4 D}{l^4 \gamma}}$$

The value of \bar{B} for a given mode decreases with increasing midplane compressive stress, and for the lower modes, becomes negative. The mode-shape equations (ref. 7, eqs. (18) and (19)) for \bar{B} positive and negative (eqs. (C8)) are

$$\left. \begin{aligned} X_S &= \cos 2\alpha \xi - \frac{\cos \alpha}{\cosh \beta} \cosh 2\beta \xi && \text{(Symmetrical; } \bar{B} \text{ positive)} \\ X_A &= \sin 2\alpha \xi - \frac{\sin \alpha}{\sinh \beta} \sinh 2\beta \xi && \text{(Asymmetrical; } \bar{B} \text{ positive)} \end{aligned} \right\} \quad (C12a)$$

$$\left. \begin{aligned} X_S &= \cos 2\alpha \xi - \frac{\cos \alpha}{\cos \bar{\beta}} \cos 2\bar{\beta} \xi && \text{(Symmetrical; } \bar{B} \text{ negative)} \\ X_A &= \sin 2\alpha \xi - \frac{\sin \alpha}{\sin \bar{\beta}} \sin 2\bar{\beta} \xi && \text{(Asymmetrical; } \bar{B} \text{ negative)} \end{aligned} \right\} \quad (C12b)$$

APPENDIX C

The arguments, α and β or $\bar{\beta}$, and the frequencies were calculated for panels 1 to 6 for stress-ratio increments of 0.10 between 0 and 0.30 and in increments of 0.05 from 0.30 to 1.0.

A sample determinant is given for which \bar{B} is negative for the first two modes. The terms in this determinant would correspond to the first 4 by 4 terms of panel 2 at a stress ratio of 0.60.

$$\begin{vmatrix}
 D_R(1) - \Omega & \frac{\bar{K}(1) C_{NSA}(1,2)}{D_{NS}(1)} & 0 & \frac{\bar{K}(1) C_{NPSA}(1,4)}{D_{NS}(1)} \\
 \frac{\bar{K}(2) C_{NAS}(2,1)}{D_{NA}(2)} & D_R(2) - \Omega & \frac{\bar{K}(2) C_{NPAS}(2,3)}{D_{NA}(2)} & 0 \\
 0 & \frac{\bar{K}(3) C_{PNSA}(3,2)}{D_{PS}(3)} & D_R(3) - \Omega & \frac{\bar{K}(3) C_{PSA}(3,4)}{D_{PS}(3)} \\
 \frac{\bar{K}(4) C_{PNAS}(4,1)}{D_{PA}(4)} & 0 & \frac{\bar{K}(4) C_{PAS}(4,3)}{D_{PA}(4)} & D_R(4) - \Omega
 \end{vmatrix} = 0 \quad (C13)$$

$$\left. \begin{aligned}
 D_R(m) &= \left(\frac{\omega_r}{\omega_m}\right)^2 \left(1 - \frac{i}{\mu_1 k^2 \beta_m}\right) \\
 \Omega &= \left(\frac{\omega_r}{\omega}\right)^2 (1 + ig) \\
 \bar{K}(m) &= -\left(\frac{\omega_r}{\omega_m}\right)^2 \frac{1}{\mu_1 k^2 \beta_m}
 \end{aligned} \right\} \quad (C14)$$

$$D_{NS}(m) = C_{mn}^{(3)} \quad (m = 1, 3, 5, \dots; \bar{B} \text{ negative}) \quad (C15a)$$

$$D_{NA}(m) = C_{mn}^{(3)} \quad (m = 2, 4, 6, \dots; \bar{B} \text{ negative}) \quad (C15b)$$

$$D_{PS}(m) = C_{mn}^{(3)} \quad (m = 1, 3, 5, \dots; \bar{B} \text{ positive}) \quad (C15c)$$

$$D_{PA}(m) = C_{mn}^{(3)} \quad (m = 2, 4, 6, \dots; \bar{B} \text{ positive}) \quad (C15d)$$

APPENDIX C

$$C_{\text{NSA}}(m,n) = C_{mn}^{(5)} \quad (m = 1,3,5,\dots; n = 2,4,6,\dots; \bar{B} \text{ negative}) \quad (\text{C15e})$$

$$C_{\text{NAS}}(m,n) = C_{mn}^{(5)} \quad (m = 2,4,6,\dots; n = 1,3,5,\dots; \bar{B} \text{ negative}) \quad (\text{C15f})$$

$$C_{\text{PSA}}(m,n) = C_{mn}^{(5)} \quad (m = 1,3,5,\dots; n = 2,4,6,\dots; \bar{B} \text{ positive}) \quad (\text{C15g})$$

$$C_{\text{PAS}}(m,n) = C_{mn}^{(5)} \quad (m = 2,4,6,\dots; n = 1,3,5,\dots; \bar{B} \text{ positive}) \quad (\text{C15h})$$

$$C_{\text{NPSA}}(m,n) = C_{mn}^{(5)} \quad \begin{pmatrix} m = 1,3,5,\dots; \bar{B} \text{ negative} \\ n = 2,4,6,\dots; \bar{B} \text{ positive} \end{pmatrix} \quad (\text{C15i})$$

$$C_{\text{NPAS}}(m,n) = C_{mn}^{(5)} \quad \begin{pmatrix} m = 2,4,6,\dots; \bar{B} \text{ negative} \\ n = 1,3,5,\dots; \bar{B} \text{ positive} \end{pmatrix} \quad (\text{C15j})$$

$$C_{\text{PNSA}}(m,n) = C_{mn}^{(5)} \quad \begin{pmatrix} m = 1,3,5,\dots; \bar{B} \text{ positive} \\ n = 2,4,6,\dots; \bar{B} \text{ negative} \end{pmatrix} \quad (\text{C15k})$$

$$C_{\text{PNAS}}(m,n) = C_{mn}^{(5)} \quad \begin{pmatrix} m = 2,4,6,\dots; \bar{B} \text{ positive} \\ n = 1,3,5,\dots; \bar{B} \text{ negative} \end{pmatrix} \quad (\text{C15l})$$

The code used to identify the integrals in equations (C13) and (C15) may be explained by considering an example. The integral $C_{\text{PNSA}}(m,n)$ is the product of the m th symmetric (S) mode shape with \bar{B} positive (P) times the first derivative with respect to ξ of the n th asymmetric (A) mode shape with \bar{B} negative (N).

The integrals for equations (C15) are

$$D_{\text{NS}}(m) = S_{\text{R2}}(\alpha_m) - G(\alpha_m, \beta_m) R_3(\alpha_m, \beta_m) + S_{\text{R5}}(\beta_m) G^2(\alpha_m, \beta_m) \quad (\text{C16a})$$

$$D_{\text{NA}}(m) = S_{\text{R1}}(\alpha_m) - H(\alpha_m, \beta_m) R_4(\alpha_m, \beta_m) + S_{\text{R6}}(\beta_m) H^2(\alpha_m, \beta_m) \quad (\text{C16b})$$

$$C_{\text{NSA}}(m,n) = A_{\text{L2}}(\alpha_m, \alpha_n) - G(\alpha_m, \beta_m) A_{\text{L4}}(\alpha_n, \beta_m) \\ - F(\alpha_n, \beta_n) B_{\text{A4}}(\alpha_m, \beta_n) + F(\alpha_n, \beta_n) G(\alpha_m, \beta_m) B_{\text{A2}}(\beta_m, \beta_n) \quad (\text{C16c})$$

APPENDIX C

$$C_{NAS}^{(m,n)} = -A_{L1}(\alpha_m, \alpha_n) + H(\alpha_m, \beta_m) A_{L3}(\alpha_n, \beta_m) + E(\alpha_n, \beta_n) B_{A3}(\alpha_m, \beta_n) - E(\alpha_n, \beta_n) H(\alpha_m, \beta_m) B_{A1}(\beta_m, \beta_n) \quad (C16d)$$

$$C_{NPSA}^{(m,n)} = A_{L2}(\alpha_m, \alpha_n) - G(\alpha_m, \beta_m) A_{L4}(\alpha_n, \beta_m) - \frac{2 C(\alpha_n, \beta_n) B_{AA2}(\alpha_m, \beta_n)}{B_{BB}(\alpha_m, \beta_n)} + \frac{2 C(\alpha_n, \beta_n) G(\alpha_m, \beta_m) B_{AA5}(\beta_m, \beta_n)}{D_D(\beta_m, \beta_n)} \quad (C16e)$$

$$C_{NPAS}^{(m,n)} = -A_{L1}(\alpha_m, \alpha_n) + H(\alpha_m, \beta_m) A_{L3}(\alpha_n, \beta_m) - \frac{2 A_A(\alpha_n, \beta_n) B_{AA1}(\alpha_m, \beta_n)}{B_{BB}(\alpha_m, \beta_n)} + \frac{2 A_A(\alpha_n, \beta_n) H(\alpha_m, \beta_m) B_{AA6}(\beta_m, \beta_n)}{D_D(\beta_m, \beta_n)} \quad (C16f)$$

$$C_{PNSA}^{(m,n)} = A_{L2}(\alpha_m, \alpha_n) - \frac{2 B_B(\alpha_m, \beta_m) A_{LL2}(\alpha_n, \beta_m)}{A_{AA}(\alpha_n, \beta_m)} - F(\alpha_n, \beta_n) B_{A4}(\alpha_m, \beta_n) + \frac{2 F(\alpha_n, \beta_n) B_B(\alpha_m, \beta_m) B_{AA4}(\beta_m, \beta_n)}{D_D(\beta_m, \beta_n)} \quad (C16g)$$

$$C_{PNAS}^{(m,n)} = -A_{L1}(\alpha_m, \alpha_n) + \frac{2 D(\alpha_m, \beta_m) A_{LL1}(\alpha_n, \beta_m)}{A_{AA}(\alpha_n, \beta_m)} + E(\alpha_n, \beta_n) B_{A3}(\alpha_m, \beta_n) - \frac{2 E(\alpha_n, \beta_n) D(\alpha_m, \beta_m) B_{AA3}(\beta_m, \beta_n)}{D_D(\beta_m, \beta_n)} \quad (C16h)$$

The remaining integrals D_{PS} , D_{PA} , C_{PSA} , C_{PAS} may be found in equations (C9). The terms used in equations (C16) are:

$$R_3(\alpha_m, \beta_m) = \frac{\sin(\alpha_m + \beta_m)}{\alpha_m + \beta_m} + \frac{\sin(\alpha_m - \beta_m)}{\alpha_m - \beta_m} \quad (C17a)$$

APPENDIX C

$$R_4(\alpha_m, \beta_m) = \frac{\sin(\alpha_m - \beta_m)}{\alpha_m - \beta_m} - \frac{\sin(\alpha_m + \beta_m)}{\alpha_m + \beta_m} \quad (C17b)$$

$$A_{L3}(\alpha_n, \beta_m) = \alpha_n \left[\frac{\sin(\alpha_n - \beta_m)}{\alpha_n - \beta_m} - \frac{\sin(\alpha_n + \beta_m)}{\alpha_n + \beta_m} \right] \quad (C17c)$$

$$A_{L4}(\alpha_n, \beta_m) = \alpha_n \left[\frac{\sin(\alpha_n + \beta_m)}{\alpha_n + \beta_m} + \frac{\sin(\alpha_n - \beta_m)}{\alpha_n - \beta_m} \right] \quad (C17d)$$

$$B_{A1}(\beta_m, \beta_n) = \beta_n \left[\frac{\sin(\beta_n - \beta_m)}{\beta_n - \beta_m} - \frac{\sin(\beta_n + \beta_m)}{\beta_n + \beta_m} \right] \quad (C17e)$$

$$B_{A2}(\beta_m, \beta_n) = \beta_n \left[\frac{\sin(\beta_n + \beta_m)}{\beta_n + \beta_m} + \frac{\sin(\beta_n - \beta_m)}{\beta_n - \beta_m} \right] \quad (C17f)$$

$$B_{A3}(\alpha_m, \beta_n) = \beta_n \left[\frac{\sin(\beta_n - \alpha_m)}{\beta_n - \alpha_m} - \frac{\sin(\beta_n + \alpha_m)}{\beta_n + \alpha_m} \right] \quad (C17g)$$

$$B_{A4}(\alpha_m, \beta_n) = \beta_n \left[\frac{\sin(\beta_n + \alpha_m)}{\beta_n + \alpha_m} + \frac{\sin(\beta_n - \alpha_m)}{\beta_n - \alpha_m} \right] \quad (C17h)$$

$$B_{AA3}(\beta_m, \beta_n) = \beta_n (\beta_m \sin \beta_n \cosh \beta_m - \beta_n \cos \beta_n \sinh \beta_m) \quad (C17i)$$

$$B_{AA4}(\beta_m, \beta_n) = \beta_n (\beta_m \cos \beta_n \sinh \beta_m + \beta_n \sin \beta_n \cosh \beta_m) \quad (C17j)$$

$$B_{AA5}(\beta_m, \beta_n) = \beta_n (\beta_n \cos \beta_m \sinh \beta_n + \beta_m \sin \beta_m \cosh \beta_n) \quad (C17k)$$

$$B_{AA6}(\beta_m, \beta_n) = \beta_n (\beta_n \sin \beta_m \cosh \beta_n - \beta_m \cos \beta_m \sinh \beta_n) \quad (C17l)$$

APPENDIX C

$$E(\alpha_n, \beta_n) = \frac{\cos \alpha_n}{\cos \beta_n} \quad (\text{C17m})$$

$$F(\alpha_n, \beta_n) = \frac{\sin \alpha_n}{\sin \beta_n} \quad (\text{C17n})$$

$$G(\alpha_m, \beta_m) = \frac{\cos \alpha_m}{\cos \beta_m} \quad (\text{C17o})$$

$$H(\alpha_m, \beta_m) = \frac{\sin \alpha_m}{\sin \beta_m} \quad (\text{C17p})$$

$$D_D(\beta_m, \beta_n) = \beta_m^2 + \beta_n^2 \quad (\text{C17q})$$

The remaining terms A_{L1}, A_{L2}, \dots may be found in equations (C10).

The determinant (eq. (C13)) was solved by the QR algorithm. In this solution, dynamic pressure and flutter frequency are obtained directly as a function of the structural damping coefficient g .

REFERENCES

1. Sylvester, Maurice A.; and Baker, John E.: Some Experimental Studies of Panel Flutter at Mach Number 1.3. NACA TN 3914, 1957. (Supersedes NACA RM L52I16.)
2. Fung, Y. C. B.: A Summary of the Theories and Experiments on Panel Flutter. AFOSR TN 60-224, U.S. Air Force, May 1960.
3. Stocker, James E.: A Comprehensive Review of Theoretical and Experimental Panel Flutter Investigations. Rep. No. NA61H-444, North American Aviation, Inc., Sept. 15, 1961.
4. Bohon, Herman L.; and Dixon, Sidney C.: Some Recent Developments in Flutter of Flat Panels. J. Aircraft, vol. 1, no. 5, Sept.-Oct. 1964, pp. 280-288.
5. Johns, D. J.: A Survey on Panel Flutter. AGARD Adv. Rep. 1, Nov. 1965.
6. Shore, Charles P.: Effects of Structural Damping on Flutter of Stressed Panels. NASA TN D-4990, 1969.
7. Weeks, George E.; and Shideler, John L.: Effect of Edge Loadings on the Vibration of Rectangular Plates With Various Boundary Conditions. NASA TN D-2815, 1965.
8. Sechler, Ernest E.; and Dunn, Louis G.: Airplane Structural Analysis and Design. John Wiley & Sons, Inc., 1942.
9. Muhlstein, Lado, Jr.; Gaspers, Peter A., Jr.; and Riddle, Dennis W.: An Experimental Study of the Influence of the Turbulent Boundary Layer on Panel Flutter. NASA TN D-4486, 1968.
10. Dowell, E. H.; and Voss, H. M.: The Effect of a Cavity on Panel Vibration. AIAA J. (Tech. Notes Comments), vol. 1, no. 2, Feb. 1963, pp. 476-477.
11. Scanlan, Robert H.; and Rosenbaum, Robert: Introduction to the Study of Aircraft Vibration and Flutter. The Macmillan Co., 1951.
12. Ungar, Eric E.; and Scharton, Terry D.: Analysis of Vibration Distributions in Complex Structures. Shock Vib. Bull., Bull. 36, Pt. 5, U.S. Dep. Def., Jan. 1967, pp. 41-53.
13. Dixon, Sidney C.: Comparison of Panel Flutter Results From Approximate Aerodynamic Theory With Results From Exact Inviscid Theory and Experiment. NASA TN D-3649, 1966.
14. Cunningham, Herbert J.: Flutter Analysis of Flat Rectangular Panels Based on Three-Dimensional Supersonic Unsteady Potential Flow. NASA TR R-256, 1967.

15. Johns, D. J.; and Parks, P. C.: Effect of Structural Damping on Panel Flutter. Aircraft Eng., vol. XXXII, no. 380, Oct. 1960, pp. 304-308.
16. Houbolt, John Cornelius: A Study of Several Aerothermoelastic Problems of Aircraft Structures in High-Speed Flight. Prom. Nr. 2760, Swiss Fed. Inst. Technol. (Zürich), 1958.
17. Erickson, Larry L.: Supersonic Flutter of Flat Rectangular Orthotropic Panels Elastically Restrained Against Edge Rotation. NASA TN D-3500, 1966.
18. Yates, E. Carson, Jr.: Subsonic and Supersonic Flutter Analysis of a Highly Tapered Swept-Wing Planform, Including Effects of Density Variation and Finite Wing Thickness, and Comparison With Experiments. NASA TN D-4230, 1967.
19. Nelson, Herbert C.; and Cunningham, Herbert J.: Theoretical Investigation of Flutter of Two-Dimensional Flat Panels With One Surface Exposed to Supersonic Potential Flow. NACA Rep. 1280, 1956. (Supersedes NACA TN 3465.)
20. Speaker, W. V.; and Ailman, C. M.: Spectra and Space-Time Correlations of the Fluctuating Pressures at a Wall Beneath a Supersonic Turbulent Boundary Layer Perturbed by Steps and Shock Waves. NASA CR-486, 1966.

TABLE I.- PANEL PROPERTIES

[Panel, 2024-T3 aluminum; stiffener, 6061-T6 aluminum; frame, 6061-T6 aluminum]

Panel	Length*		Width*		Length Width	Panel thickness		Longitudinal stiffener thickness		Transverse frame		Panel flexural rigidity, D	
	in.	m	in.	m		in.	cm	in.	cm	in.	cm	in-lb	m-N
1	13.5	0.343	13.5	0.343	1.0	0.040	0.102	0.064	0.163	0.093	0.236	62.714	7.085
2	24.5	.622	12.5	.318	1.96	.050	.127	.080	.203	.093	.236	122.488	13.839
3	24.5	.622	10.1	.257	2.43	.050	.127	.080	.203	.093	.236	122.488	13.839
4	24.5	.622	8.5	.216	2.88	.040	.102	.080	.203	.093	.236	62.714	7.085
5	24.5	.622	6.5	.165	3.77	.032	.081	.080	.203	.093	.236	32.109	3.628
6	24.5	.622	5.8	.148	4.202	.032	.081	.070	.178	.093	.236	32.109	3.628
7	13.5	.343	13.5	.343	1.0	.050	.127	.070	.178	.093	.236	122.488	13.839
8	24.5	.622	12.5	.318	1.96	.064	.163	.080	.203	.093	.236	256.75	29.007
9	24.5	.622	8.5	.216	2.88	.050	.127	.050	.127	.093	.236	122.488	13.839
10	24.5	.622	6.5	.165	3.77	.040	.102	.050	.127	.093	.236	62.714	7.085
11	24.5	.622	8.5	.216	2.88	.040	.102	.064	.163	.093	.236	62.714	7.085
12	24.5	.622	6.5	.165	3.77	.040	.102	.064	.163	.093	.236	62.714	7.085
13	24.5	.622	8.5	.216	2.88	.040	.102	.032	.081	.093	.236	62.714	7.085

*Distance between rivet lines.

Panel	Adjusted torsional stiffness, $M_{t,\theta}$				Buckling stress, σ_{cr}					
	Longitudinal stiffener		Frame		Calculated (ref. 7)		Experiment			
	lb-in ²	kN-m ²	lb-in ²	kN-m ²	psi	kN/m ²	Leading edge		Trailing edge	
							psi	kN/m ²	psi	kN/m ²
1	0.8928×10^5	2.562	1.527×10^5	4.382	859	5 923	850	5 861	850	5 861
2	1.2997	3.730	1.735	4.979	1234	8 508	1360	9 377	1240	8 550
3	1.2997	3.730	1.735	4.979	1805	12 445	1770	12 204	1860	12 825
4	1.1544	3.313	1.527	4.382	1590	10 963	1000	6 895	900	6 206
5	.8529	2.562	1.350	3.874	1702	11 735	1800	12 411	1800	12 411
6	.8529	2.448	1.350	3.874	2101	14 486	2340	16 134	2160	14 893
7	1.0465	3.003	1.735	4.979	1315	9 067	1220	8 412	965	6 654
8	1.4663	4.208	1.959	5.622	2021	13 935	1930	13 307	1885	12 997
9	.8048	2.310	1.735	4.979	2423	16 707	2460	16 962	2267	15 631
10	.7462	2.141	1.527	4.382	2660	18 341	2780	19 168	2630	18 134
11	.8928	2.562	1.527	4.382	1580	10 894	1050	7 240	1117	7 702
12	.8928	2.562	1.527	4.382	2660	18 341	2220	15 307	2090	14 411
13	.5229	1.501	1.527	4.382	1580	10 894	1275	8 791	1275	8 791

TABLE II.- EXPERIMENTAL AND CALCULATED TORSIONAL STIFFNESS

Test specimen	Design rivet spacing		Thickness				$M_{t,\theta}$			
			Hat section		Skin		Calculated		Percent difference = 100(1 - exp/calc)	
	in.	cm	in.	cm	in.	cm	lb-in ²	kN-m ²	Design spacing	1/2 rivet spacing
1	0.75	1.905	0.064	0.163	0.032	0.081	1.0922×10^5	3.134	22	12.3
2	1.0	2.54	.090	.229	.050	.127	1.70	4.878	27.7	
3	.75	1.905	.064	.163	.032	.081	1.0922	3.134	24	
4	1.0	2.54	.050	.127	.040	.102	.975	2.798	21.1	2.7
5	1.0	2.54	.032	.081	.040	.102	.716	2.055	20	8.4
6	.75	1.905	.032	.081	.032	.081	.672	1.928	25	11.7
*7	1.0	2.54	.090	.229	.040	.102	2.027	5.817	25	15

*Strap 0.10 in. (0.254 cm) on top of hat section to simulate panel frame.

TABLE III.- VIBRATION TEST RESULTS

Mode	Structural damping coefficient	Frequency, Hz	σ/σ_{cr}	Pressure, mm Hg
Panel 1				
1	0.0296	89	0	56
1	.0225	67.5	.60	56
1	.0258	90	0	143
1	.0233	80	.27	143
1	.0474	91	0	296
2	.0225	150	0	56
2	.0283	93	.60	56
2	.0295	146	0	143
2	.0266	116	.27	143
2	.0257	146	0	296
3	.0292	192	.60	56
3	.0338	207	.27	143
3	.0328	271	0	296
Panel 2				
1	0.0300	69	0	63
1	.0320	61	.27	63
1	.038	75	0	125
1	.054	82.4	0	305
2	.028	92.5	0	25
2	.038	56	.45	25
2	.0223	93	0	63
2	.034	78	.27	63
2	.0398	93	0	125
2	.0300	94	0	305
3	.020	129	0	25
3	.036	80	.45	25
3	.022	120	0	63
3	.024	104	.27	63
3	.022	133	0	125
3	.022	134	0	305
4	.020	191	0	25
4	.0222	130	.27	25
4	.032	188	0	63
4	.036	198	0	305

TABLE III.- VIBRATION TEST RESULTS - Continued

Mode	Structural damping coefficient	Frequency, Hz	σ/σ_{cr}	Pressure, mm Hg
Panel 2				
5	0.008	263	0	25
5	.036	200	.45	25
5	.020	233	.27	63
5	.010	262	0	125
5	.012	260	0	305
Panel 3				
1	0.0121	94	0	1.0
1	.032	98	0	105
1	.032	92	.45	105
1	.0618	107	0	185
1	.044	100	.20	185
1	.056	104	0	250
2	.010	131	0	1.0
2	.02	131	0	105
2	.02	106	.45	105
2	.02	125	0	185
2	.02	118	.20	185
2	.022	128	0	250
3	.018	176	0	1.0
3	.020	176	0	105
3	.0385	165	0	250
4	.026	225	0	1.0
4	.030	225	0	105
4	.0362	166	.45	105
4	.0280	203	.20	185
4	.025	222	0	250
5	.018	310	0	1.0
5	.040	314	0	105
5	.024	272	.45	185
5	.0142	296	0	250
Panel 4				
1	0.0221	105	0	44
1	.0380	104	.55	44
1	.0227	107.5	0	116
1	.0210	108	.20	116
1	.0467	110	0	286

TABLE III.- VIBRATION TEST RESULTS - Concluded

Mode	Structural damping coefficient	Frequency, Hz	σ/σ_{cr}	Pressure, mm Hg
Panel 4				
2	0.033	135	0	44
2	.0411	128	.55	44
2	.0345	133	0	116
2	.0309	132	.20	116
2	.0322	128	0	286
3	.0166	153	0	44
3	.0332	123	.55	44
3	.0190	150	0	116
3	.0236	140	.20	116
3	.0160	150	0	286
4	.0168	194	0	44
4	.0196	138	.55	44
4	.0203	192	0	116
4	.0196	172	.20	116
4	.0320	194	0	286
5	.0223	243	0	44
5	.0495	243	0	286
Panel 5				
2	0.0456	183	0.45	103
3	.0260	195	0	9
3	.064	190	0	103
3	.040	181	.45	103
3	.062	192	0	200
3	.0358	186	.27	200
3	.0300	192	0	300
4	.03	227	0	9
4	.056	227	0	103
4	.0600	242	0	200
4	.024	200	.27	200
4	.03	232	0	300
5	.020	264	0	9
5	.036	269	0	103
5	.042	280	0	200
5	.020	228	.27	200
6	.02	314	0	9
6	.024	225	.45	103

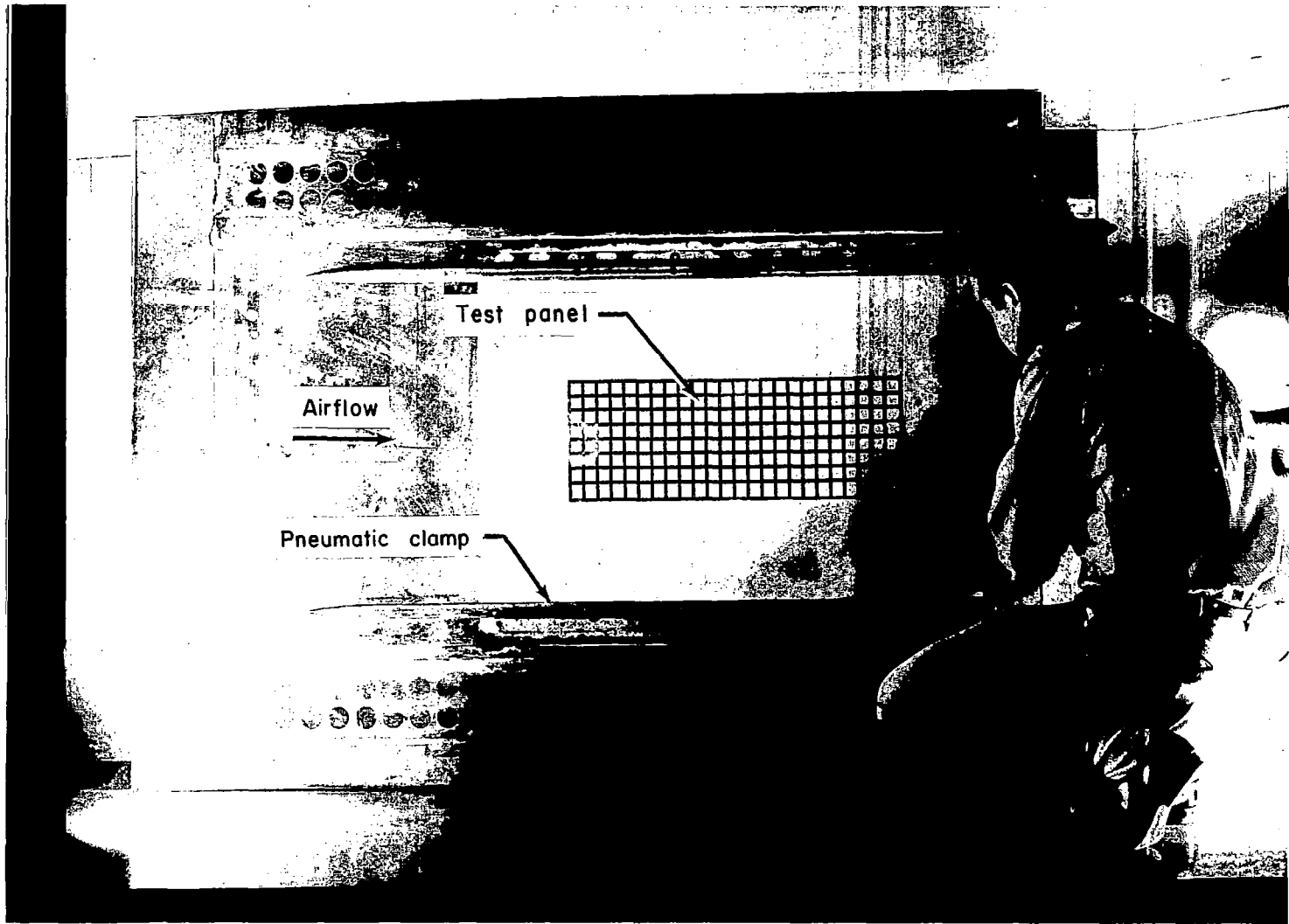


Figure 1.- Panel mounted on splitter plate.

L-65-1693.1

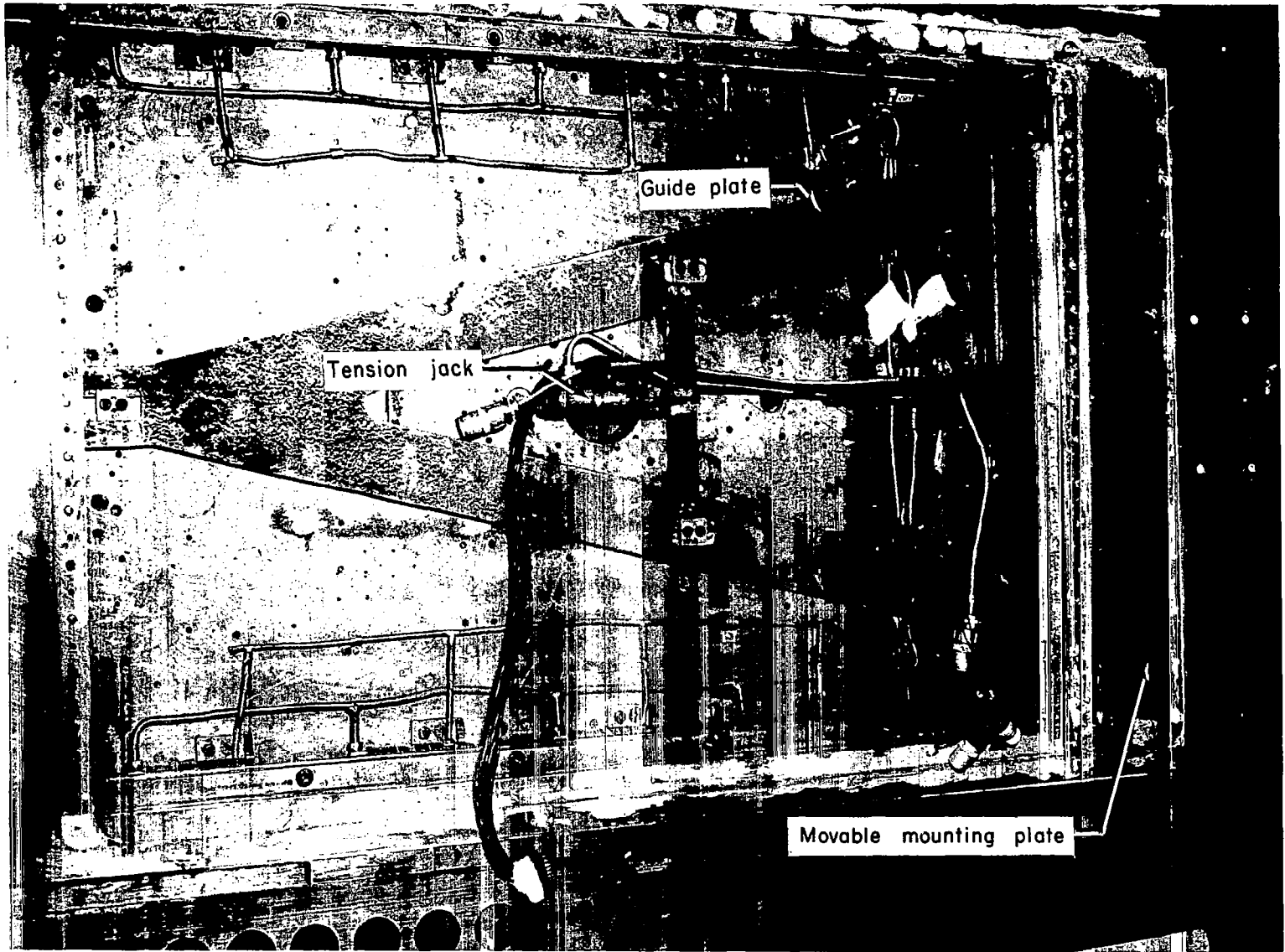


Figure 2.- Splitter plate cavity.

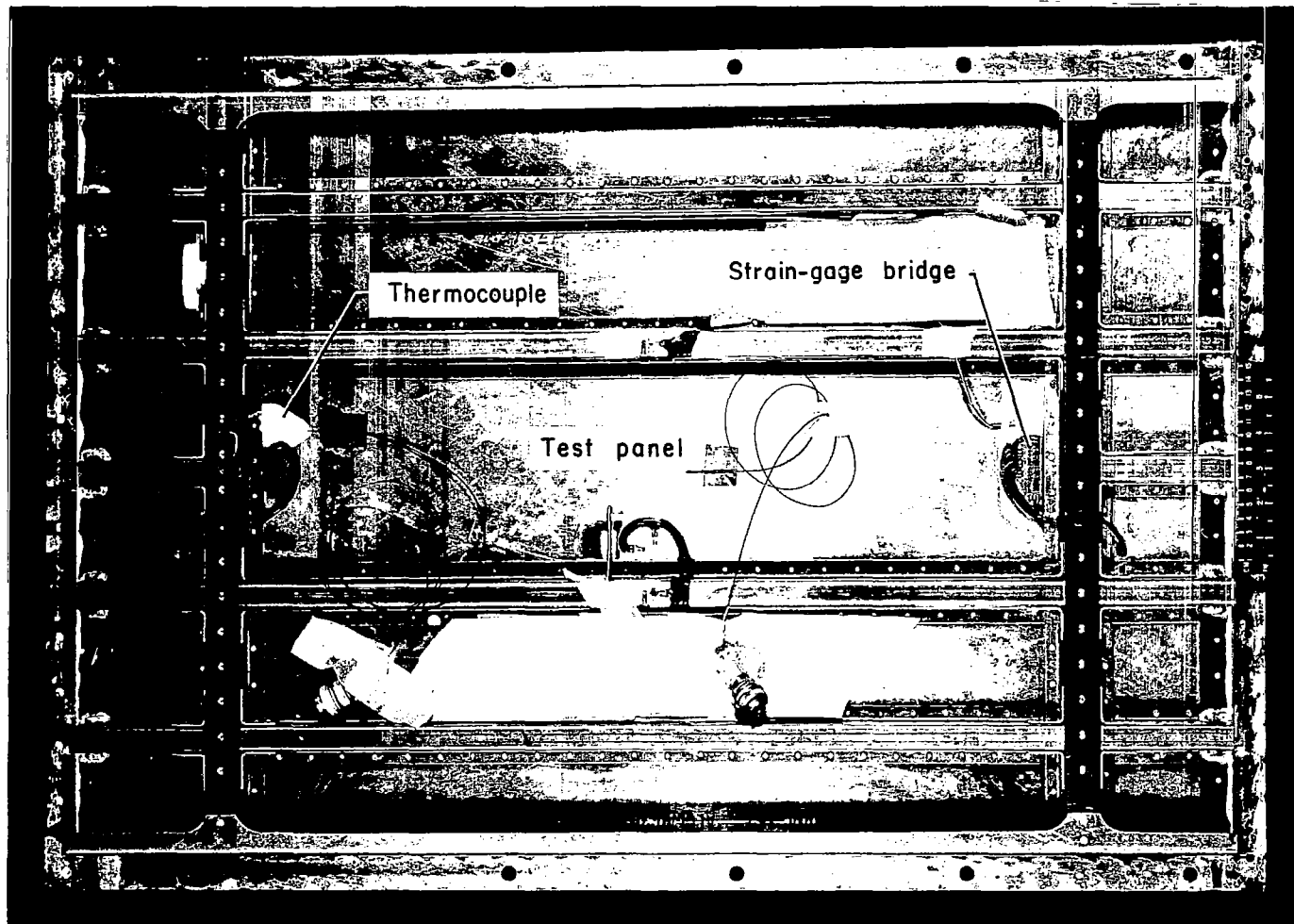


Figure 3.- Under side of panel 6.

L-65-7638.1

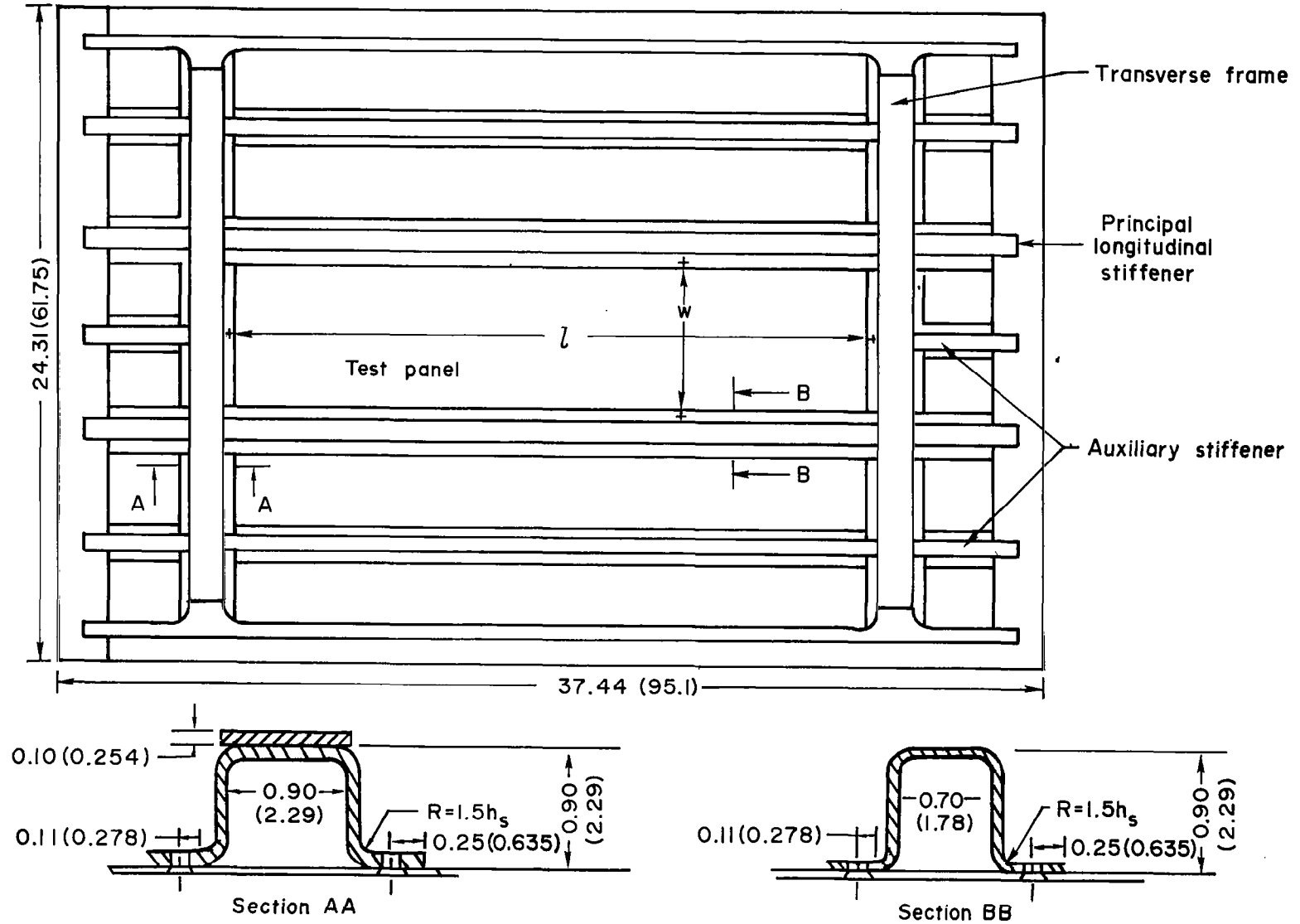


Figure 4.- Panel details. Dimensions are in inches (cm).

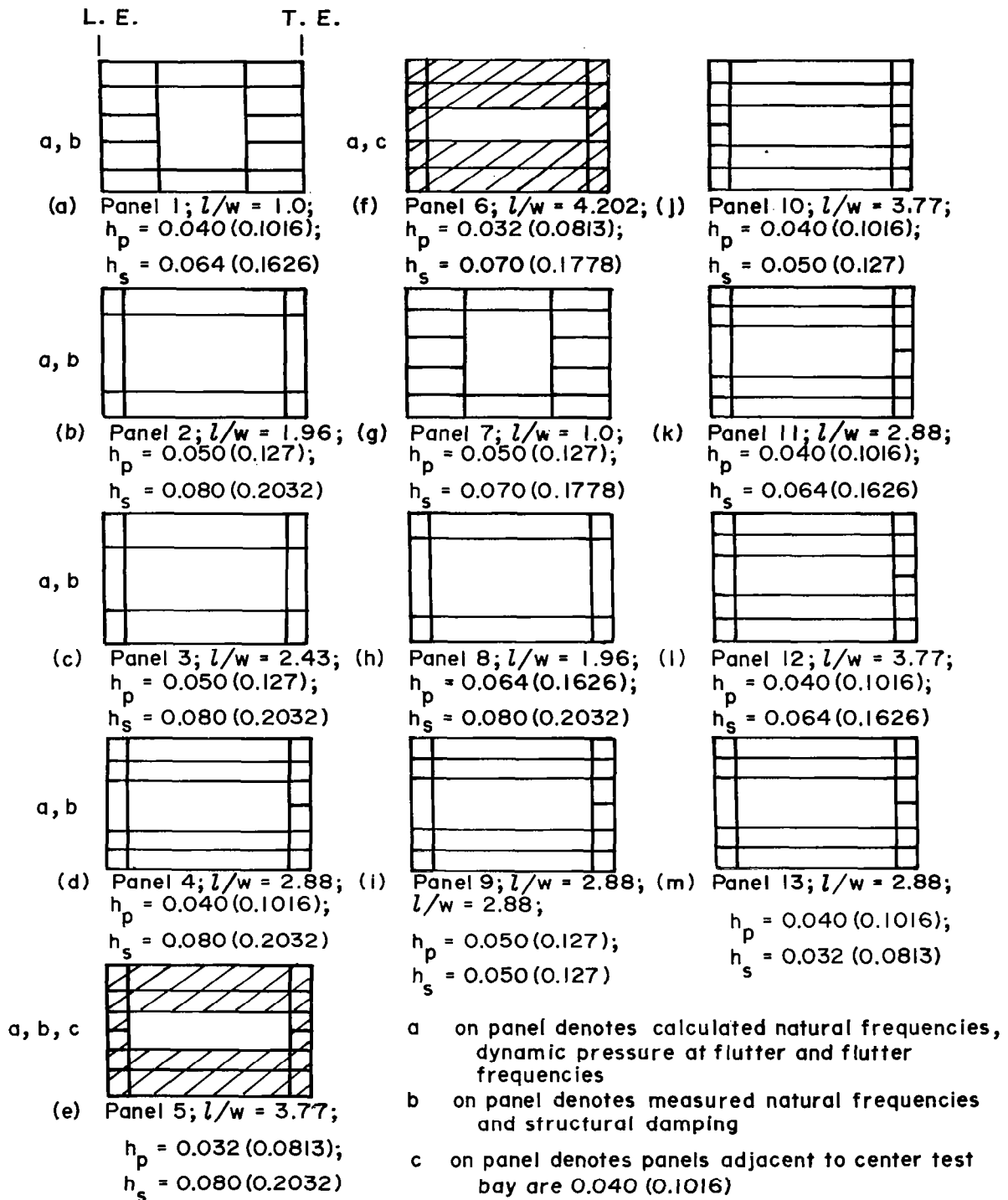
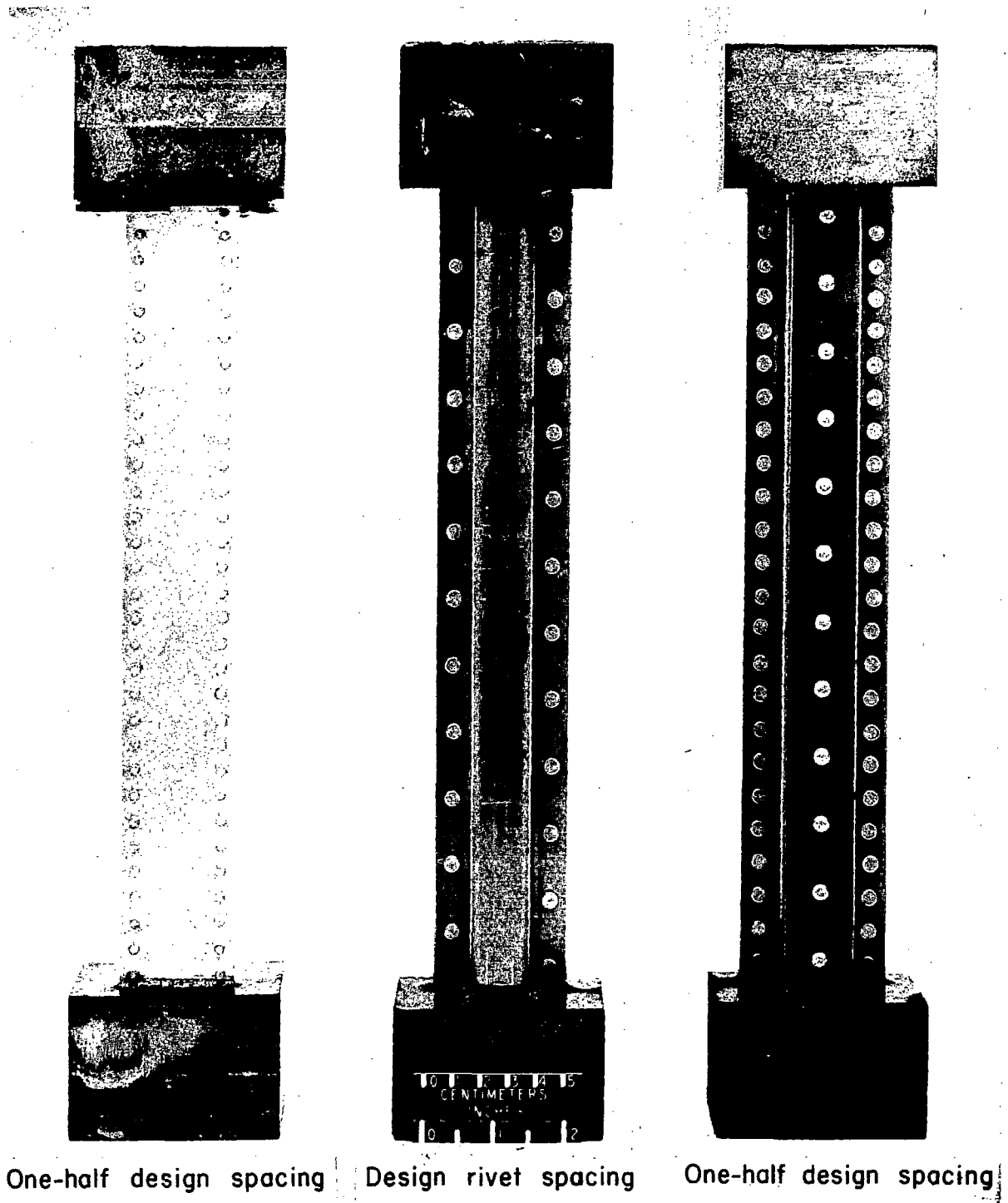


Figure 5.- Summary of panel configurations used in investigation. Thickness of flutter panel h_p and primary longitudinal stiffener h_s given in inches (cm).

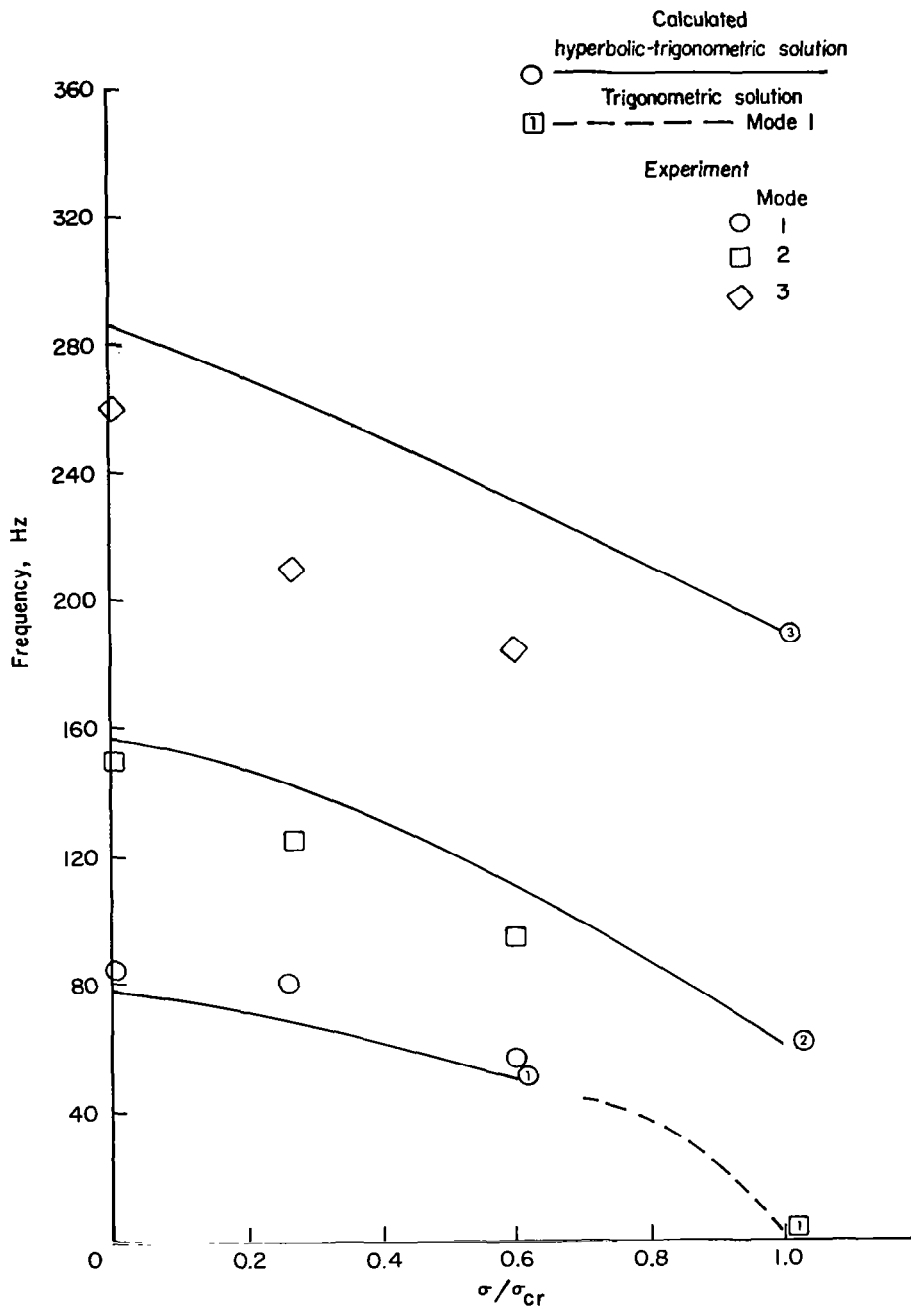


(a) Longitudinal stiffeners.

(b) Transverse frame.

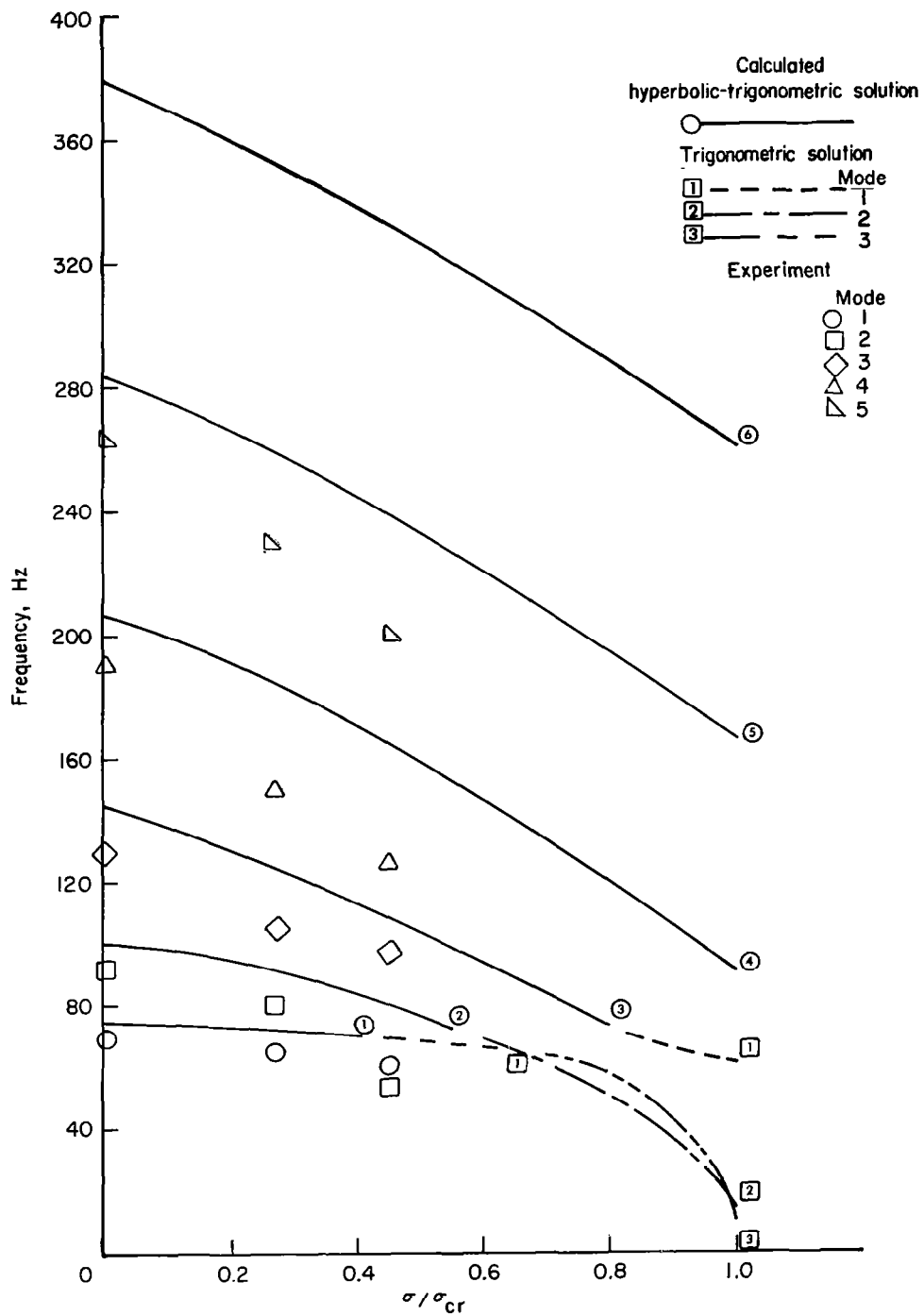
Figure 6.- Examples of torsional stiffness test specimens.

L-68-1590



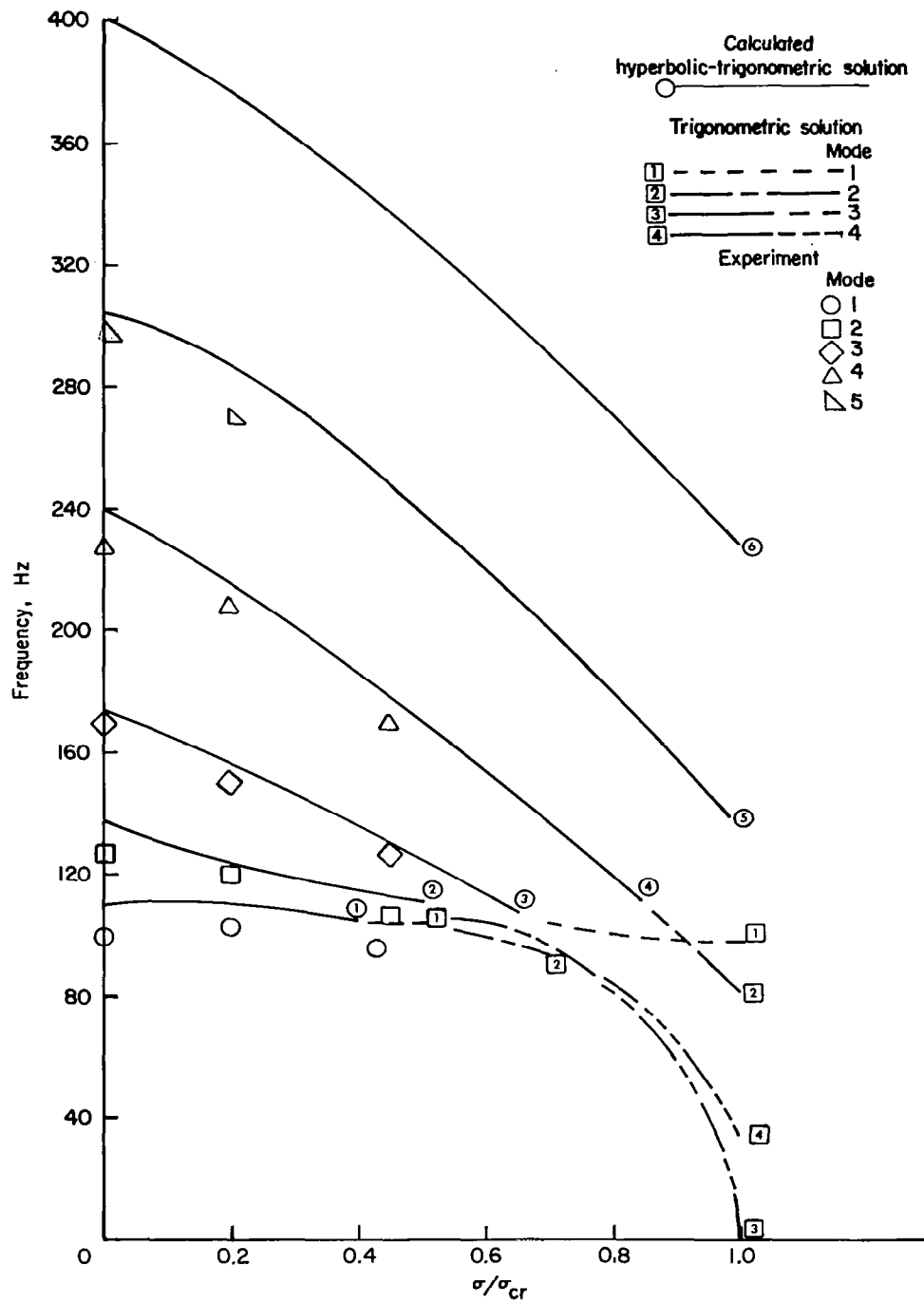
(a) Panel 1; $L/w = 1.0$.

Figure 7.- Calculated and measured natural frequencies as a function of stress ratio σ/σ_{cr} .



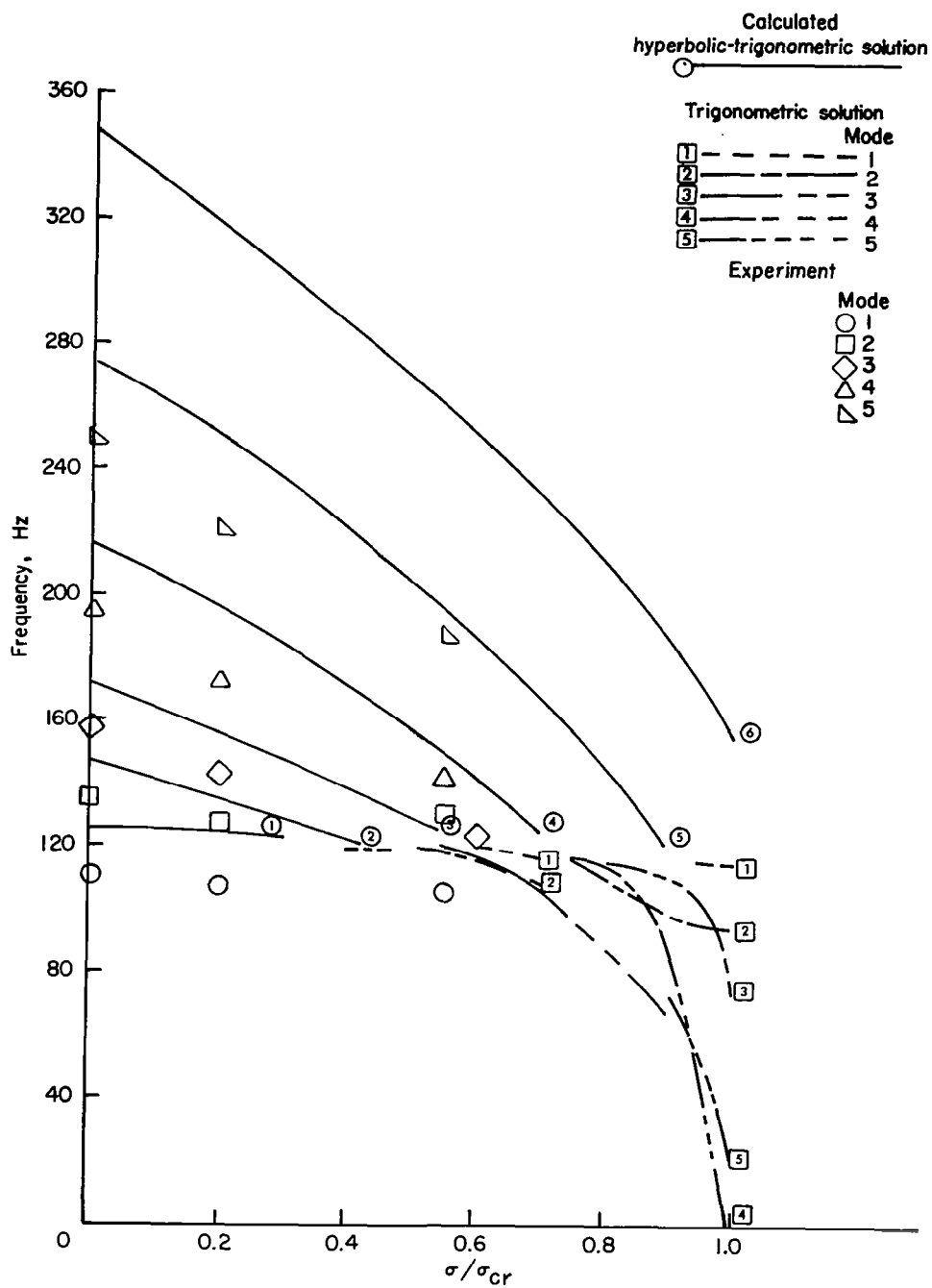
(b) Panel 2; $L/w = 1.96$.

Figure 7.- Continued.



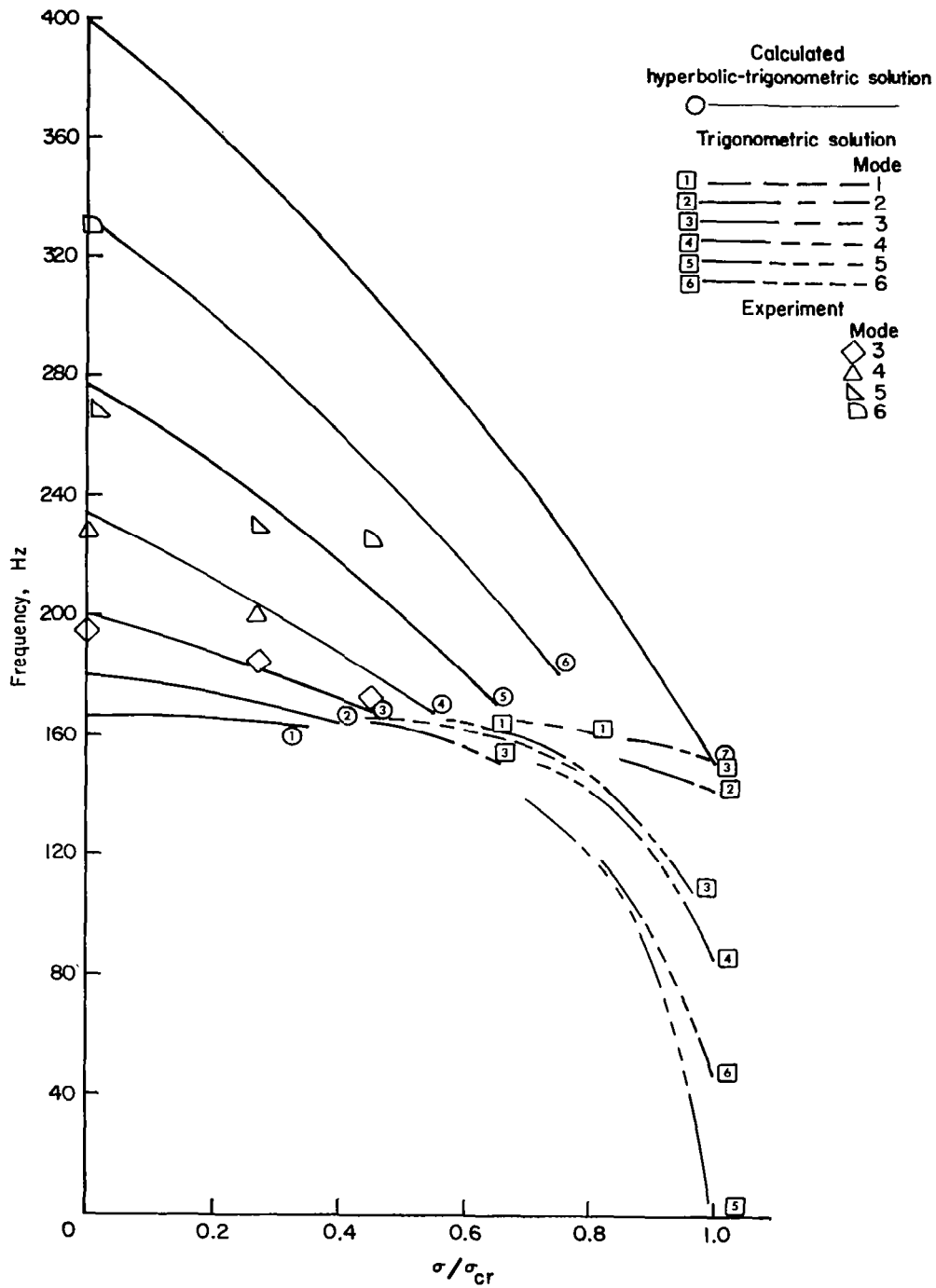
(c) Panel 3; $L/w = 2.43$.

Figure 7.- Continued.



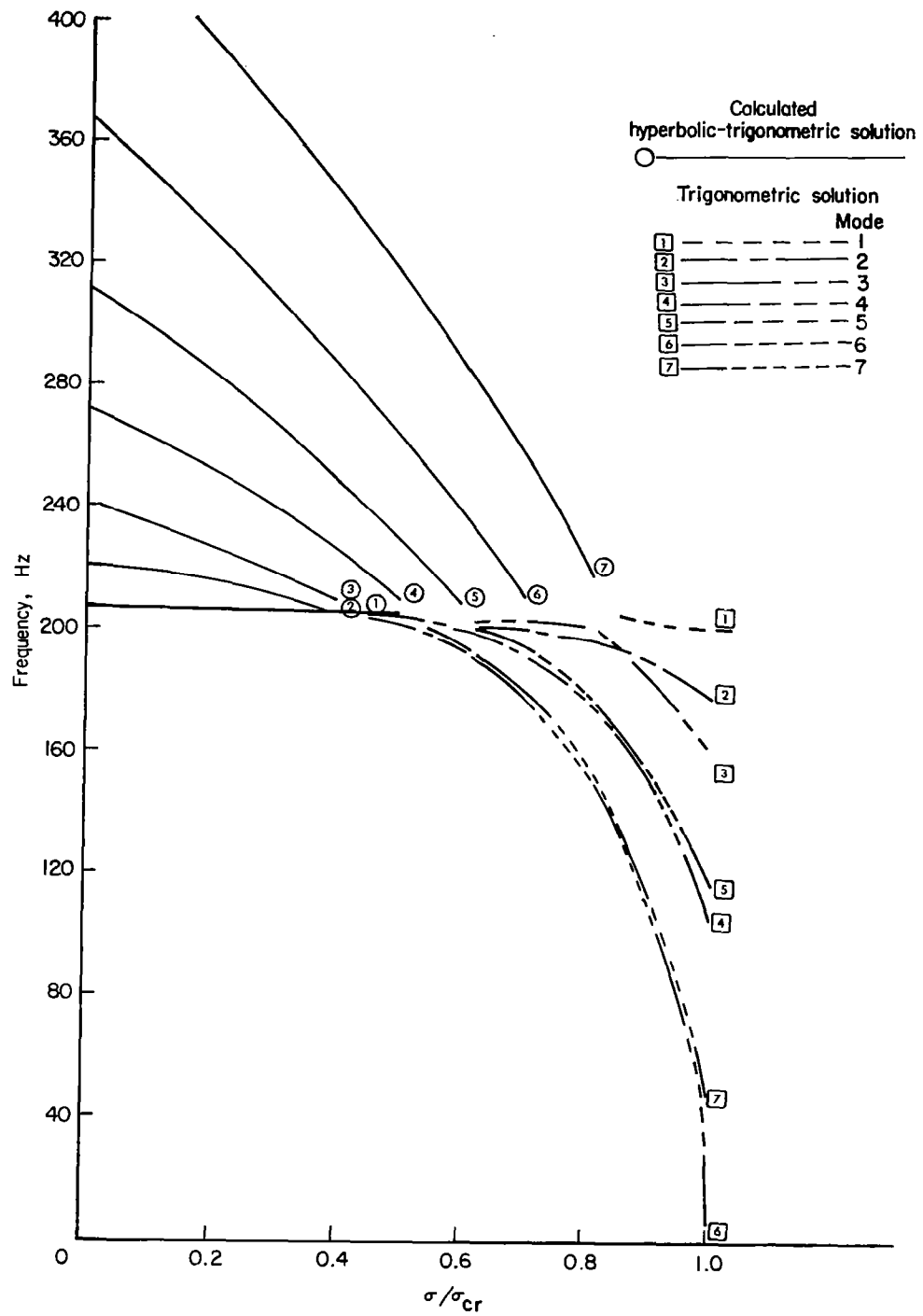
(d) Panel 4; $L/w = 2.88$.

Figure 7.- Continued.



(e) Panel 5; $L/w = 3.77$.

Figure 7.- Continued.



(f) Panel 6; $L/w = 4.202$.

Figure 7.- Concluded.

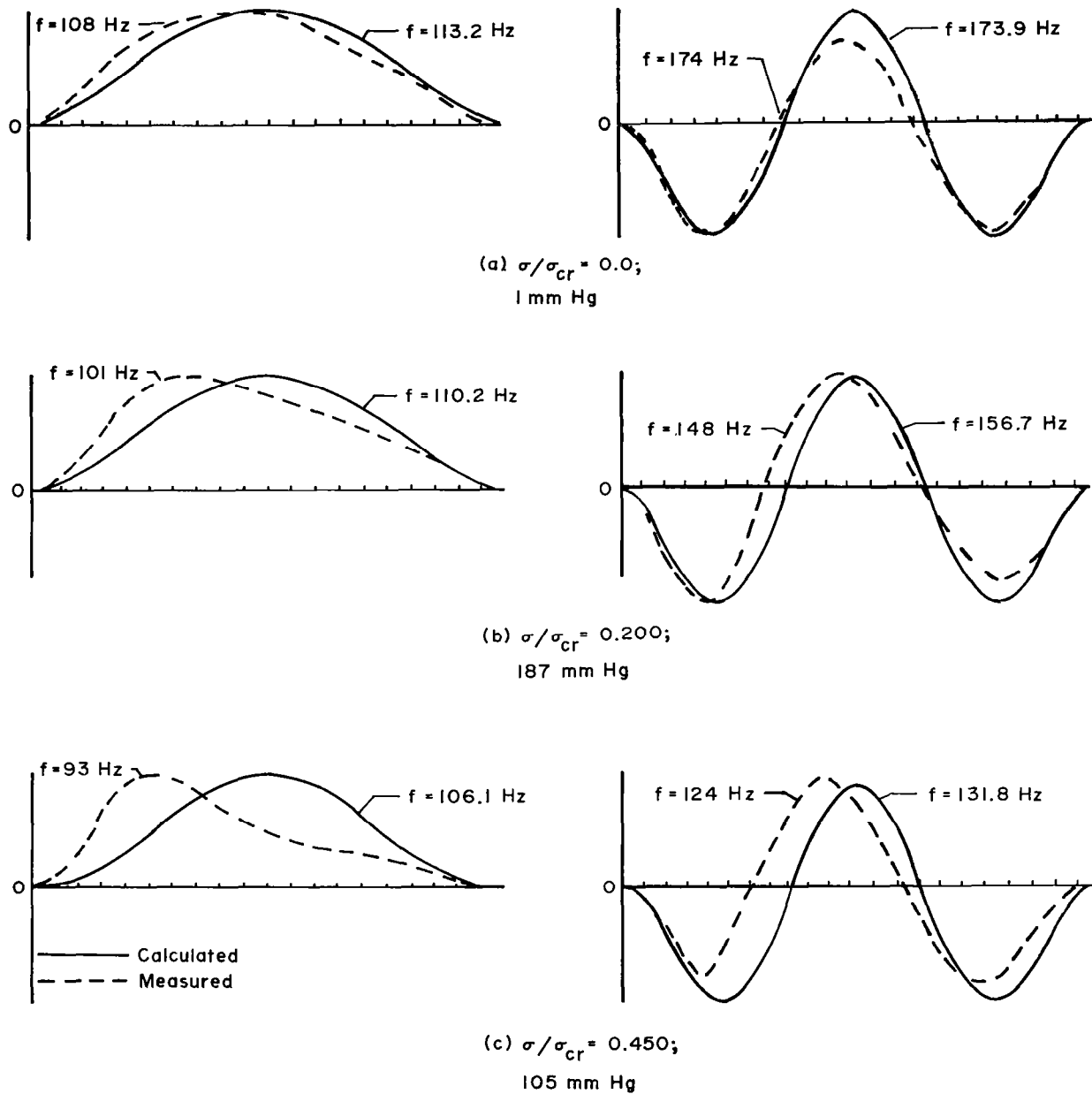
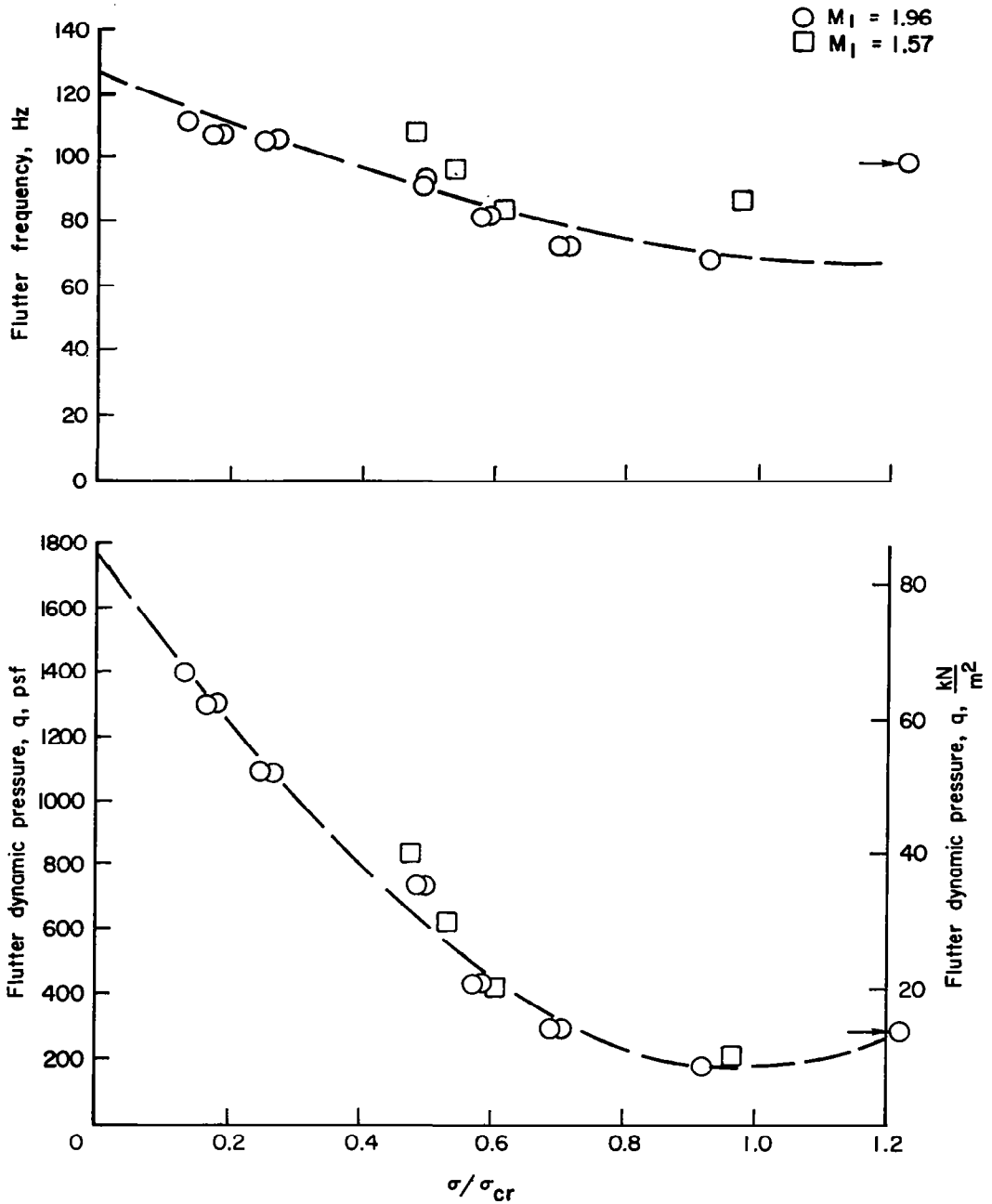
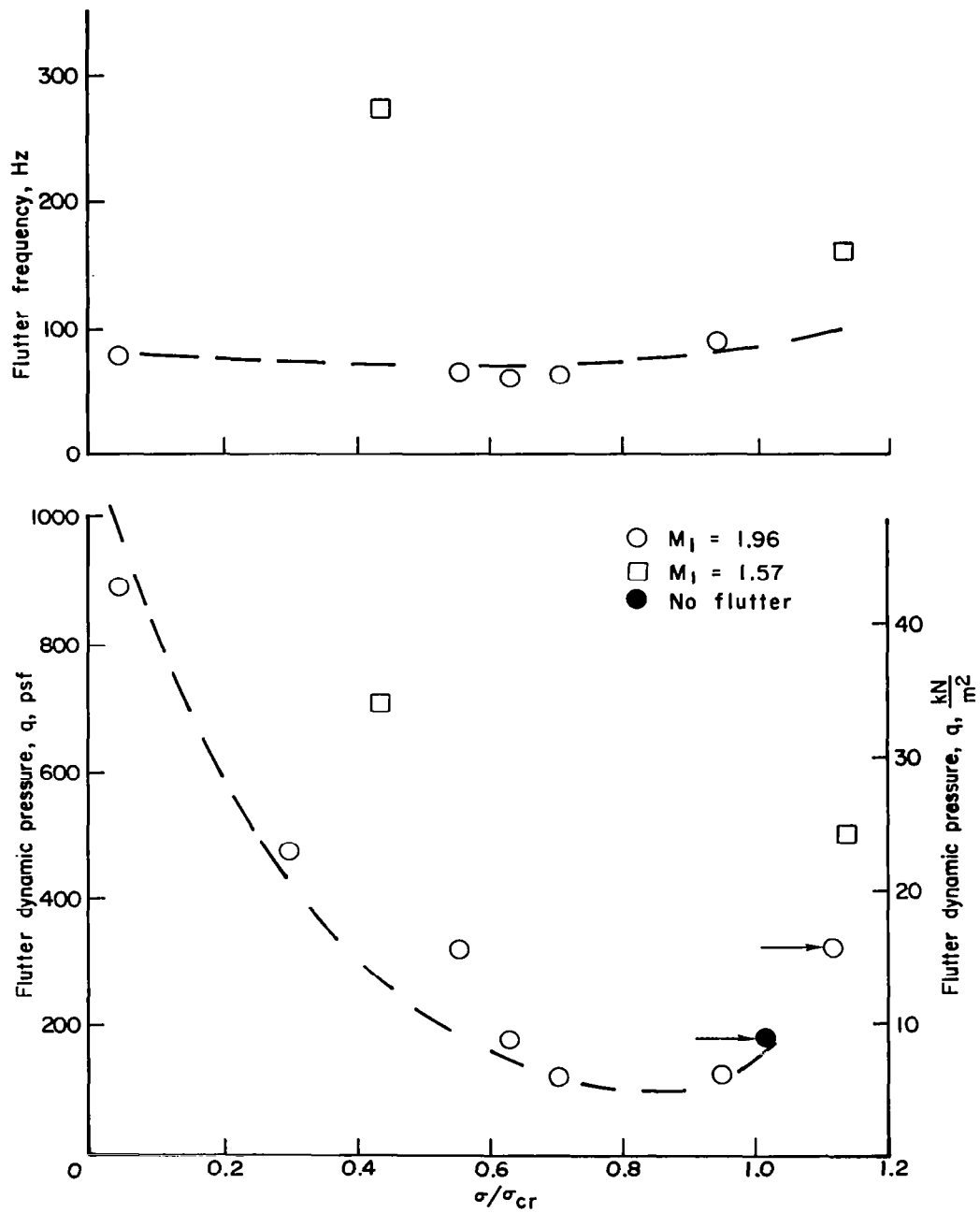


Figure 8.- First- and third-mode shapes of panel 3 after flutter tests.



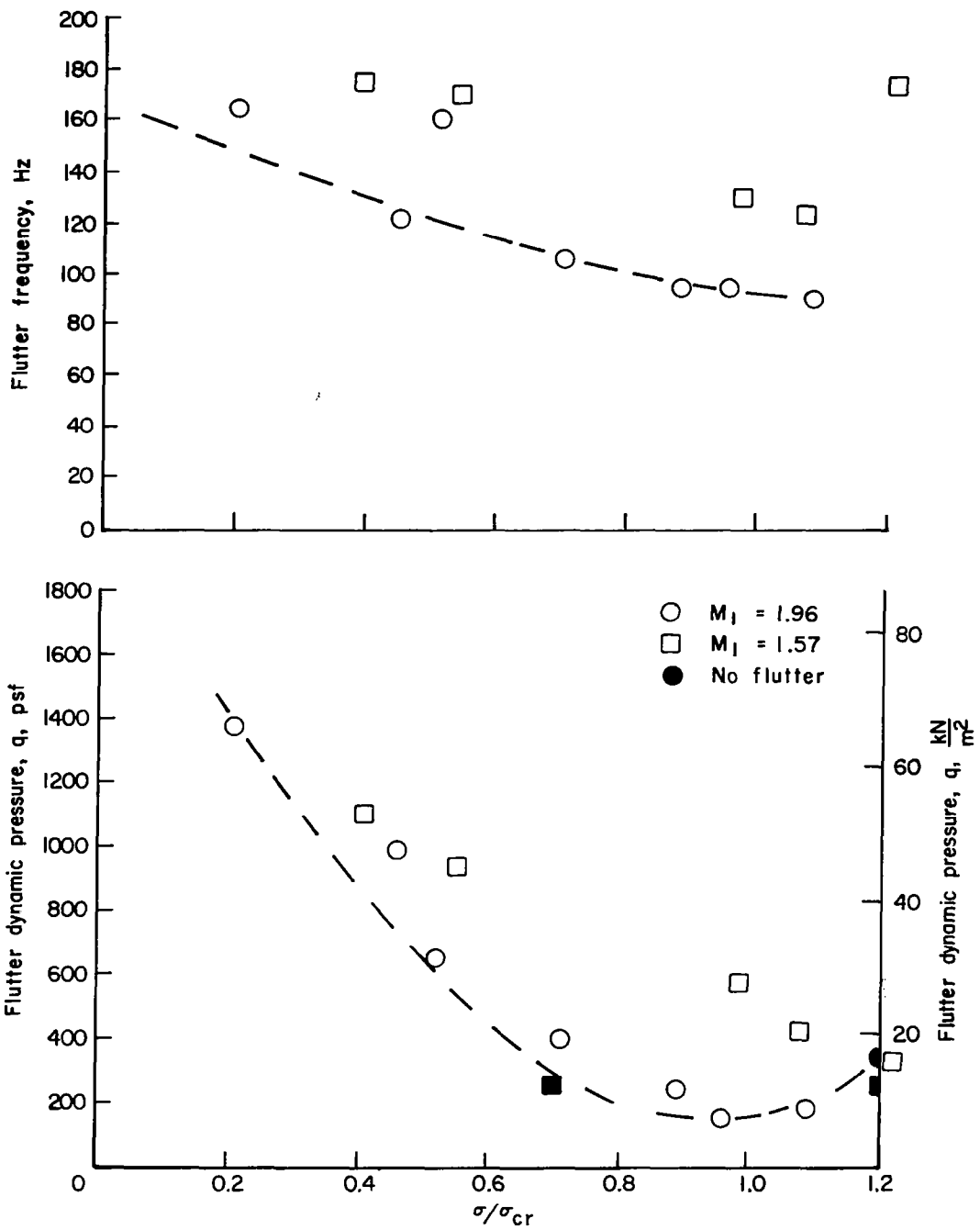
(a) Panel 1; $L/w = 1$.

Figure 9.- Experimental flutter results. Flutter frequency and dynamic pressure as a function of stress ratio σ/σ_{cr} .



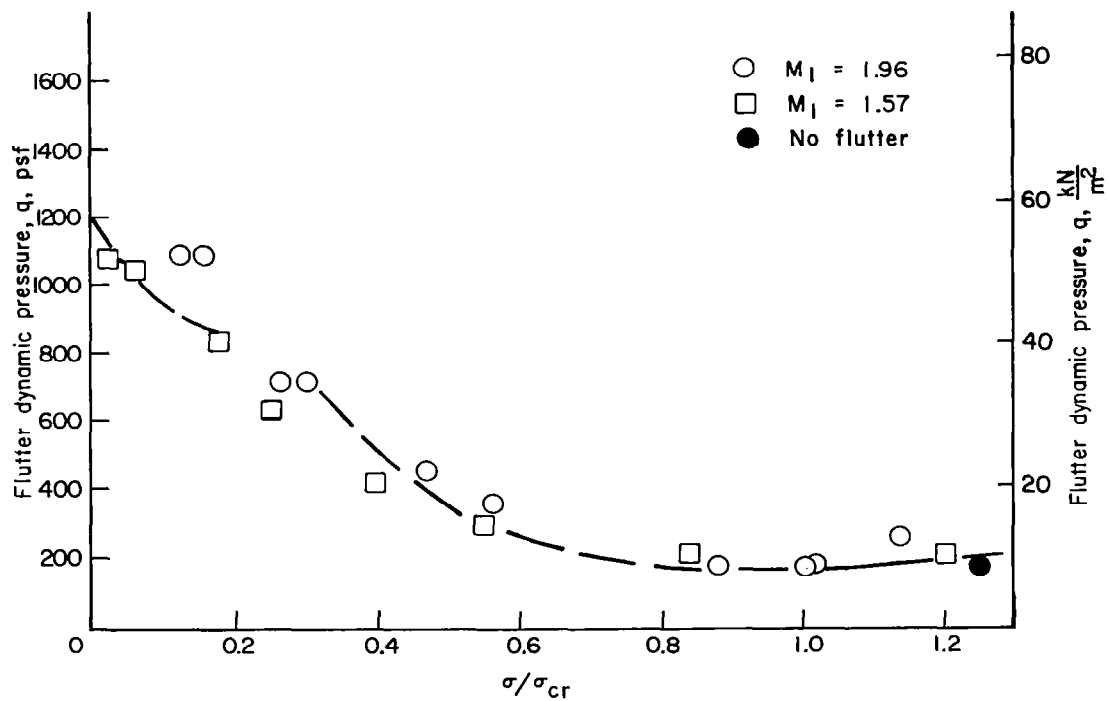
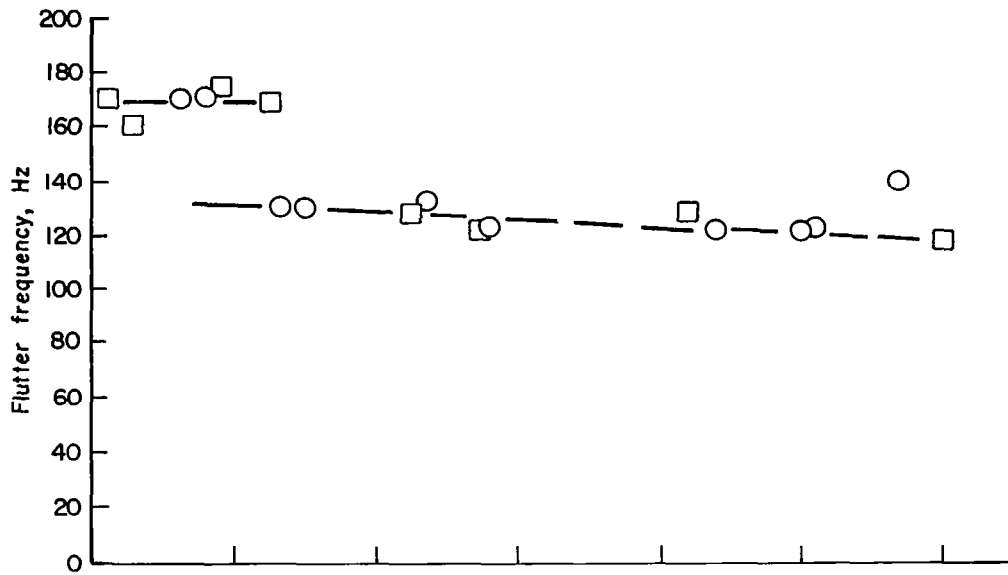
(b) Panel 2; $l/w = 1.96$.

Figure 9.- Continued.



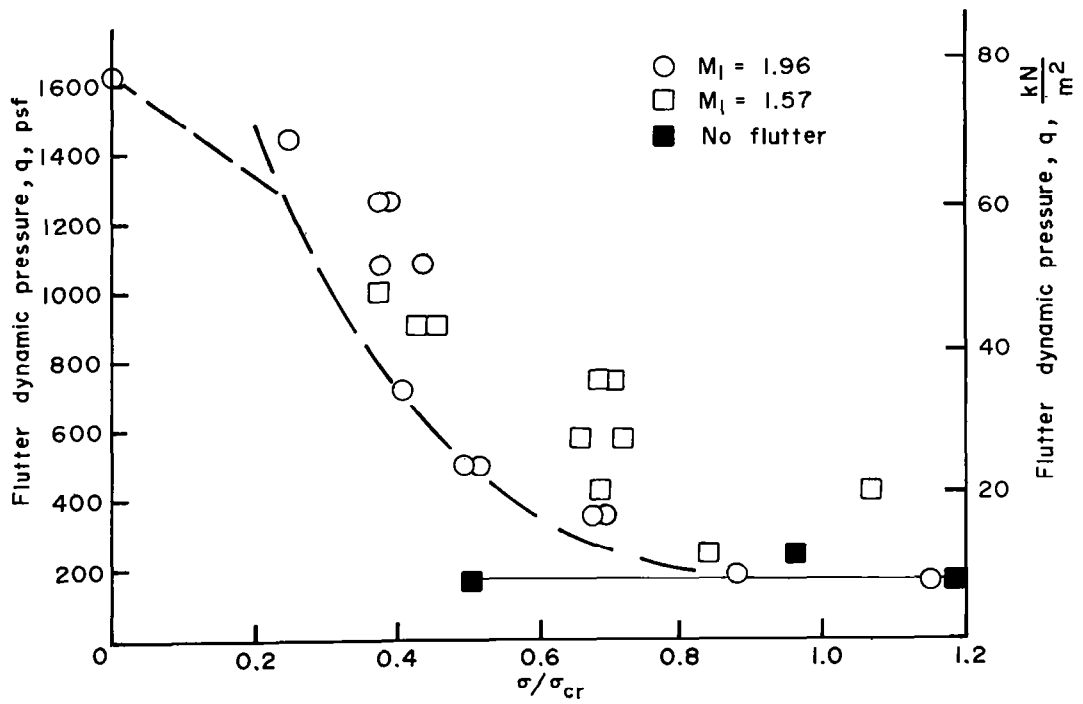
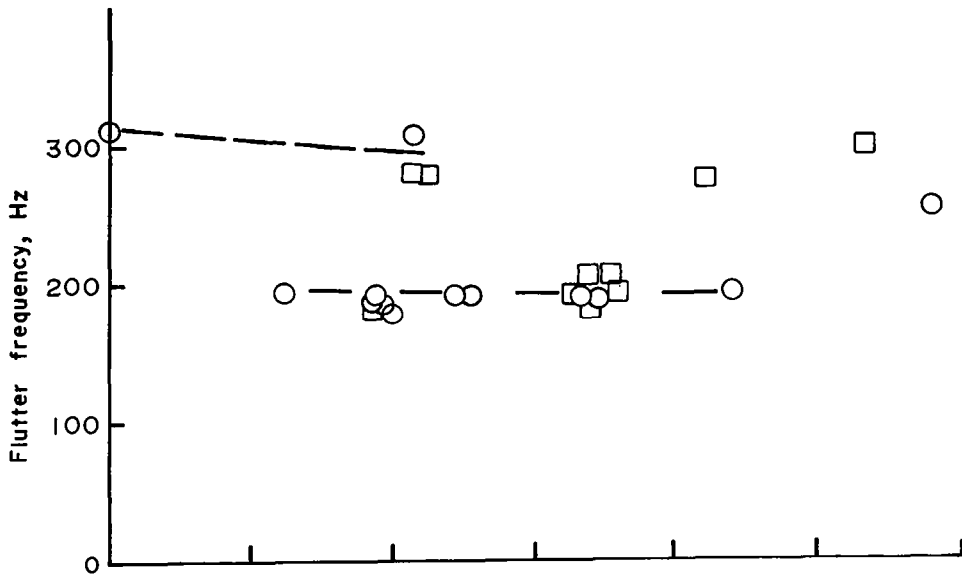
(c) Panel 3; $l/w = 2.43$.

Figure 9.- Continued.



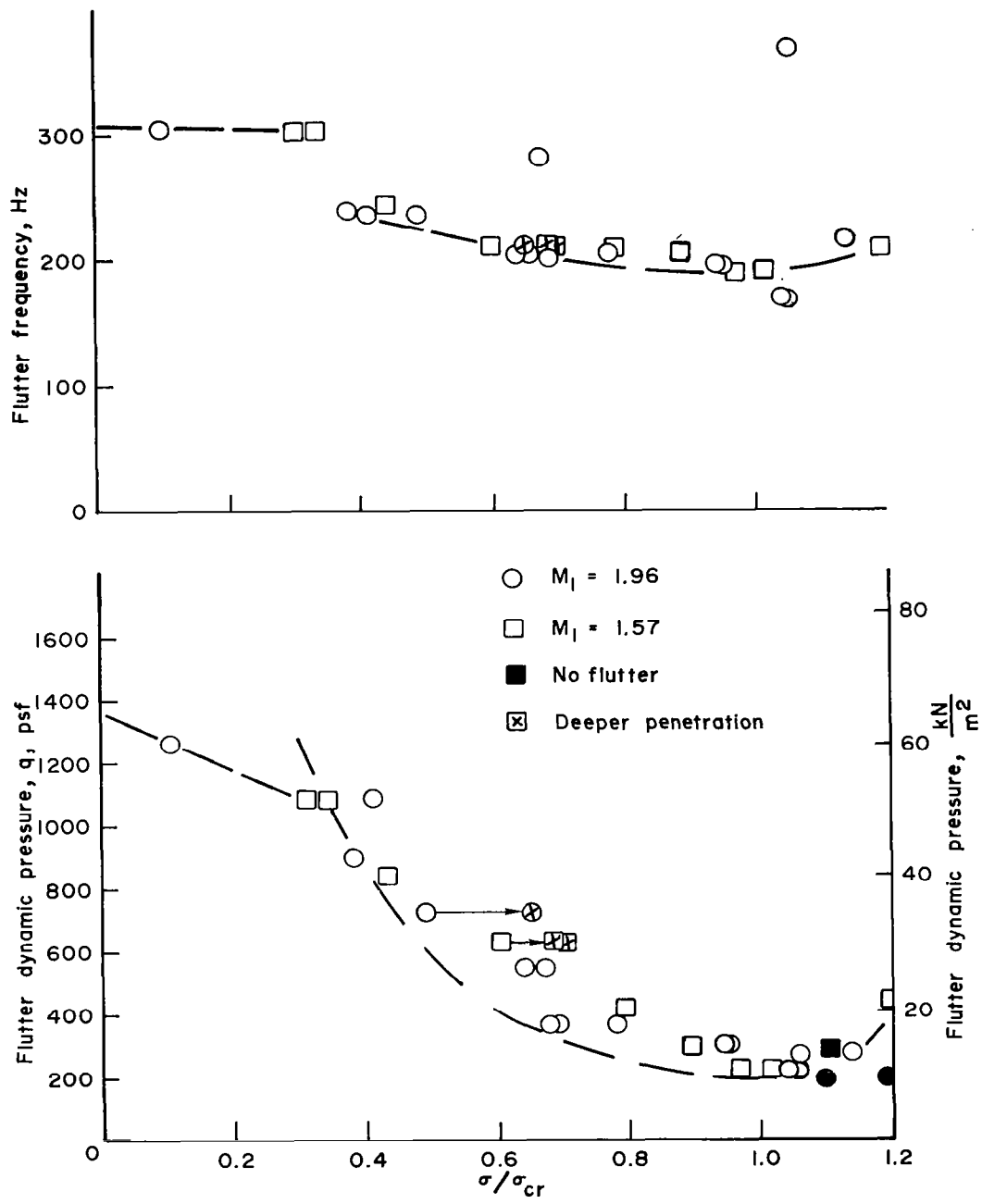
(d) Panel 4; $L/w = 2.88$.

Figure 9.- Continued.



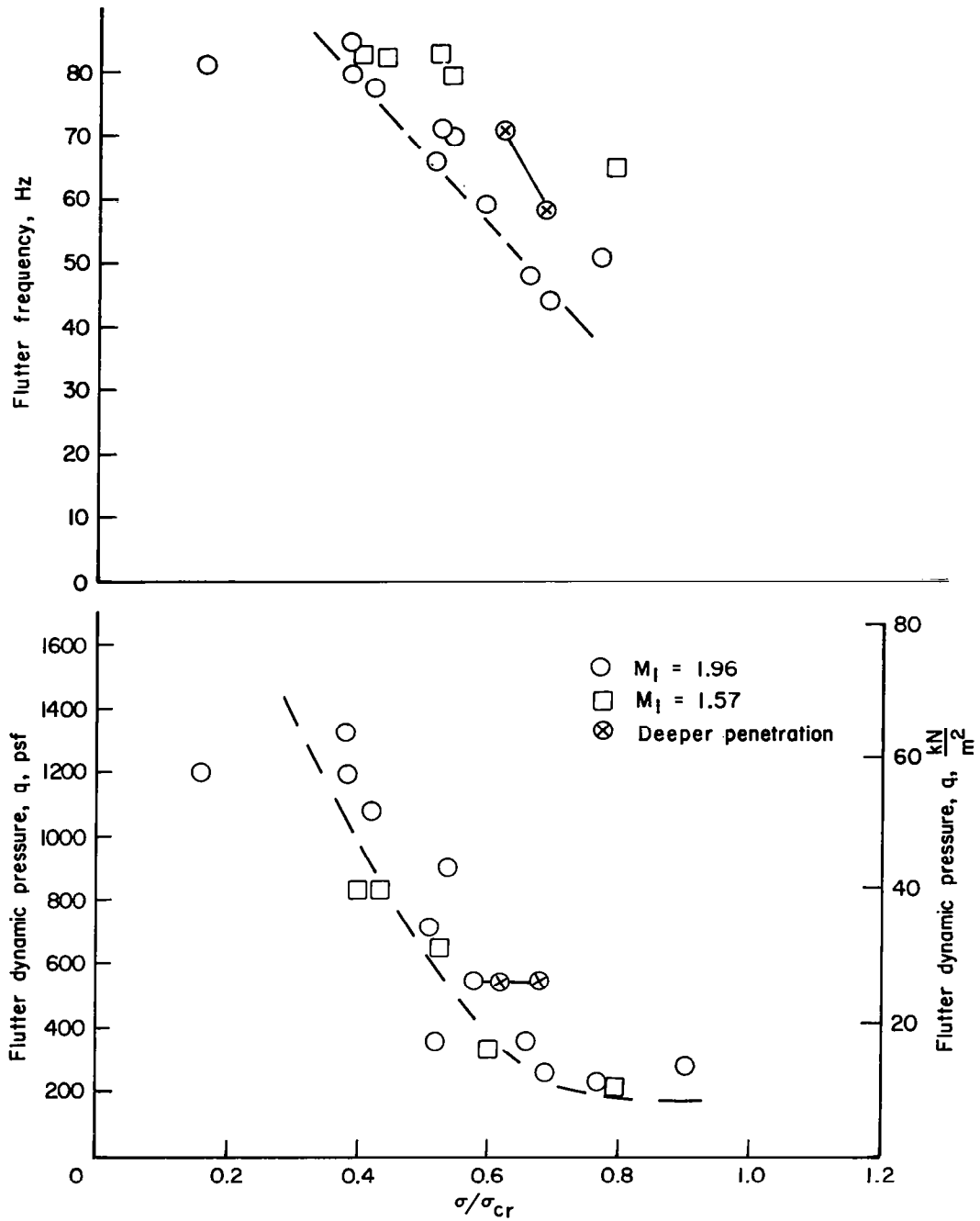
(e) Panel 5; $l/w = 3.77$.

Figure 9.- Continued.



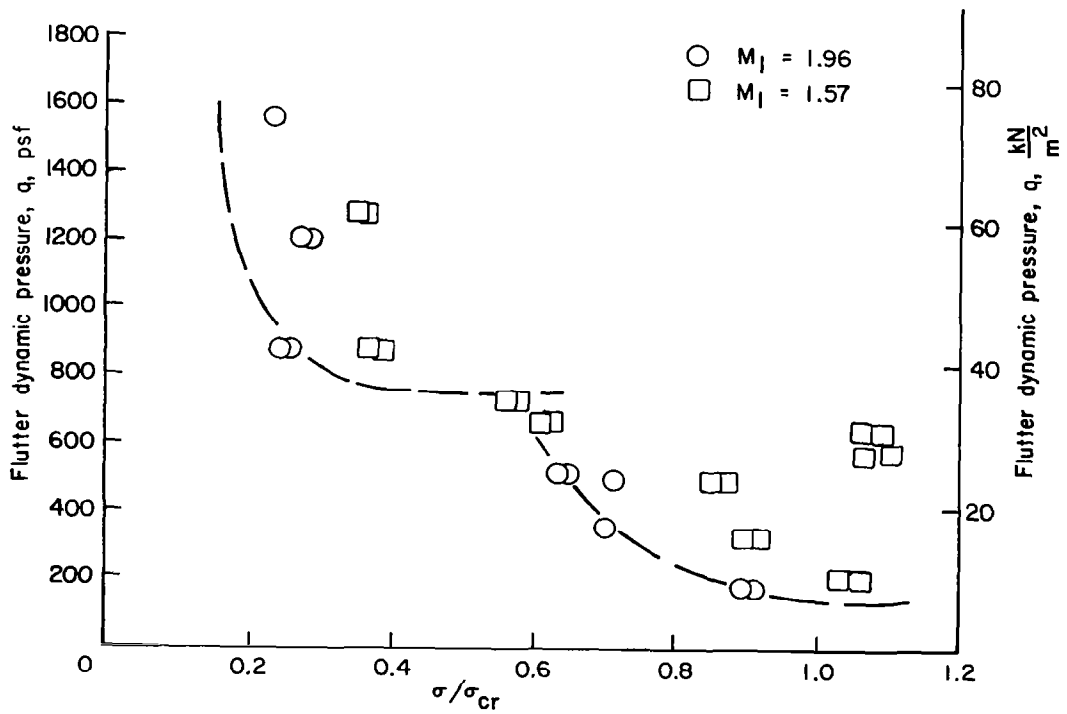
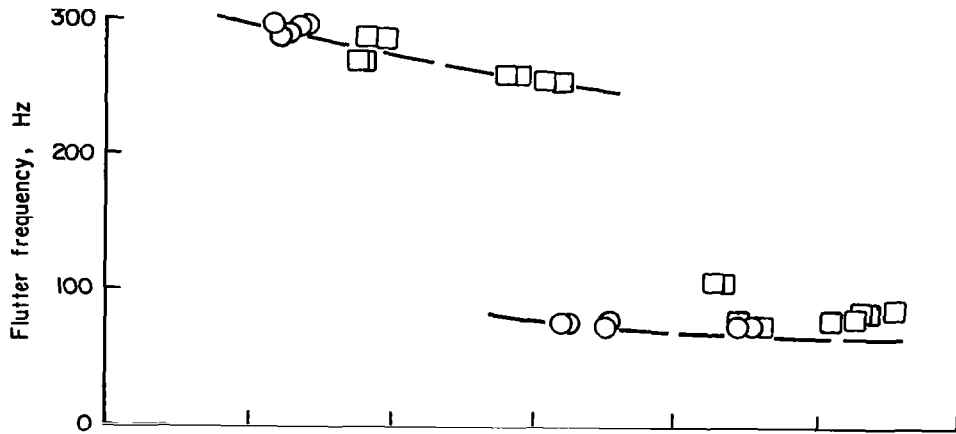
(f) Panel 6; $l/w = 4.202$.

Figure 9.- Continued.



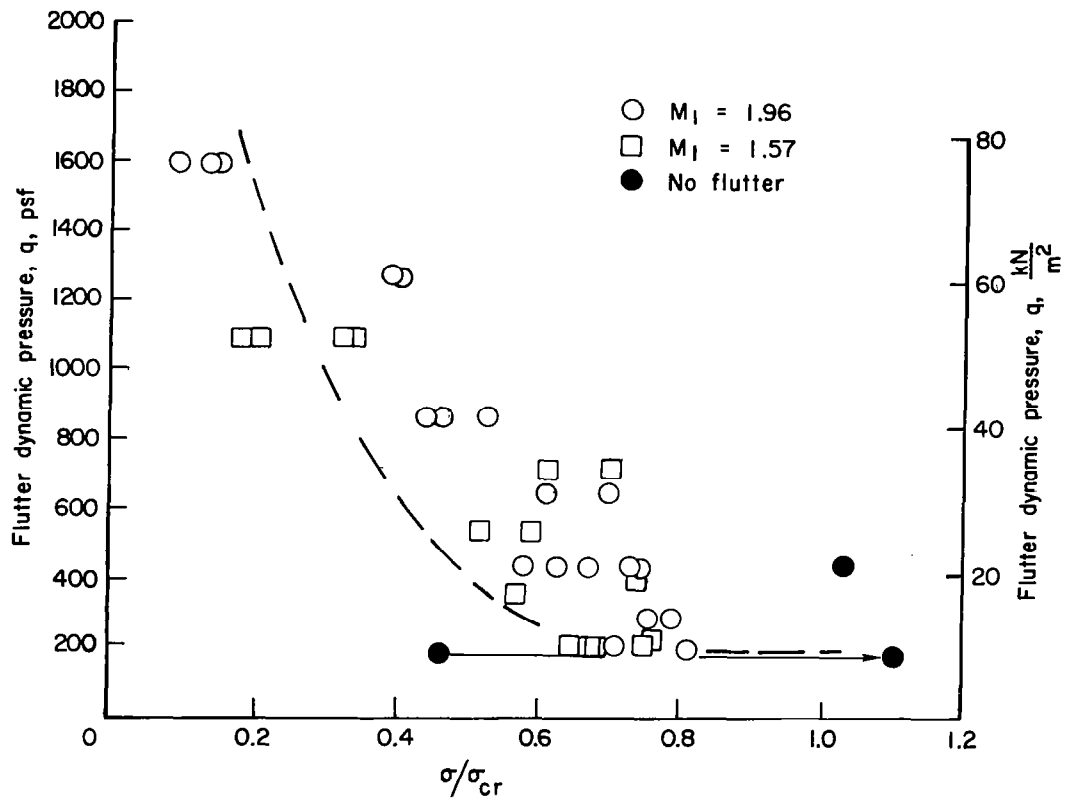
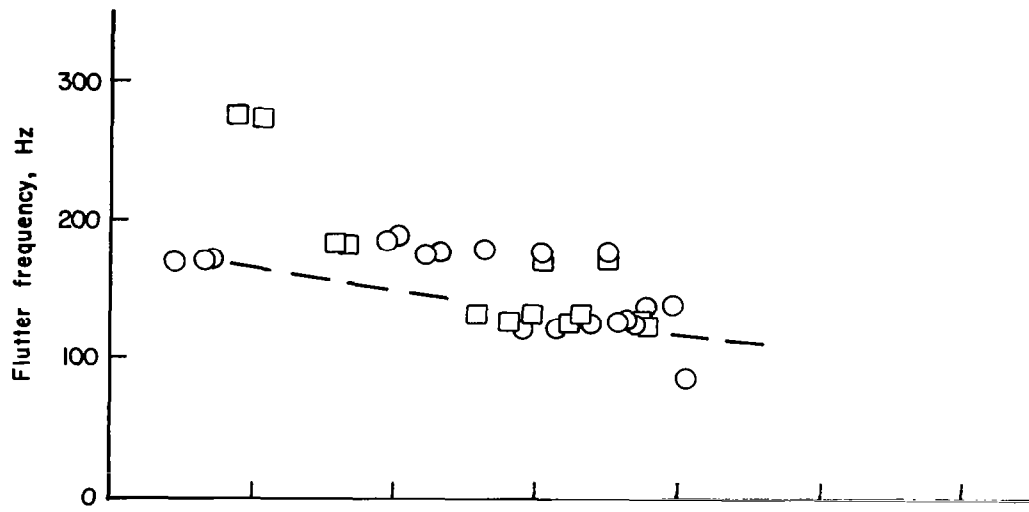
(g) Panel 7; $L/w = 1.0$.

Figure 9.- Continued.



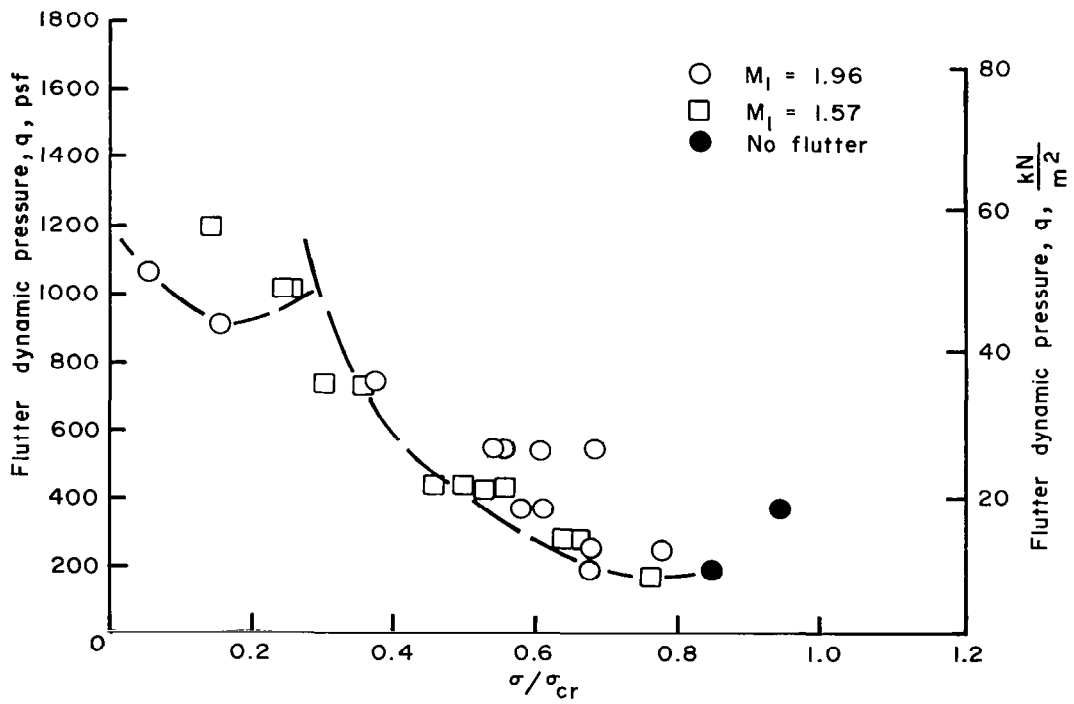
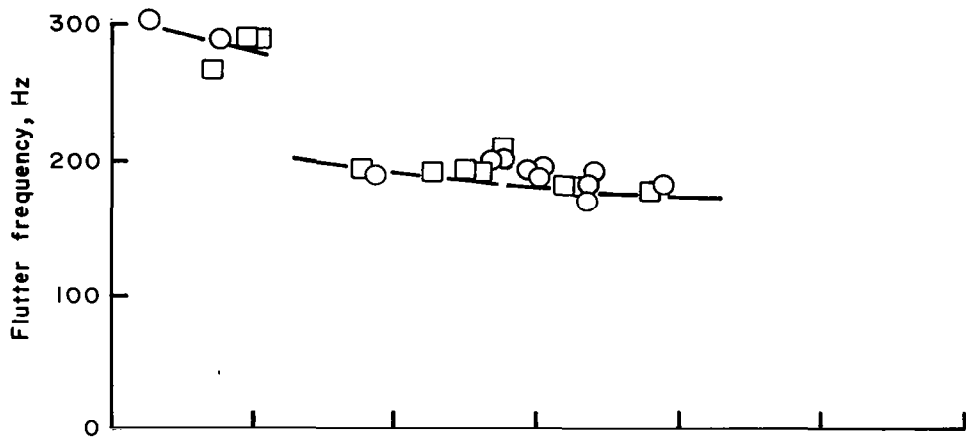
(h) Panel 8; $L/w = 1.96$.

Figure 9.- Continued.



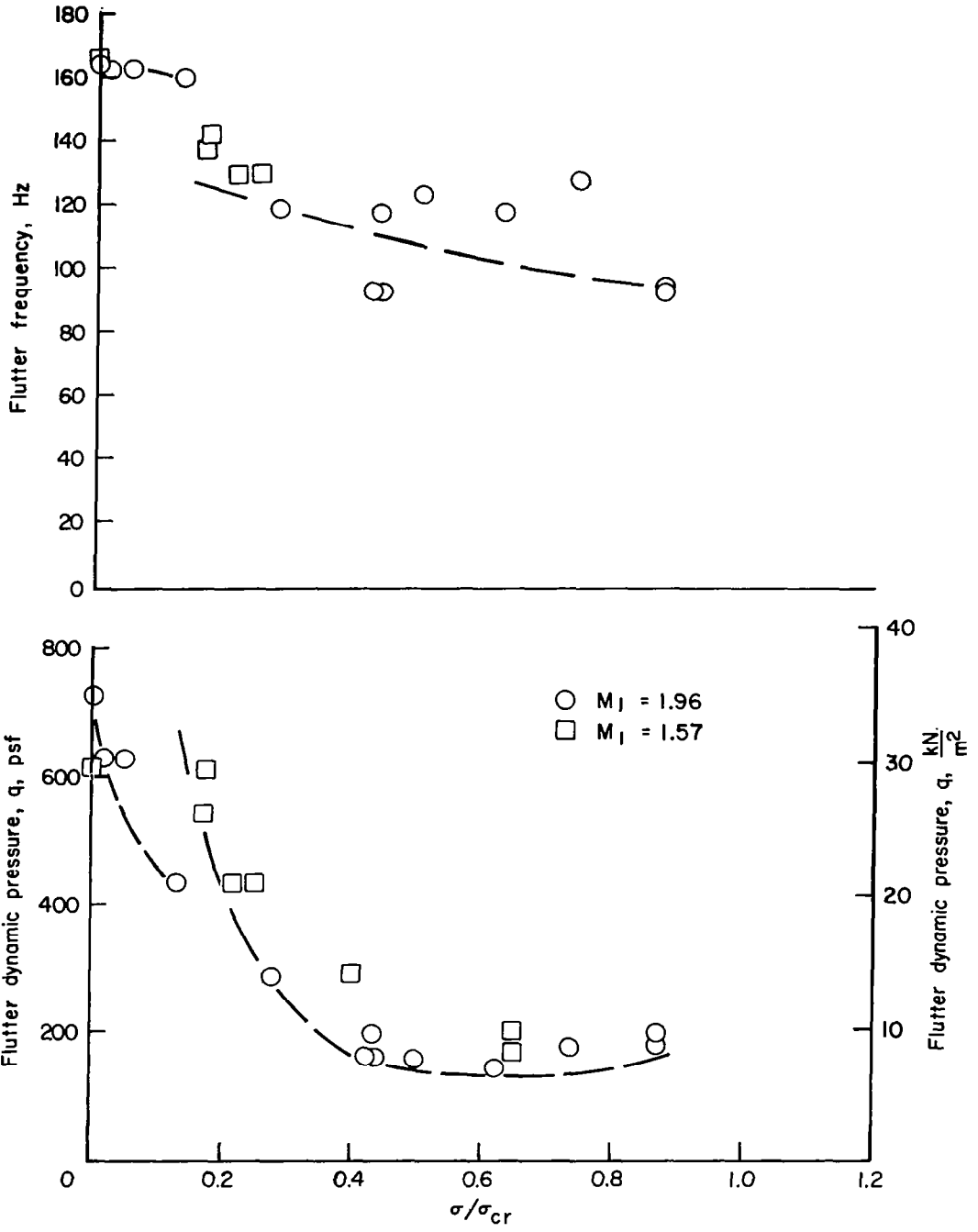
(i) Panel 9; $L/w = 2.88$.

Figure 9.- Continued.



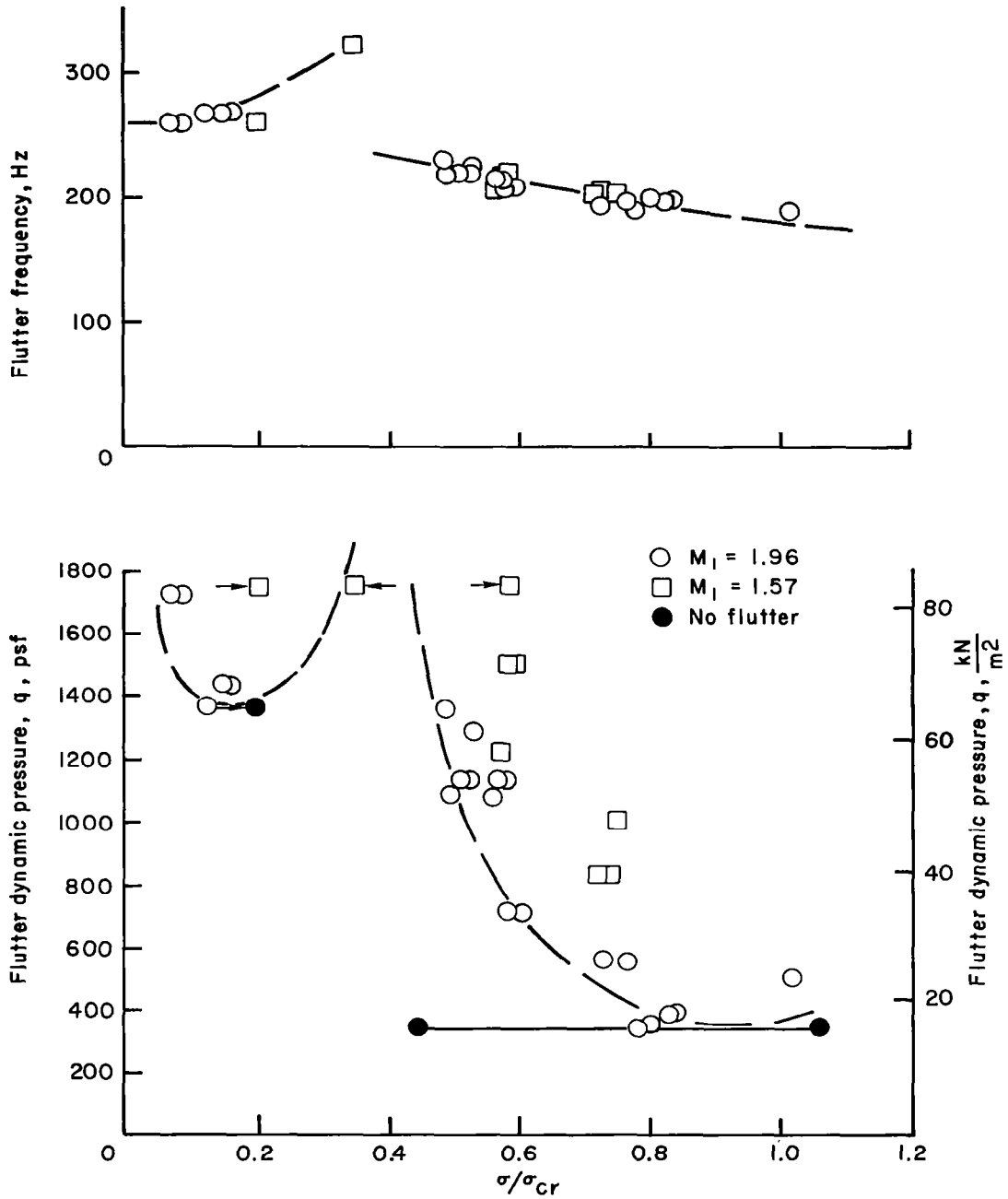
(j) Panel 10; $l/w = 3.77$.

Figure 9.- Continued.



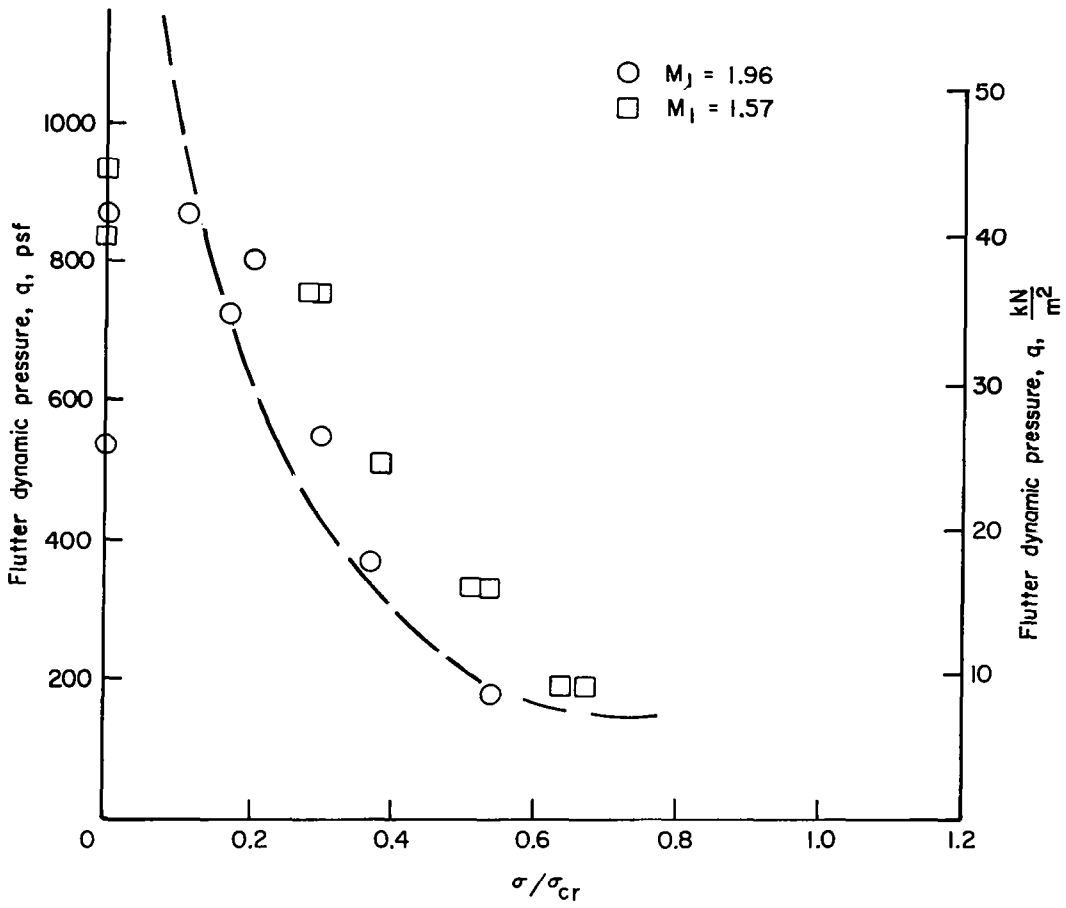
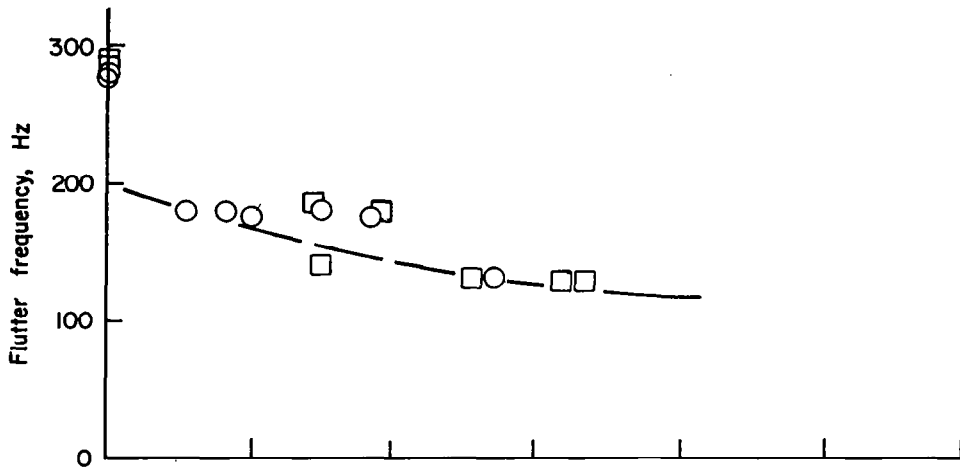
(k) Panel 11; $L/w = 2.88$.

Figure 9.- Continued.



(I) Panel 12; $L/w = 3.77$.

Figure 9.- Continued.



(m) Panel I3; $L/w = 2.88$.

Figure 9.- Concluded.

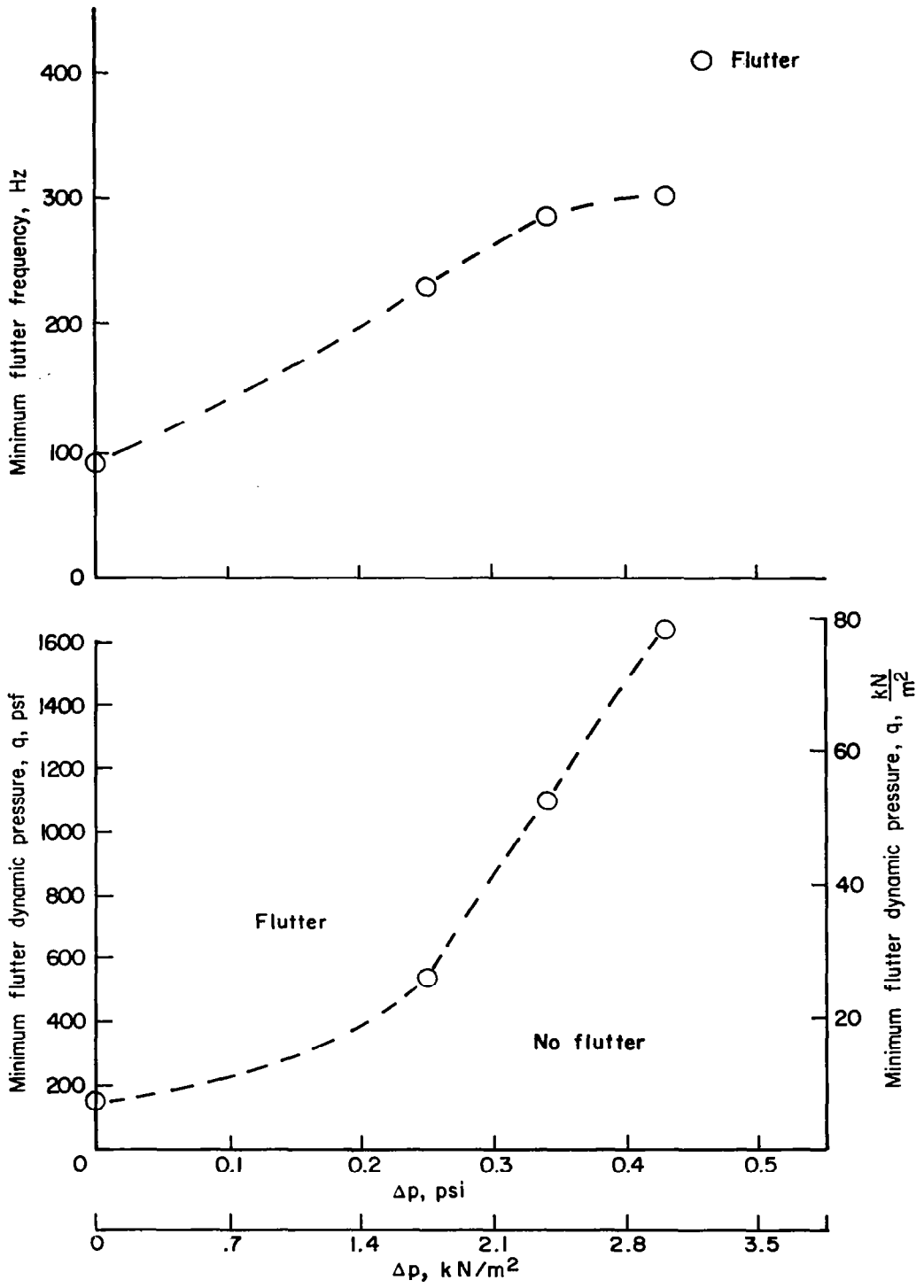


Figure 10.- Effect of pressure differential on the minimum flutter dynamic pressure and flutter frequency of panel 11. $M_1 = 1.96$.

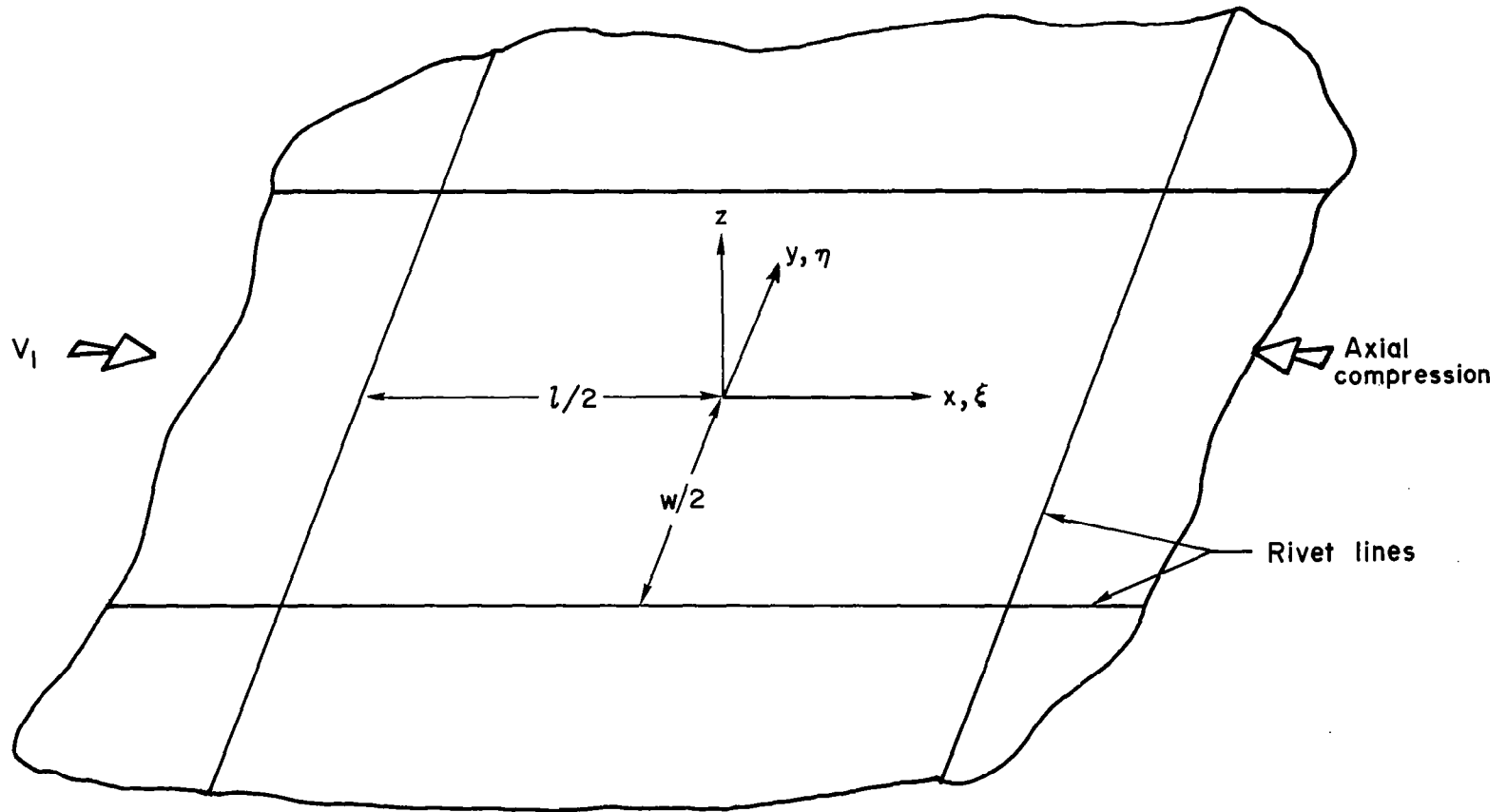


Figure 11.- Coordinate notation.

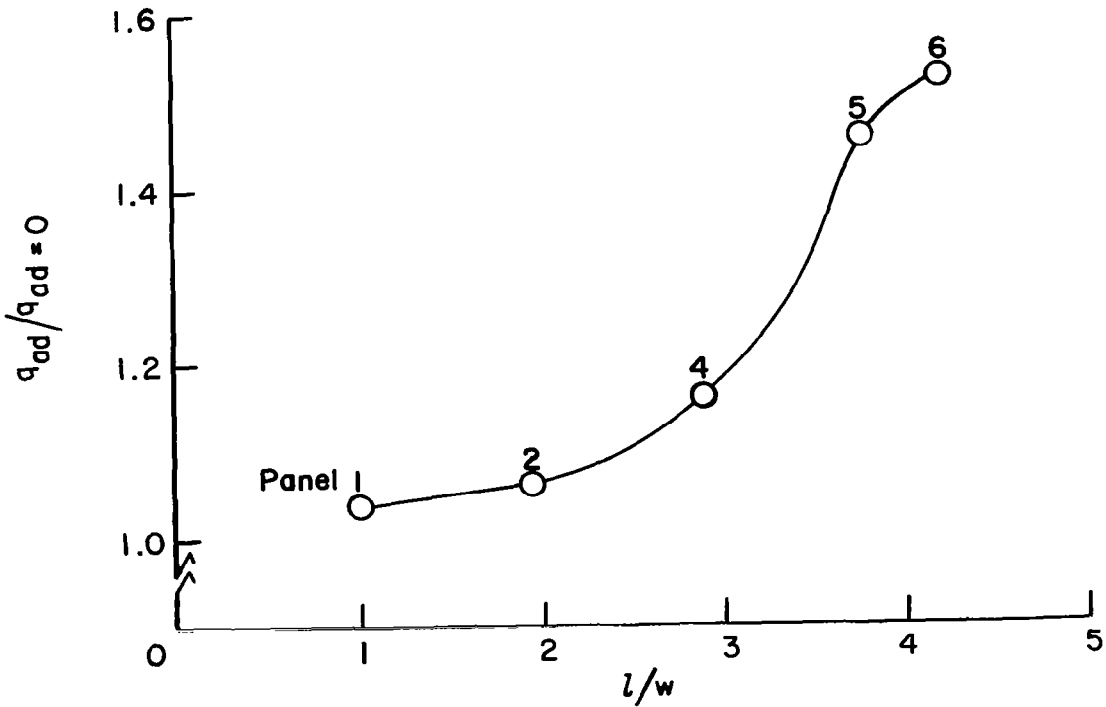
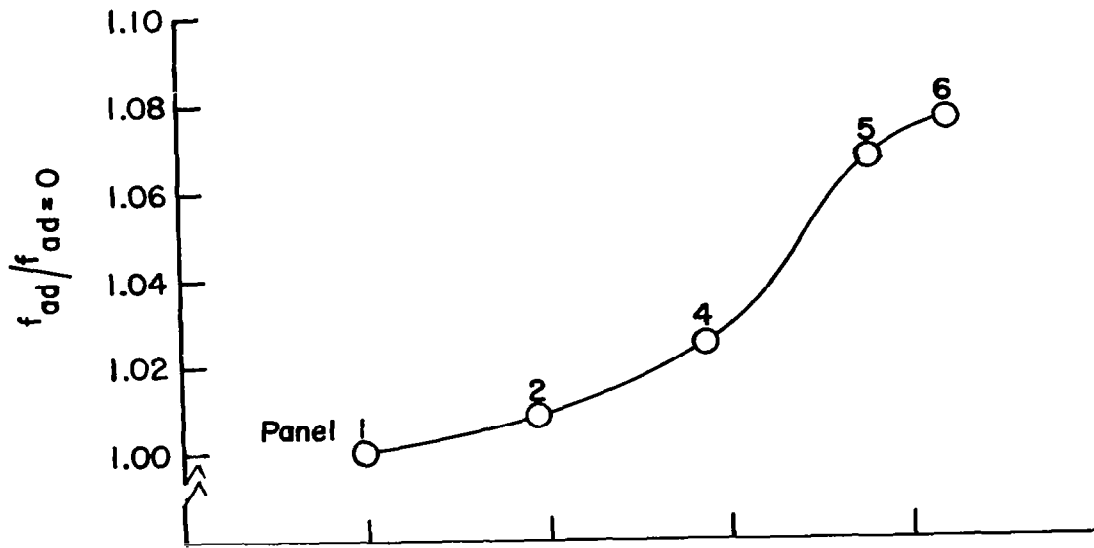


Figure 12.- Effect of aerodynamic damping on the flutter solution. $\alpha/\sigma_{cr} = 0$; $g = 0$ for panels 1, 2, 4, 5, and 6.

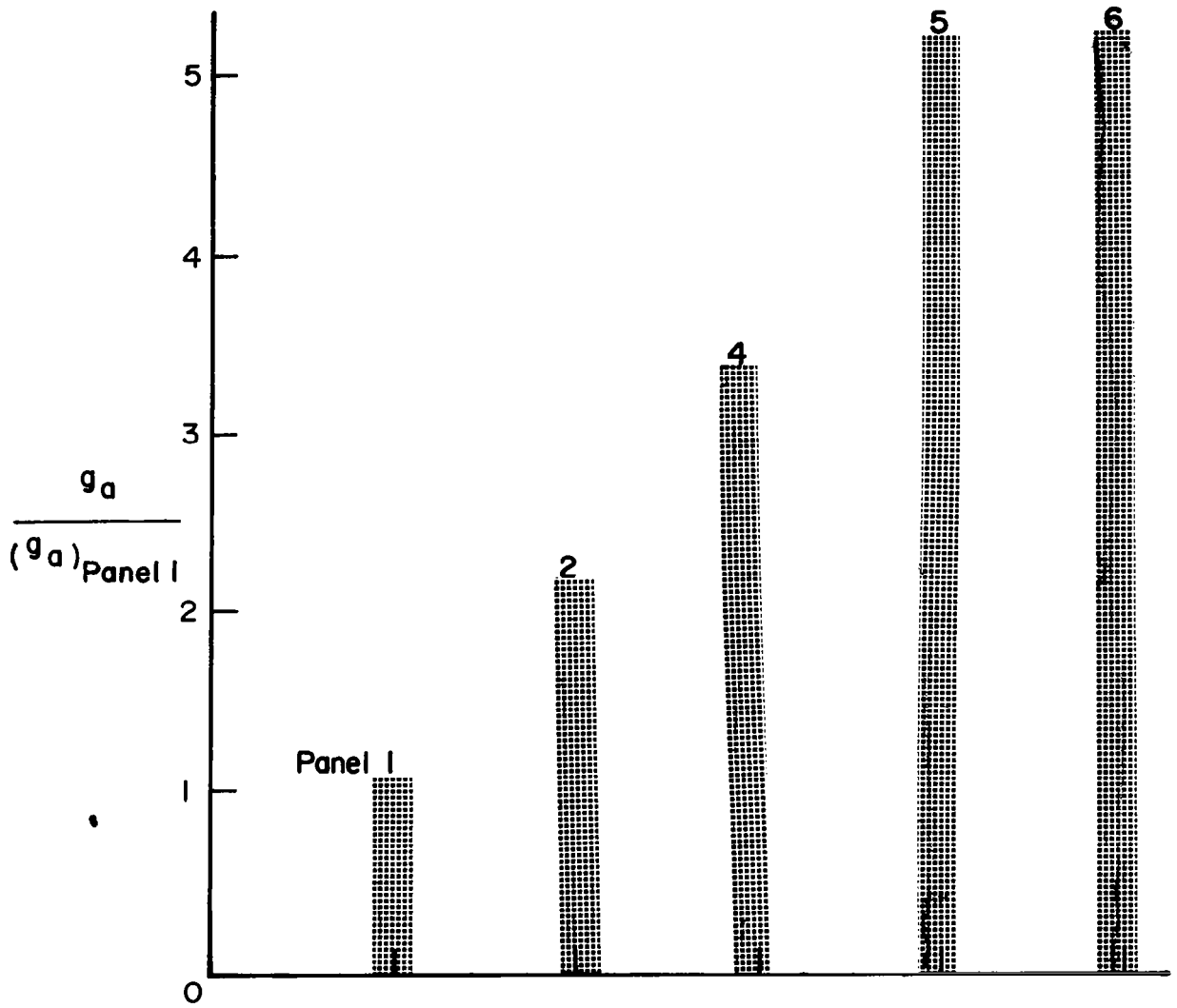
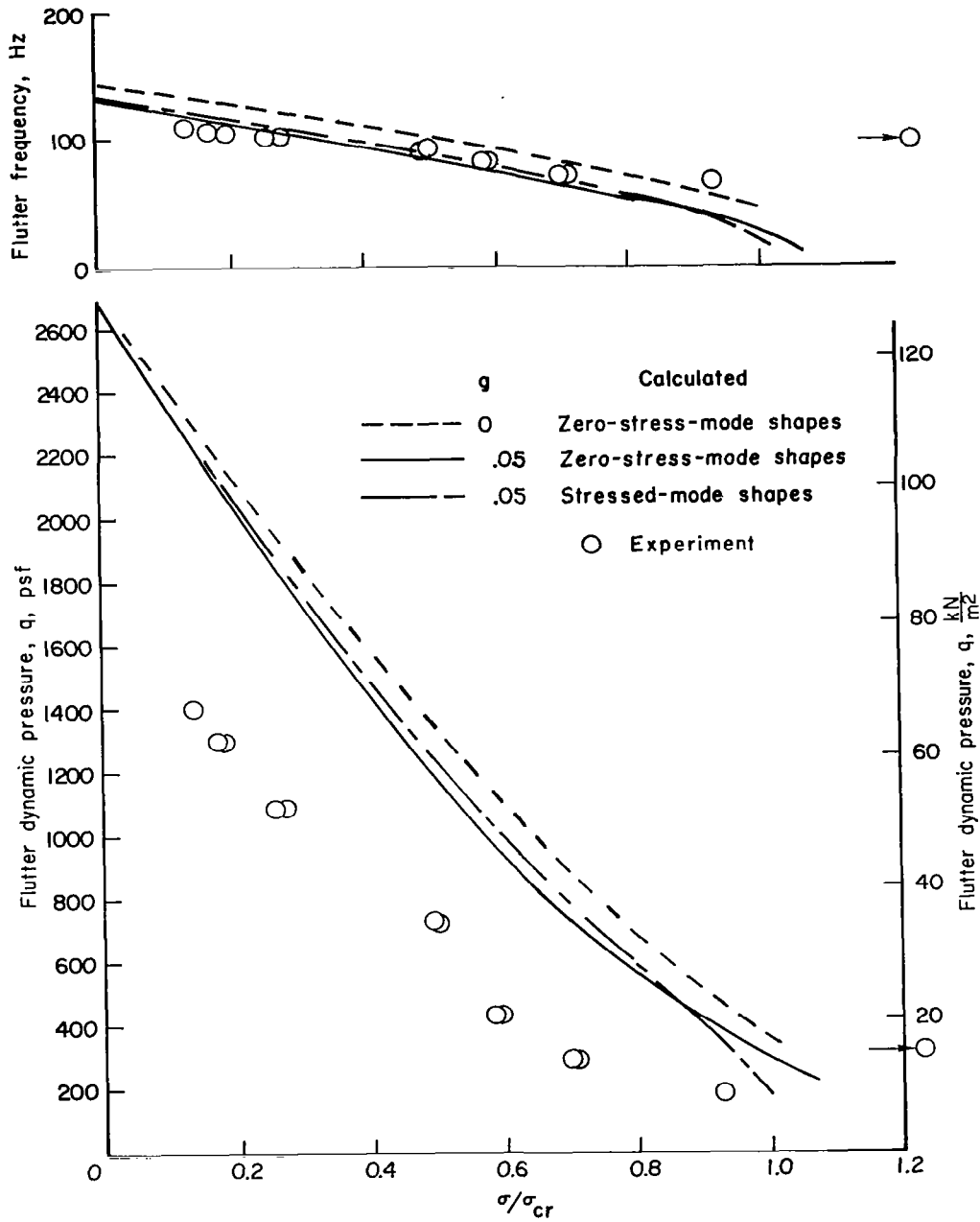
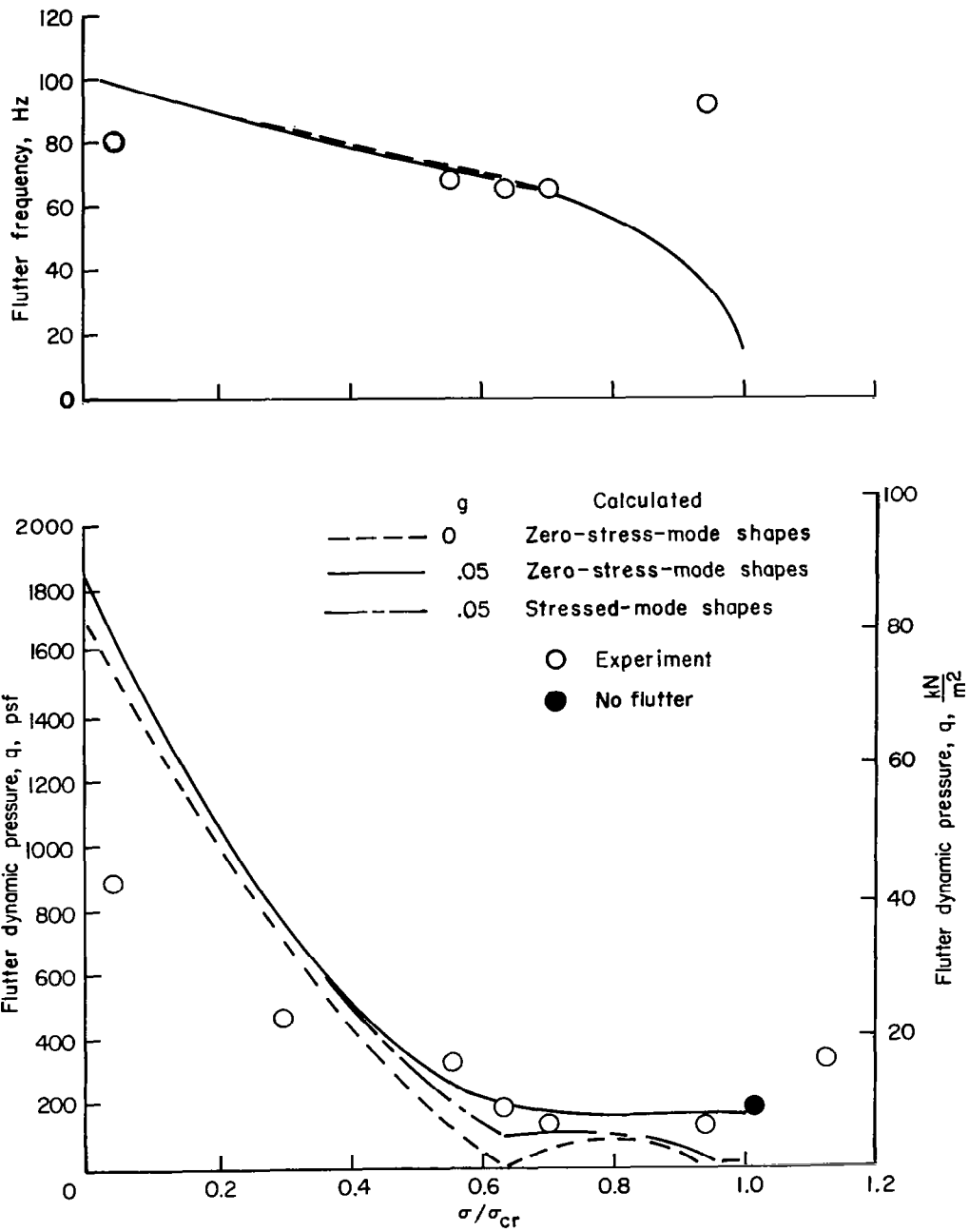


Figure 13.- Aerodynamic damping coefficient g_a for a semi-infinite panel at a constant dynamic pressure normalized by g_a for a panel having length and thickness of panel 1.



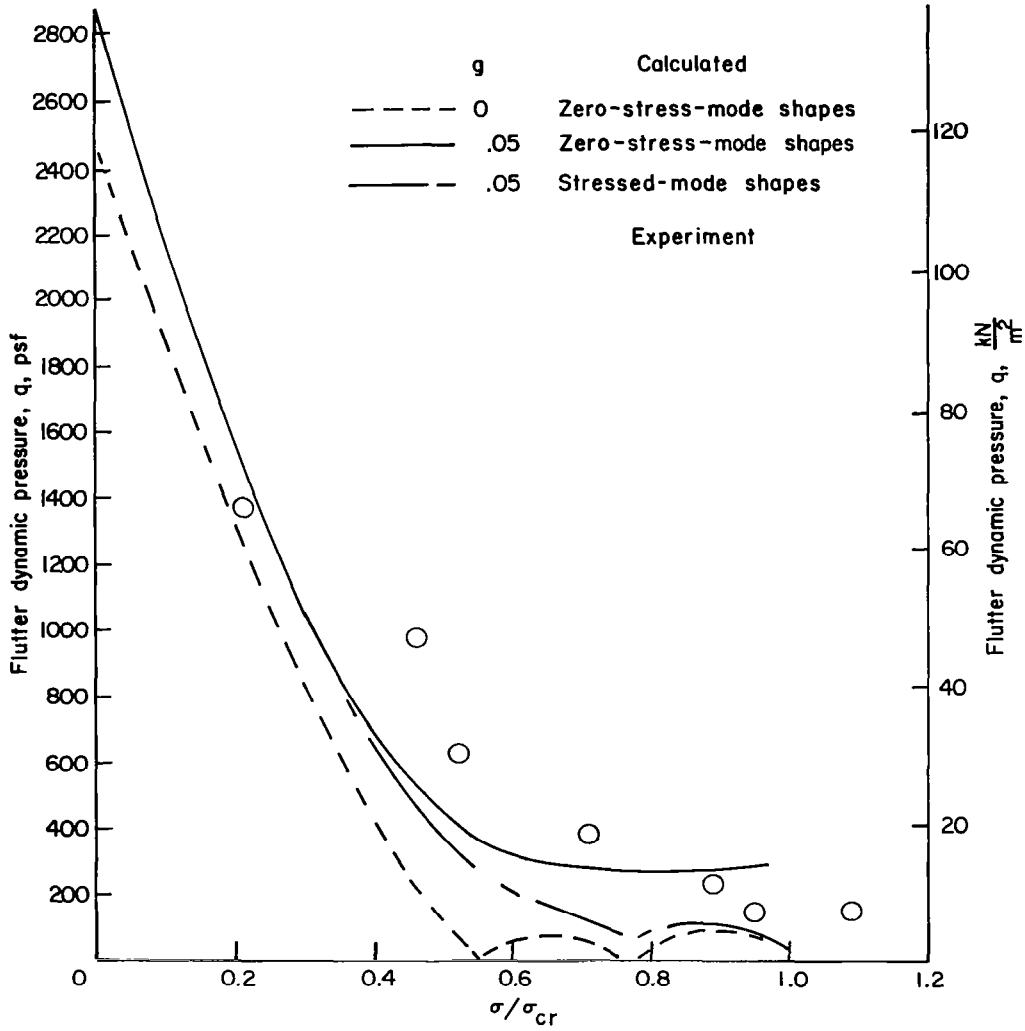
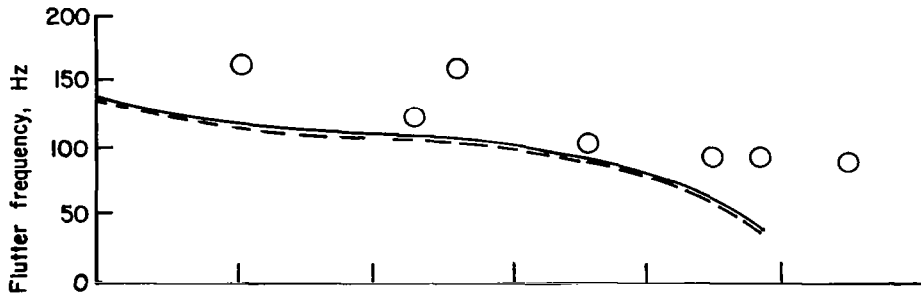
(a) Panel 1; $l/w = 1.0$.

Figure 14.- Comparison of experimental and theoretical results at $M_1 = 1.96$.



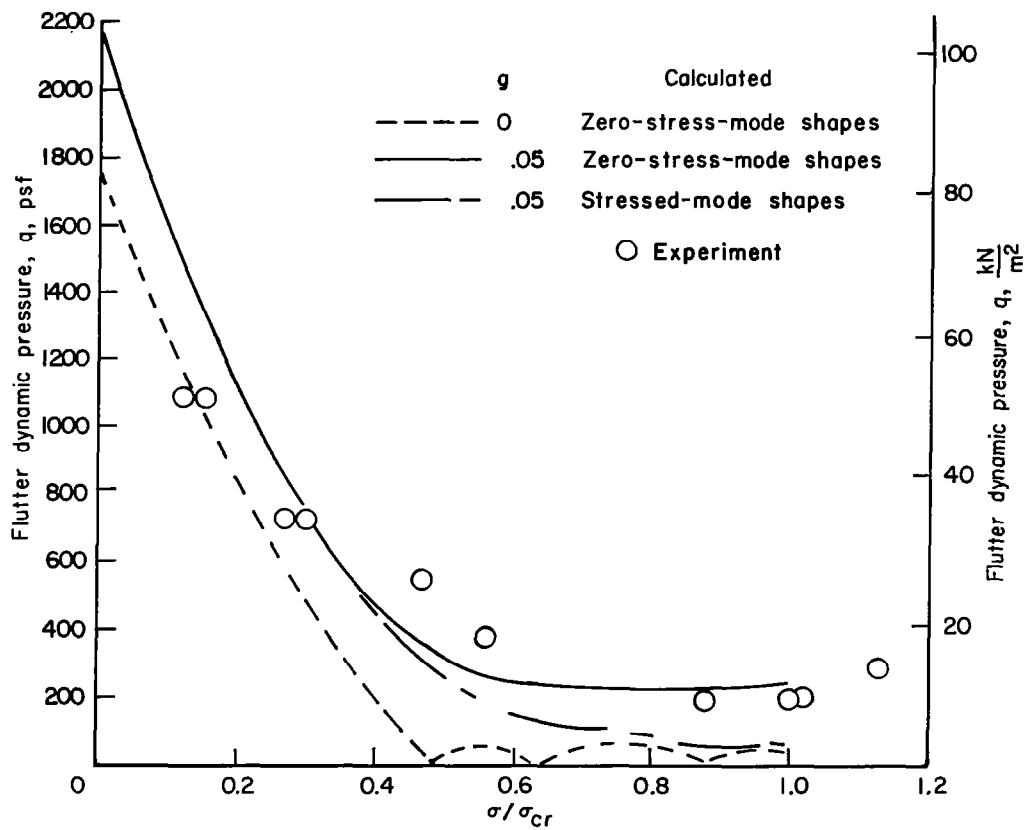
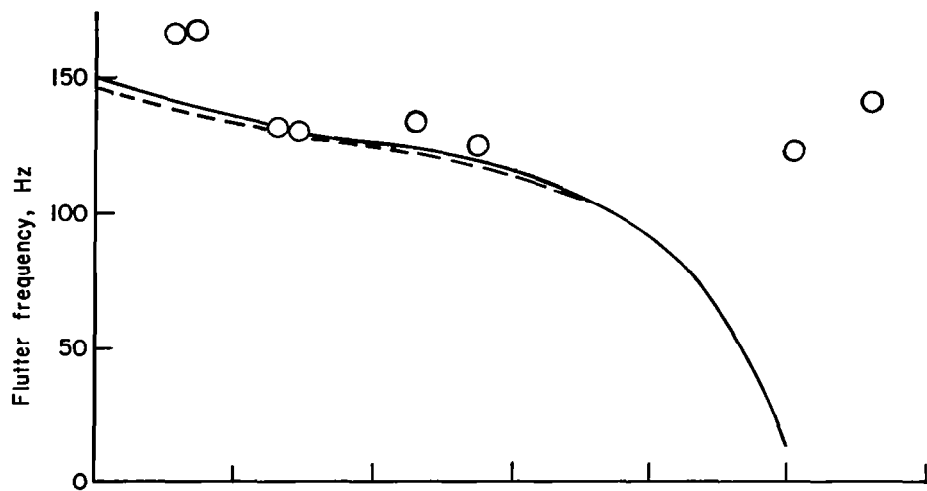
(b) Panel 2; $L/w = 1.96$.

Figure 14.- Continued.



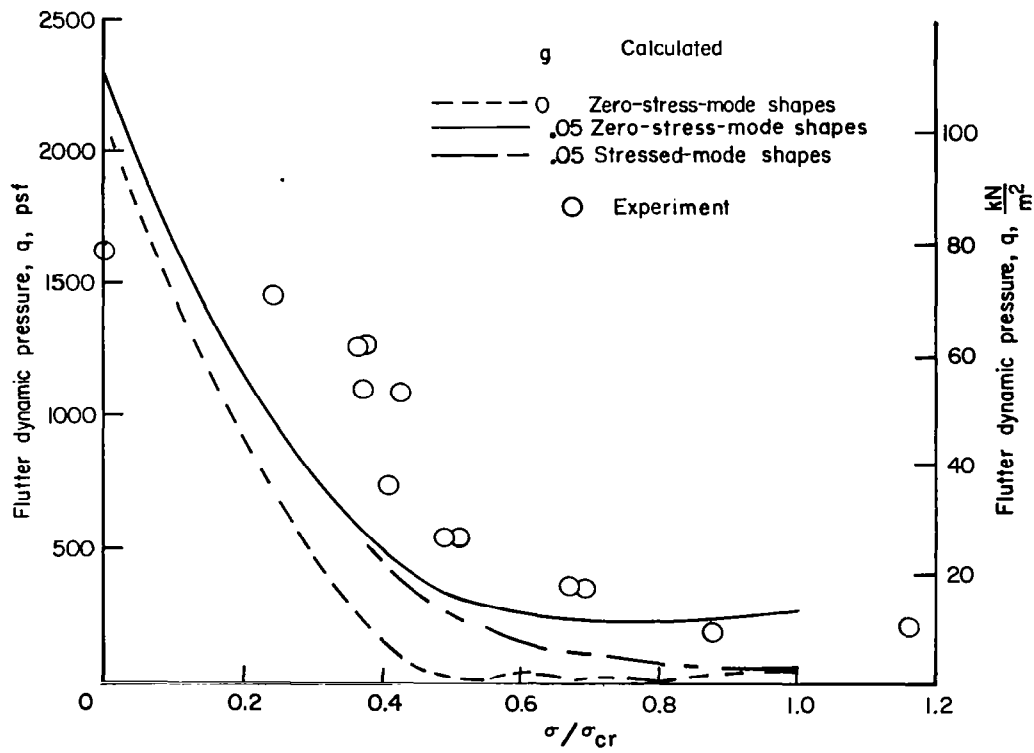
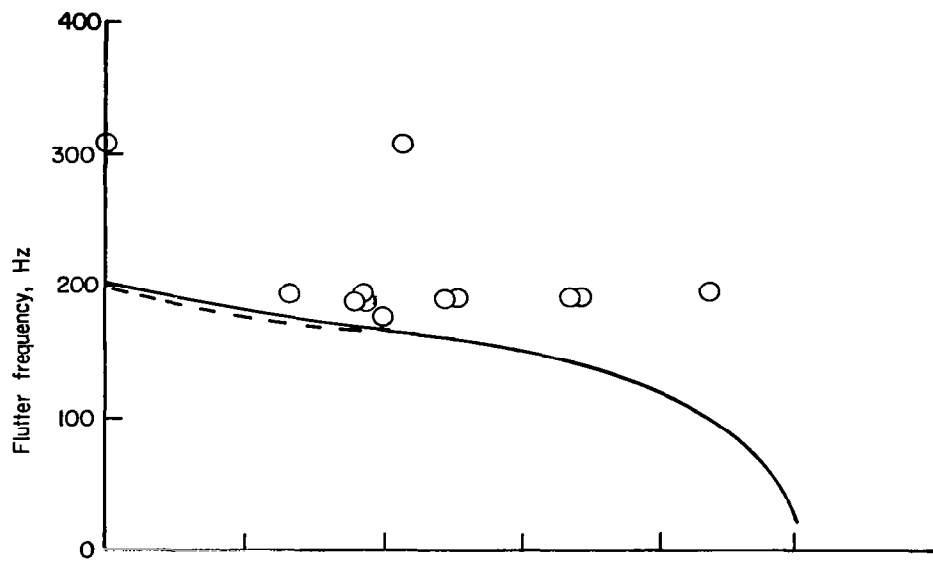
(c) Panel 3; $L/w = 2.43$.

Figure 14.- Continued.



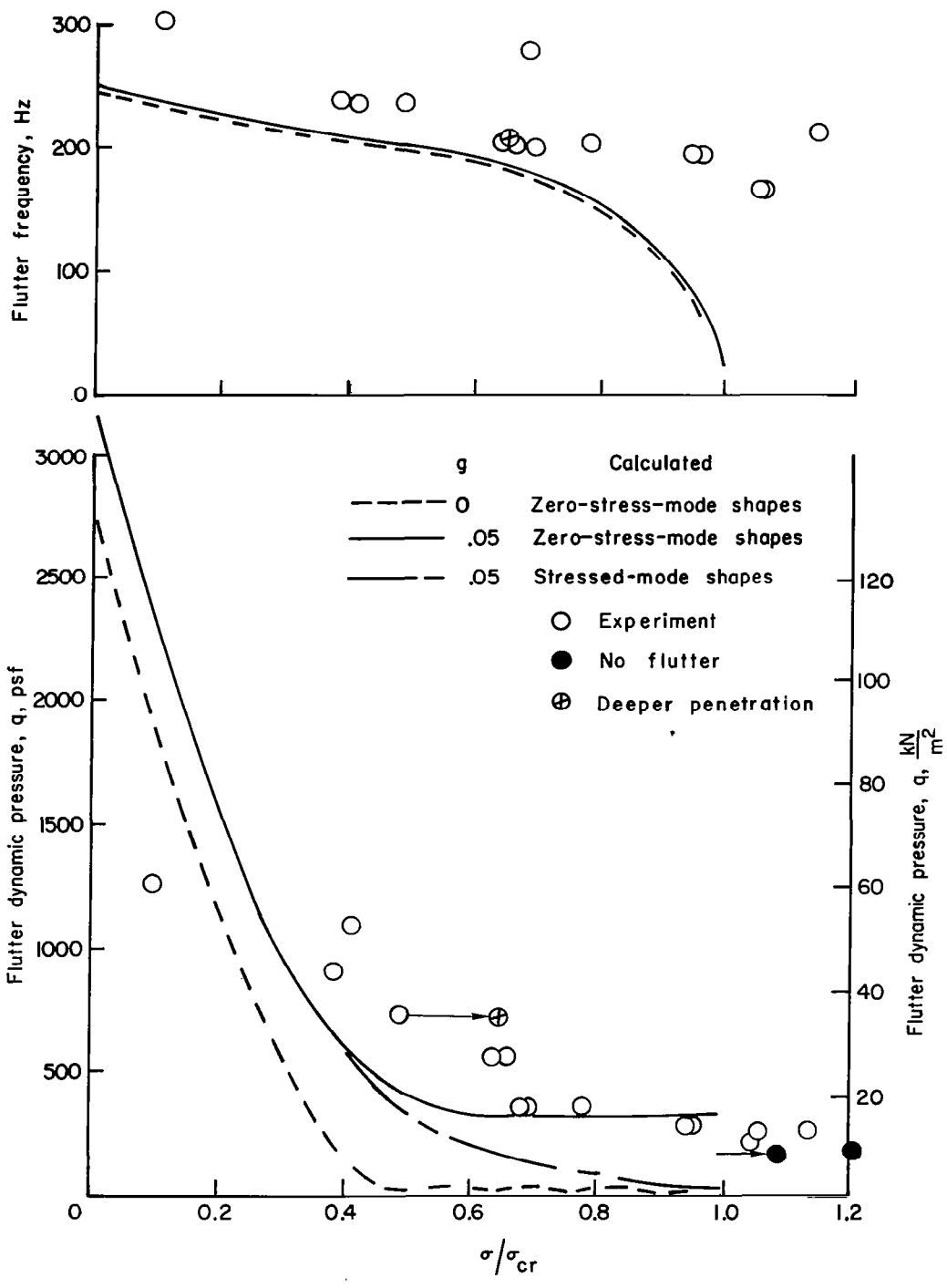
(d) Panel 4; $L/w = 2.88$.

Figure 14.- Continued.



(e) Panel 5; $l/w = 3.77$.

Figure 14.- Continued.



(f) Panel 6; $L/w = 4.202$.

Figure 14.- Concluded.

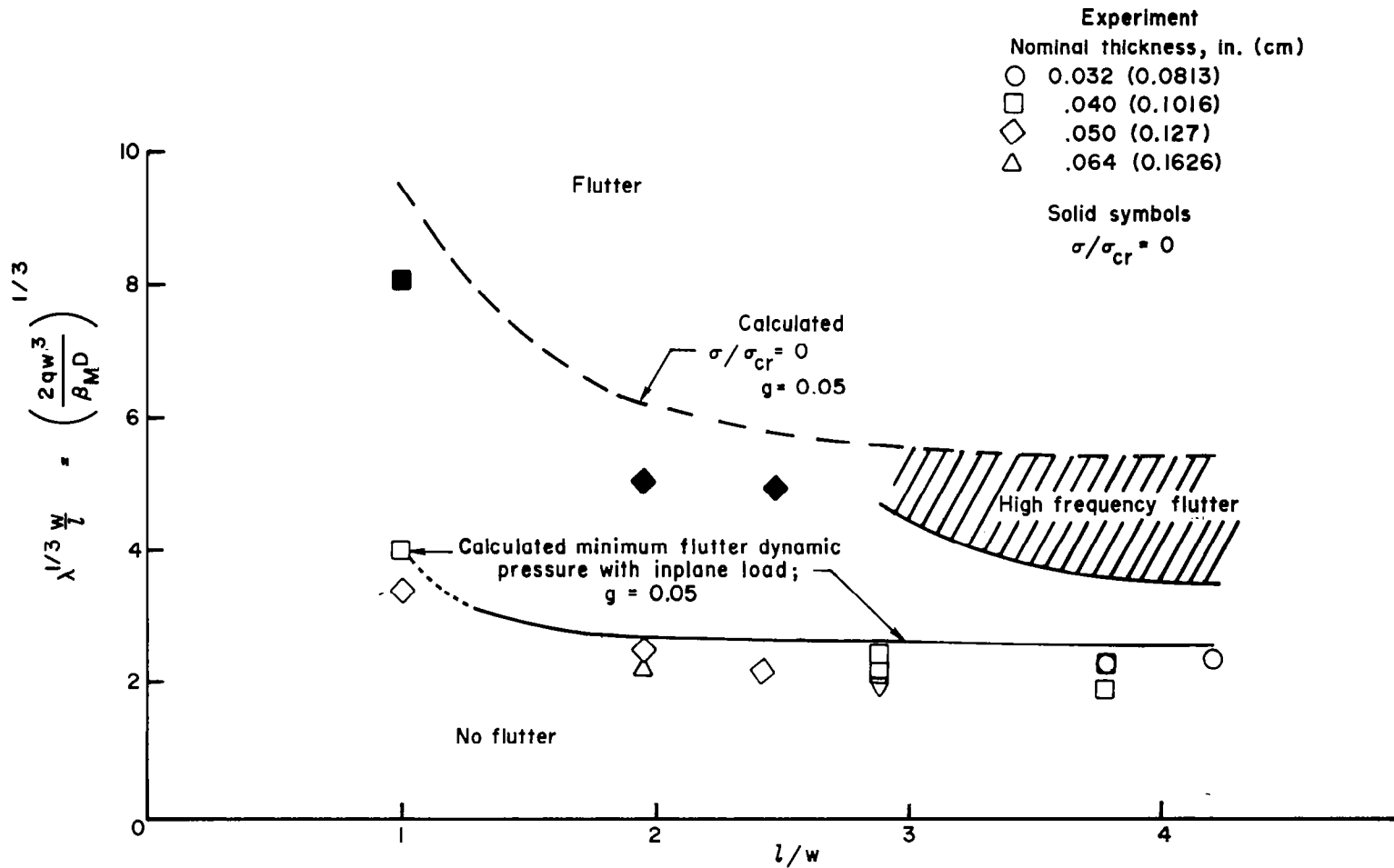
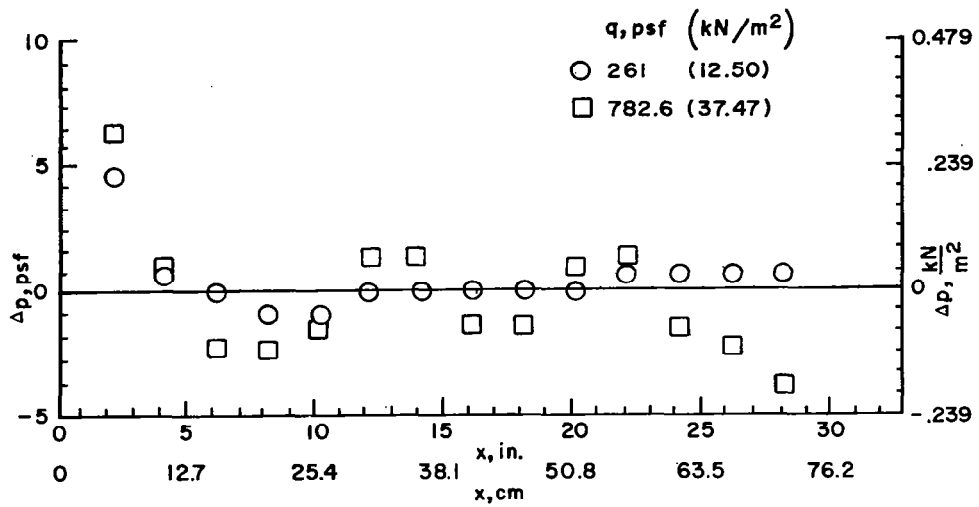
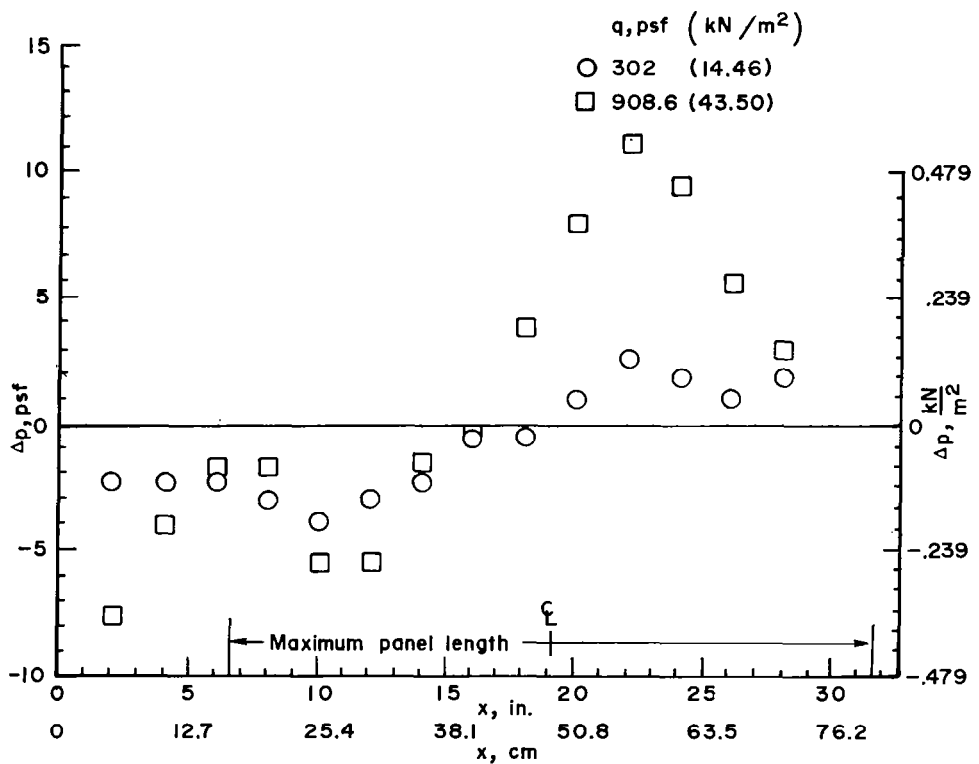


Figure 15.- Comparison of experimental and analytical results for modified flutter parameter $\lambda^{1/3} \frac{w}{l}$ as a function of length-width ratio. $M_1 = 1.96$.

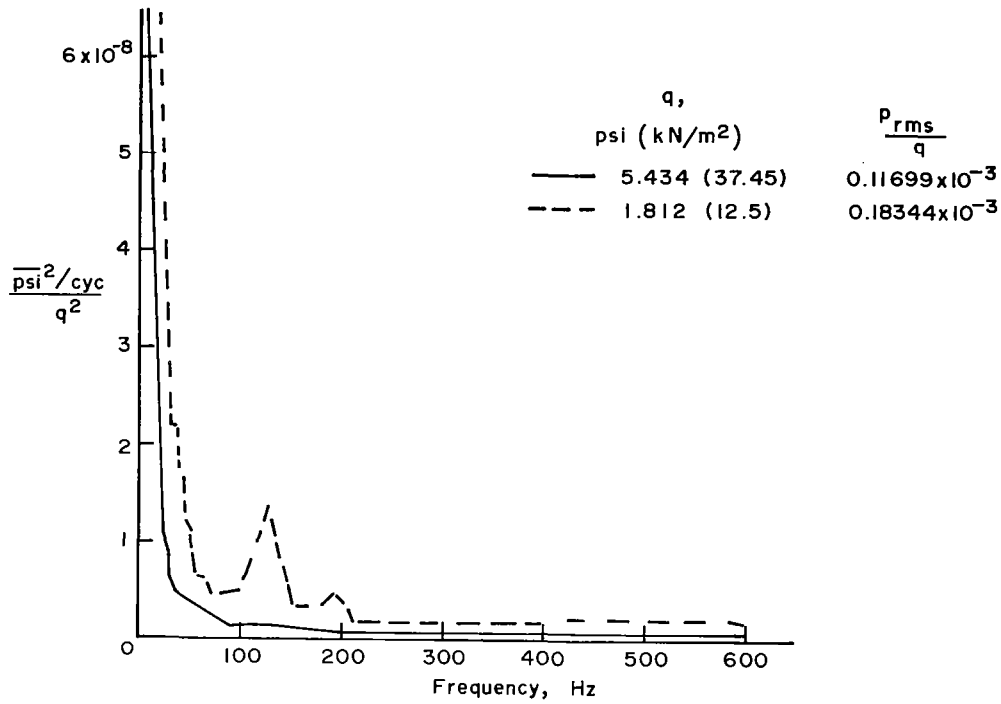


(a) $M_1 = 1.96$.

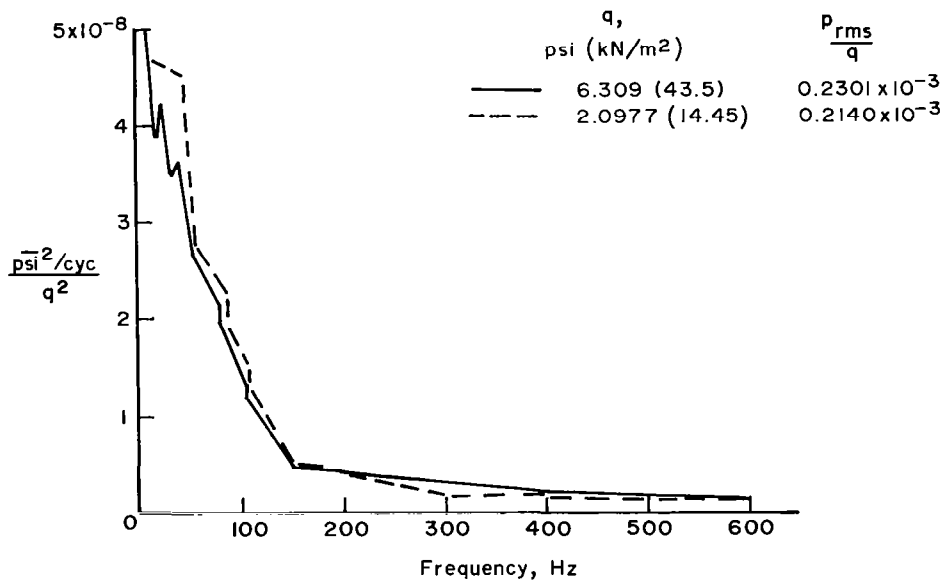


(b) $M_1 = 1.57$.

Figure 16.- Pressure differential along chord of splitter plate for zero pressure differential at Mach numbers of 1.96 and 1.57.



(a) $M_1 = 1.96$.



(b) $M_1 = 1.57$.

Figure 17.- Pressure spectra and overall fluctuating pressure normalized by dynamic pressure at $M_1 = 1.57$ and $M_1 = 1.96$.

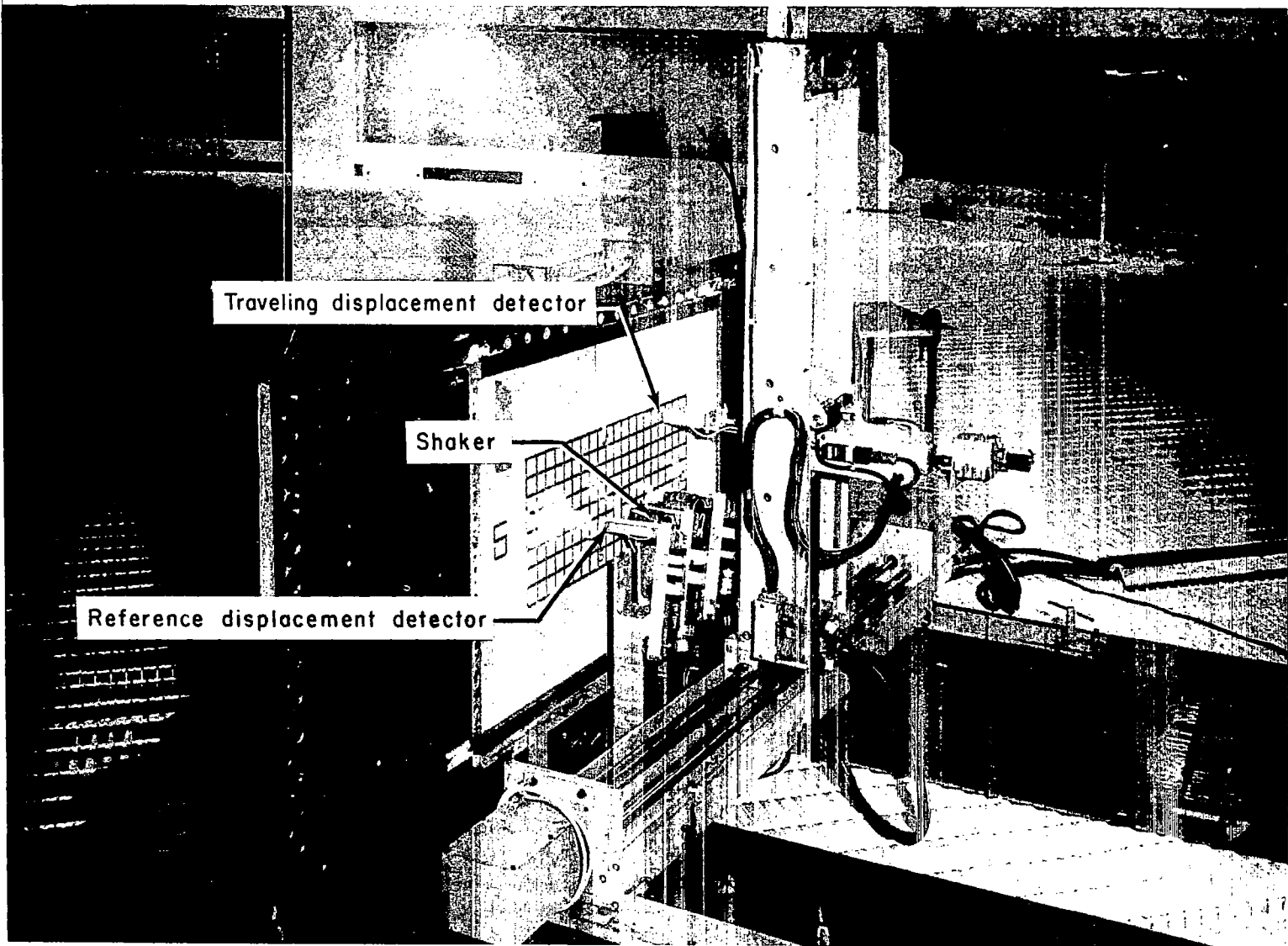


Figure 18.- Mode shape survey apparatus in Langley 55-foot vacuum chamber.

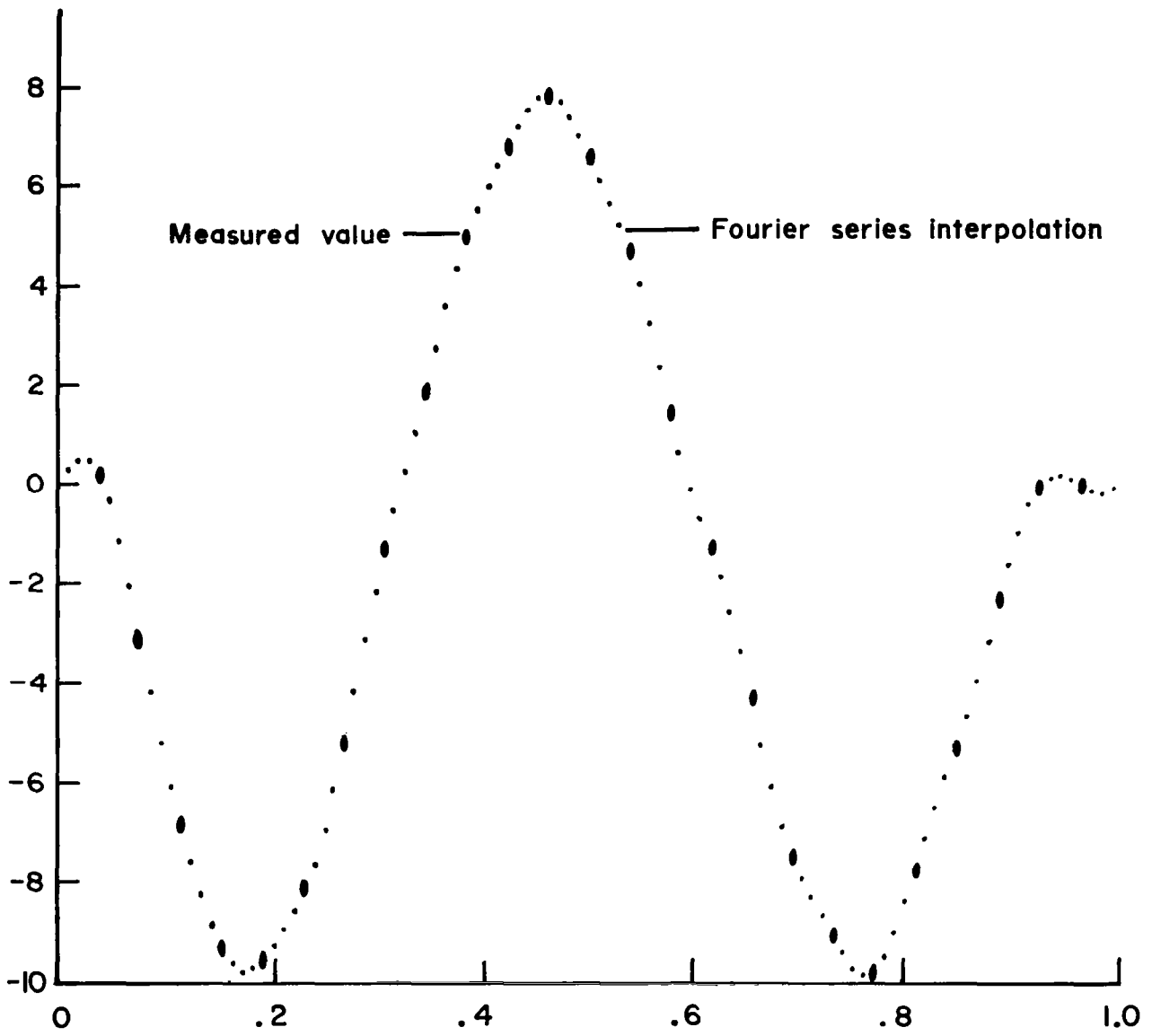


Figure 19.- Typical measured mode shape and program curve fit.